UNIVERSITÁ DEGLI STUDI DI TORINO

FACOLTÁ DI SCIENZE MATEMATICHE FISICHE E NATURALI

CORSO DI LAUREA SPECIALISTICA IN FISICA DELLE INTERAZIONI FONDAMENTALI

SEARCH FOR A $Z^{\pm}(4430) \to \psi(2S)\pi^{\pm}$ RESONANCE IN HADRON COLLISIONS AT CDFII

Laureando:
Francesco Rubbo

Relatore:
Stefano Argirò
Correlatori:
Diego Tonelli
Nadia Pastrone
Controrelatore:
Roberto Mussa

ANNO ACCADEMICO 2009/2010

CONTENTS

Introduction 4

1 Theory overview and experimental status 7
1.1 The Standard Model 7
1.2 The quark model 7
1.2.1 The eightfold way 8
1.2.2 The color quantum number 9
1.2.3 Symmetries and quantum numbers 10
1.3 Charmonium states and properties 10
1.4 Beyond the quark model 12
1.5 The XYZ mesons: experimental observations 12
1.5.1 X(3872) 12
1.5.2 Other XYZ mesons 14
1.6 The charged state $Z^-(4430)$ 14
1.6.1 Belle analysis 15
1.6.2 BaBar analysis 17
1.7 XYZ exotic states: theoretical models 18
1.8 Experimental aspects 19
1.8.1 The B-Factories 20
1.8.2 The hadron collider environment 20

2 The upgraded Collider Detector at the Fermilab Tevatron 23
2.1 The Fermilab Tevatron collider 23
2.1.1 Proton production 25
2.1.2 Antiproton production and accumulation 25
2.1.3 Injection and collisions 26
2.1.4 Tevatron performance 27
2.2 The CDF II detector 28
2.2.1 Coordinates and notation 28
2.2.2 Overview 30
2.3 The tracking system 30
2.3.1 The magnet 31
2.3.2 Layer 00 32
2.3.3 Silicon VerteX detector II 32
2.3.4 Intermediate Silicon Layers 33
2.3.5 Central Outer Tracker 33
2.3.6 Tracking performance 34
2.3.7 Muon detectors 36
2.4 Other detectors 37
2.4.1 Time of Flight detector 37
2.4.2 Calorimeters 37
2.4.3 Cerenkov Luminosity Counters 39
2.5 Trigger and Data Acquisition system 40
2.5.1 Level-1 41
2.5.2 Level-2 43
2.5.3 Level-3 43
2.6 Operations and data quality 43

2.7 Monte Carlo simulation of detector and trigger 45

3 Strategy, dataset and reconstruction 47
3.1 Strategy 47
3.1.1 The "displaced" approach 47
3.1.2 The "prompt" approach 47
3.2 Useful variables and physics objects 48
3.3 Trigger and samples 49
3.3.1 Monte Carlo samples 49
3.4 Off-line reconstruction 51
3.4.1 $\psi(2S)$ candidates 51
3.4.2 The $p\bar{p} \to Z^-[\to \psi(2S)\pi^-]$ + X channel 51
3.4.3 The $B^0 \to Z^-[\to \psi(2S)\pi^-]K^+$ channel 52

4 The "displaced" channel 53
4.1 Optimization of the $B^0 \to \psi(2S)K^+\pi^-$ signal 53
4.1.1 Study of discriminating observables 53
4.1.2 algorithm and results 56
4.2 The Dalitz plot 57
4.2.1 Acceptance 57
4.2.2 Comparison with Belle 59
4.2.3 The $\psi(2S)\pi^-$ mass distribution 59
4.2.4 Non-resonant $B^0 \to \psi(2S)K^+\pi^-$ decays 61
4.2.5 Combinatorial background 62
4.3 Summary of the "displaced" approach 64

5 The "prompt" channel 67
5.1 Motivation 67
5.2 Combinatorial background 67
5.3 Track quality studies 68
5.4 Muon quality studies 70
5.4.1 The $\psi(2S) \to \mu^+\mu^-$ sample 71
5.4.2 The $\psi(2S) \to J/\psi\pi^+\pi^-$ sample 73
5.5 Final configuration and first look at the $\psi(2S)\pi^-$ mass distribution 74
5.6 Peaking Background 77
5.7 The $Z^-(4430)$ region 78

6 Search optimization 81
6.1 Concept 81
6.1.1 A data-based unbiased optimization 82
6.2 Application 83
6.3 Significance 85
6.3.1 Significance scan 86
6.4 Optimization with independent signal 86
6.5 Summary of the "prompt" approach 87

7 Conclusions and prospects 89

A Data-simulation comparison 91

B Optimization procedure 93

INTRODUCTION

"Baryons can now be constructed from quarks by using the combinations (qqq), (qqqq$\bar{q}$), etc., while mesons are made out of (q$\bar{q}$), (qq$\bar{q}\bar{q}$), etc." . The original formulation of Constituent Quark Model (CQM) as proposed by Gell-Mann in 1964 [1], do not exclude more complex configuration for hadrons. However, until 2004 the simplest description with one valence quark and antiquark pair for mesons and three valence quarks for baryons, has provided good agreement with all experimental results, with the possible exception of some claims of observation of pentaquark, never established definitely.

In the latest years, experimental searches of particles in the mass range of the charmonium (a neutral bound state of a c-quark with $\bar{c}$-antiquark), have uncovered a number of resonances that do not fit immediately with CQM predictions. The first of these states has been the $X(3872)$, observed by the Belle experiment in 2004, and several others followed in the next years. The discovery of these states, collectively called XYZ mesons, has caused a revival of interest in charmonium spectroscopy, both in the theoretical and experimental communities. Many models have been proposed to describe the experimental results and provide predictions, some of them trying to reconcile the new observations with traditional descriptions, as variations of charmonium model, others suggesting more exotic interpretations, including multiquark states. The theoretical picture is still far from clear. Intense experimental activity is ongoing to provide additional constraining information and shed light in this aspect of low-energy Quantum ChromoDynamics (QCD) phenomenology.

A major breakthrough in this scenario has been the observation of an exotic charged state: the $Z^-(4430)$. The Belle experiment reported the observation of this particle in 2008, as a 4430 MeV c^{-2} resonance in the $\psi(2S)\pi^-$ mass distribution of B decays to $\psi(2S)K\pi^-$ final states [2][1]. Being charged, this particle cannot fit with any quarkonium description and is the first solid candidate for a multiquark state, with minimal quark content $cu\bar{c}\bar{d}$. If confirmed, the $Z^-(4430)$ would impose crucial constraints to the models aiming at a general description of the XYZ states. A search for this resonance was performed by the BaBar experiment in an experimental environment similar to Belle's one but with a smaller event sample. This search has not been able to confirm Belle's result. In this somewhat contradictory experimental scenario input from other experiments could be extremely valuable in determining definitively, or excluding, the existence of such a multiquark state. This thesis describes the first search for $Z^-(4430)$ resonance in hadron collisions, an environment strongly different from e^+e^- collisions at the $\Upsilon(4S)$ resonance exploited by the Belle and BaBar experiments, which offers new challenges but also additional opportunities in the experimental study of these states.

This thesis was conducted from August 2009 to July 2010 at the Fermi National Accelerator Laboratory, 50 km west of Chicago. It describes a search for $Z^-(4430)$ resonances in 5.7 fb^{-1} of data collected by the upgraded Collider Detector at Fermilab (CDFII) experiment at the Tevatron p$\bar{\text{p}}$ collider. The Tevatron collider is a superconducting protosynchrotron that collides protons against antiprotons, circulating on a 1 km radius ring, at center of mass energy of 1.96 TeV. CDFII is a multipurpose particle detector composed by a magnetic spectrometer, hermetic 4π calorimeters and muon detectors. At the Tevatron XYZ states can be produced directly in the hard-scattering or as intermediate resonances in heavy flavor decays (similarly to B-Factories). In this analysis we devised a complete and coherent approach that explored both possibilities exploiting the highly efficient trigger on low-p_{T}, opposite-charge muon pairs available at CDF, and the excellent tracking and vertexing

1 In Belle's and BaBar's analyses, both charged and neutral B decays are included, so, here and in the following of this thesis, K stands for both K^+ or K^0_S, unless otherwise explicitly indicated.

performance of the CDFII detector. We performed two parallel analyses, one exploring the $\psi(2S)\pi^-$ mass spectrum in $B^0 \to \psi(2S)K^+\pi^-$ decays, and the other searching for a $\psi(2S)\pi^-$ resonance without any other requirement on the event. In the first case we optimized the B signal and studied the Dalitz plot of the decay in comparison with Belle's result. The second approach has proved more promising. The accurate and detailed study of the optimal configuration of reconstruction requirements in terms of track and muon quality has represented an important part of the work. The systematic study of several different quality requirements for muons and the difficult choices made, aiming at the best compromise between signal purity and sufficient event statistics, have been the key contributions for the achievement of the analysis. An innovative method of optimization [3] has been used to extract the final result.

The work described in this thesis is the first search for a $Z^-(4430)$ resonance in hadron collisions and has been conceived, carried out and concluded entirely by the author. An ad-hoc analysis framework has been developed based on reconstruction code already consolidated in other analysis, adapted and modified for the purpose of this work. The progress of the work has been periodically presented in internal meetings of the CDF B-physics group and documented in internal notes. The thesis is organized as follows:

CHAPTER 1 provides a brief summary of the standard theoretical model for charmonium states, followed by a description of the experimental status of the XYZ mesons and the theoretical models proposed to understand their phenomenology.

CHAPTER 2 describes the accelerator and the CDFII detector. The sub-detectors used to reconstruct charged-particles trajectories and muons are described in greater detail, because more closely related to the present analysis.

Starting from Chapter 3, the original contribution of the author is presented and discussed.

CHAPTER 3 introduces the analysis strategy and details the data sample, the reconstruction algorithms and the Monte Carlo simulations used.

CHAPTER 4 contains the description of the search for a $Z^-(4430)$ as intermediate $\psi(2S)\pi^-$ state in $B^0 \to \psi(2S)K^+\pi^-$ decays ("displaced" analysis). The optimization of the B^0 signal, the study of the Dalitz plot and the comparison with Belle's result are discussed.

CHAPTER 5 describes studies aimed at optimizing the search for $Z^-(4430)$ decays without requiring the presence of a B decay ("prompt" analysis). These include studies of track and muon quality to limit the adverse effect of the combinatorial background, and comparison between different possible final states for the $\psi(2S)$.

CHAPTER 6 explains the data-based optimization used to extract the signal. The estimation of the significance of the results follows, together with studies of the physics background and test of the robustness of the signal.

CHAPTER 7 summarizes the results of this work and discuss some future prospects.

In this document particle symbols are taken from the Particle Data Group (PDG) notation and inclusion of the charge conjugate modes is always implied.

1 THEORY OVERVIEW AND EXPERIMENTAL STATUS

This chapter provides a brief summary of the theoretical background relevant for this thesis and an introduction to the experimental status of the XYZ meson spectroscopy.

1.1 THE STANDARD MODEL

The Standard Model of particle physics is a quantum field theory describing the fundamental interactions between elementary particles: electromagnetic, weak and strong interaction. Gravity is not included in the model; gravitational forces are insignificant at the energies currently accessible in particle physics experiments. So far the greatest majority of experimental results seem to agree with the Standard Model predictions, but a broad and intense experimental effort is devoted to identify the first signs of beyond-the-standard-model physics, which is believed to become experimentally accessible at the TeV scale.

Elementary particles are classified into particles of matter, force-mediating particles and the Higgs boson.

Particles of matter are fermions (spin $\frac{1}{2}$) and are divided into leptons (electron, muon, tau and their neutrinos) and quarks (up, down, charm, strange, top and bottom). Each particle has its corresponding antiparticle, which has the same mass but opposite quantum numbers. Leptons and quarks are grouped in three generations or flavors, shown in table 1.

Force-mediating particles are bosons (spin 1). They are exchanged between particles of matter when they interact through one of the three fundamental interactions.

- The electromagnetic interaction, which involves electrically charged particles, is mediated by the photon, a massless and electrically neutral boson.

- The weak force has three mediators: the Z^0 and the $W^{\pm}$. The Z^0 is electrically neutral and has a mass of (91.1876 ± 0.0021) GeV c^{-2} [4]; the $W^{\pm}$ are electrically charged and have masses (80.403 ± 0.029) GeV c^{-2} [4]. Both leptons and quarks are sensitive to the weak interaction.

- The strong force describes the interaction between particles provided of color-charge (quarks) via eight gluons. They are massless and electrically neutral; however they carry a color-anticolor charge. Leptons don't couple to the strong force.

The Standard Model also predicts the existence of the yet unobserved Higgs boson, a hypothetical massive scalar particle. The Higgs field is the cause of the difference in mass between photon and $W^{\pm}$ and Z^0 through spontaneous breaking of the electroweak gauge symmetry. It can also couple with fermions providing mass to leptons and quarks.

1.2 THE QUARK MODEL

Since in this thesis we studied the properties of multiquark states, in the following a more detailed introduction to the phenomenology of hadrons is presented.

Type	Charge	Spin	Particles		
Leptons	-1	1/2	e^-	μ^-	τ^-
	0	1/2	ν_e	ν_μ	ν_τ
Quarks	+2/3	1/2	u	c	t
	-1/3	1/2	d	s	b
Mediators	0	1		γ	
	-1,0,+1	1	W^-	Z^0	W^+
	0	1		*Gluons*	
Higgs Boson	0	0		H	

Table 1: Elementary particles

1.2.1 The eightfold way

Quarks are confined within composite particles called hadrons, bound by the strong interaction. While a detailed and quantitative understanding of strong dynamics at the low energies (MeV) involved in quark-quark interactions within hadrons has not been achieved so far, in the '60 Gell-Man, Zweig and Nishijima [1] proposed a classification scheme for hadrons, based on their valence quarks and the underlying symmetries, which has proven successful: the Constituent Quark Model (CQM). Table 2 shows the properties of the known quarks.

Quark	Charge (e)	Mass	Isospin I_z	B
Up u	+2/3	1.5-3.3 MeV c^{-2}	1/2	1/3
Down d	-1/3	3.5-6.0 MeV c^{-2}	-1/2	1/3
Charm c	+2/3	$1.27^{+0.07}_{-0.11}$ GeV c^{-2}	0	1/3
Strange s	-1/3	70-130 MeV c^{-2}	0	1/3
Top t	+2/3	171.2 ± 2.1 GeV c^{-2}	0	1/3
Bottom b	-1/3	$4.2^{+0.17}_{-0.07}$ GeV c^{-2}	0	1/3

Table 2: Properties of quarks: electric charge, mass, isospin and baryon number

According to this classification hadrons are grouped in mass multiplets defined by an approximate symmetry. In the original scheme by Gell-Mann and Nishijima, the three light flavors (u, d, s) were taken into account, because they were the only ones hypothesized at the time. Hadrons were described as formed by different combination of quarks in these three states. Mathematically this corresponds to the $SU(3)$ symmetry. The simplest representations of this symmetry, corresponding to particles with integer charge, are multiplets of one, eight, or ten members.

Both mesons, bosons composed of a quark-antiquark pair, and baryons, fermions composed of three quarks, have to belong to these families. Observed light mesons actually can be represented as scalar and vector octets and singlets according to their spin while light baryons are grouped in a spin $\frac{1}{2}$ octet and a spin $\frac{3}{2}$ decuplet. Fig. 1 shows the representation of the multiplets in diagrams where the isospin is on the horizontal axis and the hypercharge, defined as the sum of baryon number and strangeness, lies on the vertical axis. The quantum numbers of each state satisfy the relation

$$Q = I_3 + \frac{Y}{2}$$

where Q is the electric charge in units of e, I_3 is the third component of isospin and Y is the hypercharge.

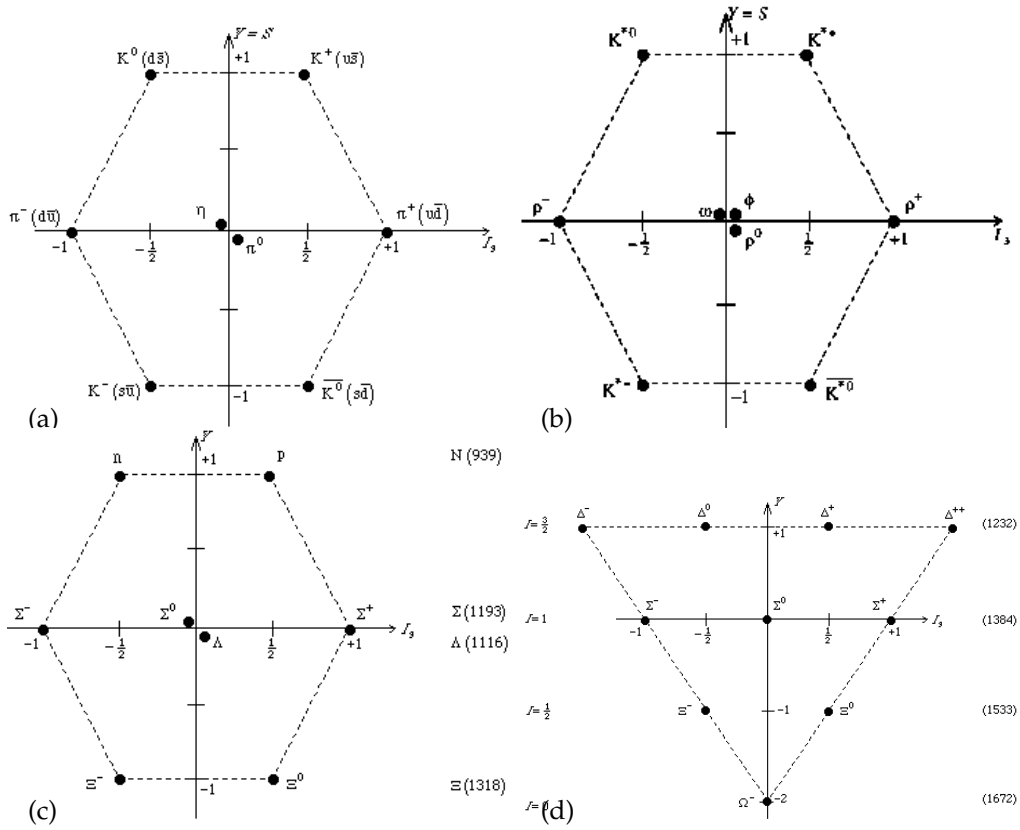

Figure 1: Representations of the pseudoscalar meson octet (a), the vector meson octet (b), the baryon octet (c) and the baryon decuplet (d).

This description allows approximate predictions of the mass difference between isospin multiplets through the Gell-Mann–Okubo mass formulae. The SU(3) symmetry described here referred to the light flavor of quarks (u, d, s). The other flavors (c,b,t) were discovered subsequently. They are much heavier and they do not easily fit in an expansion of the symmetry SU(n), with n greater than 3. The approximate flavor SU(3) symmetry remains useful to describe the properties of the light hadrons and classify them.

The introduction of Quantum ChromoDynamics (QCD) showed that a separate SU(3) symmetry, associated with a quantum degree of freedom called *color*, is the basis of the strong interaction that bound quarks in hadrons.

1.2.2 The color quantum number

The current description of hadrons prescribes that quarks and gluons have an additional quantum number, called *color charge*, which characterizes three states: red, green and blue (r, g, b). The color charge is responsible for the strong interaction. A quark can take one of the three colors, while an antiquark takes an anticolor. Gluons carry both a color and an anticolor. The color confinement principle requires hadrons to be colorless. There are infinite configurations to satisfy this condition, but, so far, the two simplest type of hadrons have been considered: mesons and baryons.

1.2.3 Symmetries and quantum numbers

Also discrete symmetries play an important role in the quark model. This paragraph briefly describes the main features of the corresponding operators.

- Charge symmetry (C): replaces every particle by its antiparticle.
- Parity symmetry (P): reflects the three spatial coordinates.
- Time symmetry (T): reverses the direction of time.

Particles are characterized by their quantum numbers, which describe values of conserved quantities. The isospin I_z is a quantum number related to the strong interaction and depending on the up and down quark content of the hadron, so that $I_z = \frac{1}{2}(N_u - N_d)$, where N_u and N_d are the numbers of up and down quark respectively. The total angular momentum J of a hadron is the combination of the orbital angular momentum L between the quarks and the total spin S, which is the combination of the spins of the quarks. S is equal to 0 or 1 for mesons, and to $\frac{1}{2}$ or $\frac{3}{2}$ for baryons. Since the charge and parity symmetries are unitary operators, their eigenvalues can only take the values ± 1. For mesonic states, the parity eigenvalue is related to the orbital angular momentum through $P = (-1)^{L+1}$. In addition, for quarkonia, which are eigenstates of the charge conjugation, one has $C = (-1)^{L+S}$.

Table 3 resumes the quantum numbers relevant for the quark model classification scheme.

q	electric charge	
B	baryon number	$\frac{1}{3}$ for quarks, 0 for leptons
S	spin	
I_z	isospin	$I_z = \frac{1}{2}(N_u - N_d)$
L	orbital angular momentum	
J	total angular momentum	$\lvert L - S \rvert \leq J \leq L + S$
P	parity	$P = (-1)^{L+1}$ for mesons
C	charge conjugation	$C = (-1)^{L+S}$ for quarkonia

Table 3: Quantum numbers and some relation between them.

1.3 CHARMONIUM STATES AND PROPERTIES

A flavorless meson composed of a heavy quark and its own antiquark is called a quarkonium. It is called a charmonium if it is a $c\bar{c}$ meson like the J/ψ. Charmonium states have masses around $3\,\mathrm{GeV}\,c^{-2}$.

The discovery of $c\bar{c}$ states in the 70s, prompted the introduction of QCD-motivated quark potential models in order to understand the charmonium spectroscopy. The inspection of the energy levels of charmonium (Fig. 2) showed similarities with positronium and suggested that charmonium level can analogously be described through a static nonrelativistic potential.

In analogy with the description of positronium, charmonium states are described as a $c\bar{c}$ pair bound by an interquark force with a short-distance behavior dominated by single-gluon exchange ($\propto \frac{1}{r}$). At large distance, however, the potential must increase with r, to meet the experimental evidence that no free quarks are observable and are confined inside the hadrons. Thus, an effective potential can be written as

$$V = -\frac{4}{3}\frac{\alpha_S}{r} + kr$$

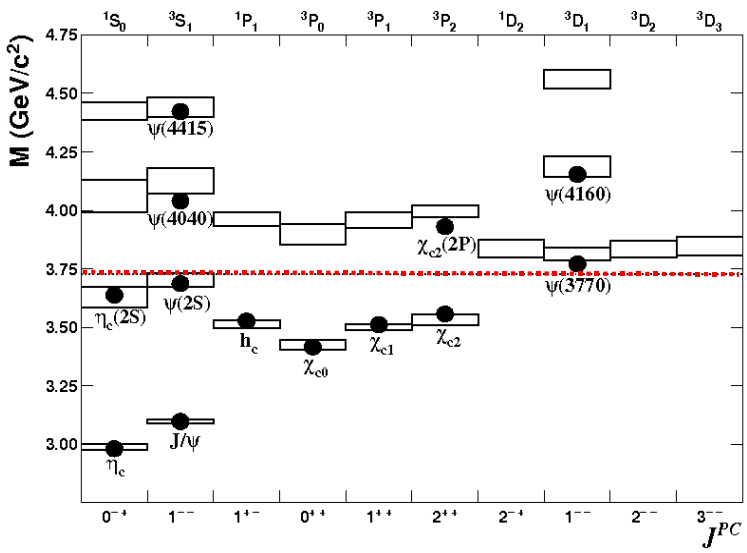

Figure 2: Diagram of charmonium levels. The boxes represent the theoretical predictions with their uncertainties while the dots correspond to the experimental mass measurement.

where k is a constant whose approximate value is $1\,\mathrm{GeV\,fm}^{-1}$.

Assuming the quark quasi-static within the hadrons, the energy levels can be obtained by solving a nonrelativistic Schrödinger equation, then the states are characterized by the radial quantum number n and the relative angular momentum between quark and antiquark, L. Corrections of order (v/c^2), that are produced by spin-dependent interactions, give rise to splitting within multiplets.

States are described by the Russel-Saunders term symbols: orbital levels are labeled by ***S***,***P***,***D*** and the quark and antiquark spins add to give the total spin $S = 0$ (spin-singlet) or $S = 1$ (spin-triplet); S and L add to give the total angular momentum of the state, J. The parity of a quark-antiquark state with angular momentum L is $P = (-1)^{L+1}$ and the charge conjugation eigenvalue is given by $C = (-1)^{L+S}$. Therefore, quarkonium states are generally denoted by $^{2S+1}L_J$ with quantum numbers J^{PC}.

This description has proved reliable experimentally, in fact all charmonium states below the $D\bar{D}$ "open-charm" mass threshold[1] have been observed as predicted. They are relatively narrow $(0.1 - 0.3\,\mathrm{MeV}\,c^{-2})$ and decay through electromagnetic or hadronic transitions, so their quantum numbers, J^{PC}, can be inferred from the decay products. Charmonium states above the $D\bar{D}$ mass threshold can decay to $D\bar{D}$ final states. These resonances are wider and more difficult to measure since they have a larger variety of decay modes. The measurement described in this thesis fits within a broader, and currently active, effort in exploring experimentally charmonium-like mesons with masses above open-charm threshold.

1 value of mass ($\approx 3.7\,\mathrm{GeV}\,c^{-2}$) above which charmonium states are kinematically allowed to decay in charmed meson. These decays of charmonia are always favored by the OZI rule but prohibited by energy conservation below threshold.

1.4 BEYOND THE QUARK MODEL

With the realization of quantum chromodynamics, it was understood that the quark model is a simplified vision of the structure of hadrons. Hadrons are composed not only of their valence quarks, but must include virtual quark-antiquark pairs as well as gluons. The current understanding of QCD do not exclude a more complex description of hadrons than the rather simple classification in baryon and meson, adopted so far.

Starting from 2003, several unexpected resonances have been observed at the B-Factories and at the Tevatron. Most of them are narrow neutral hadrons that do not seem to fit conventional explanations based on the constituent-quark model. The spectroscopy of hadrons decaying in final states containing charmonium resonances and with masses in the range $3-5$ GeV c^{-2} has seen a revival and a lot of theoretical and experimental activity is being devoted to understand the phenomenology of these states. Their common features are that all have masses above the open charm threshold and they have large widths into charmonium final states. Due to their unknown nature, they are sometimes referred to as the XYZ mesons.

An experimental summary is given in the following and a few of those resonances are discussed in the remainder of this chapter together with the possible theoretical interpretations.

1.5 THE XYZ MESONS: EXPERIMENTAL OBSERVATIONS

The main properties of some of the XYZ states are summarized in table 4. The following description only concerns a few features that are useful for understanding the motivation of this work. More detailed information can be found in [5] and [6].

State	M (MeV c^{-2})	Γ (MeV c^{-2})	Production mode	Decay mode	Seen by
$X(3872)$	3871.5 ± 0.4	< 2.3	$B \to X(3872)K$	$J/\psi\pi^+\pi^-$	Belle, BaBar, CDF, DØ
$X(3875)$	3875.2 ± 0.7	$3.0^{+2.1}_{-1.7}$	$B \to X(3875)K$	$D^0\bar{D}^0\pi^0$,$D\bar{D}^*$	Belle, BaBar
$Z(3929)$	3929 ± 5	29 ± 10	$\gamma\gamma \to Z(3930)$	$D\bar{D}$	Belle
$X(3940)$	3943 ± 6	39 ± 26	$e^+e^- \to X(3940)J/\psi$	$D\bar{D}^*$	Belle
$Y(3940)$	3943 ± 17	87 ± 34	$B \to Y(3940)K$	$J/\psi\omega$	Belle, BaBar
$X(4160)$	4156 ± 29	139^{+113}_{-65}	$e^+e^- \to X(4160)J/\psi$	$D^*\bar{D}^*$	Belle
$Y(4008)$	4008^{+82}_{-49}	226^{+97}_{-80}	$e^+e^-(ISR)$	$J/\psi\pi^+\pi^-$	Belle
$Y(4260)$	4264 ± 12	83 ± 22	$e^+e^-(ISR)$	$J/\psi\pi^+\pi^-$	BaBar, Belle, CLEO
$Y(4350)$	4361 ± 13	74 ± 18	$e^+e^-(ISR)$	$\psi(2S)\pi^+\pi^-$	BaBar, Belle
$Y(4660)$	4664 ± 12	48 ± 15	$e^+e^-(ISR)$	$\psi(2S)\pi^+\pi^-$	Belle
$Z_1^+(4050)$	4051 ± 14	82^{+21}_{-17}	$B^0 \to Z_1^+(4050)K^-$	$\chi_{c1}\pi^+$	Belle
$Z_2^+(4250)$	4248^{+44}_{-29}	177^{+54}_{-39}	$B^0 \to Z_2^+(4250)K^-$	$\chi_{c1}\pi^+$	Belle
$Z^\pm(4430)$	4433 ± 5	45^{+35}_{-18}	$B \to Z^\pm(4430)K$	$\psi(2S)\pi^\pm$	Belle

Table 4: Summary of the main properties of some of the XYZ mesons.

1.5.1 X(3872)

The first of these new heavy hadrons observed is the $X(3872)$. It is a narrow state with a mass of roughly 3872 MeV c^{-2}. Given the observed final states and the observed mass,

in the charmonium region, it was assumed that the $X(3872)$ is itself a charmonium state. It has however proved difficult to identify the $X(3872)$ with any of the narrow $c\bar{c}$ mesons expected by the CQM model.

Discovery, confirmation and properties

The Belle collaboration in 2003 observed the $X(3872)$ in the decay $B^+ \to X(3872)K^+ \to J/\psi\pi^+\pi^-K^+$ [7]. In addition to the $\psi(2S)$, a second signal was seen in the $J/\psi\pi^+\pi^-$-mass distribution with high significance. Shortly after the Belle announcement, the Collider Detector at Fermilab (CDF) experiment confirmed the observation in high-energy proton-antiproton collision at the Fermilab Tevatron [8] (Fig. 3). Further observations were then reported by BaBar and DØ. The current world's average mass of the $X(3872)$ is (3871.4 ± 0.6) MeV c^{-2} and its total width is less than 2.3 MeV c^{-2}. All experiments observe a width consistent with experimental resolution. As the mass is higher than the $D\bar{D}$ open charm threshold, the $X(3872)$ narrow width suggests that decays to $D\bar{D}$ are suppressed.

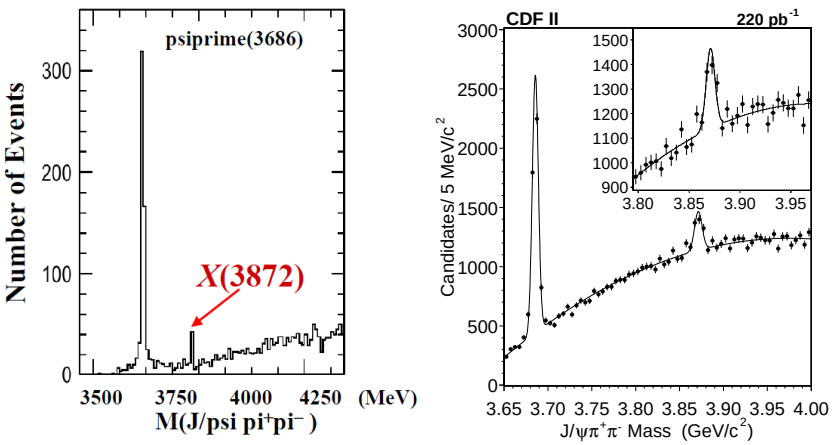

Figure 3: Left: $J/\psi\pi\pi$-mass distribution at Belle. The $X(3872)$ is visible as a narrow enhancement near the $\psi(2S)$ peak. Right: Distribution of the $J/\psi\pi^+\pi^-$ mass at CDF. The points represent data, the full line the total fit. The inset shows a magnification in the region of the $X(3872)$ signal.

Observations by Belle and BaBar of the decay $X(3872) \to J/\psi\gamma$ indicates the charge conjugation number $C = +1$ while studies from Belle and CDF combining angular information and the kinematic properties of the dipion pair rule out $J^{PC} = 0^{++}$ or 0^{-+} values and favor 1^{++} or 2^{-+} assignments. This implies that the dipion in the $X(3872) \to \pi^+\pi^-J/\psi$ has $C = -1$, consistent with the fact that the dipion mass distribution, measured at CDF suggests ρ resonance structure.

Neither of the available charmonium assignments with these J^{PC} values, the 1^{++} χ'_{c1} and the 2^{-+} η_{c2}, is expected to have a large branching fraction in the isospin violating $\rho J/\psi$ decay channel.

The $X(3872)$ is still the subject of intensive theoretical and experimental studies to shed light on its nature.

1.5.2 Other XYZ mesons

In the following years, several other charmonium-like states have been observed. Here is a brief report of their main features based on Godfrey and Olsen, *The Exotic XYZ Charmonium-Like Mesons* [5].

X(3940) and Y(3940)

The $X(3940)$ was observed by Belle in $e^+e^- \to X(3940)J/\psi$ with $X(3940) \to D^{*0}\bar{D}^0$ [9]. Its mass is (3943 ± 6) MeV c^{-2} and its width is (39 ± 26) MeV c^{-2}. Belle also set the 90% CL limits to the following branching ratios $B(X(3940) \to \omega J/\psi) < 0.26$ and $B(X(3940) \to D^{*0}\bar{D}^{*0}) > 0.45$.

Another state, the $Y(3940)$, was also discovered by Belle in $B \to Y(3940)K$ with $Y(3940) \to \omega J/\psi$ [10]. Its mass is compatible with the $X(3940)$: 3943 ± 17 MeV c^{-2}, but it is somewhat wider, with $\Gamma = (87 \pm 34)$ MeV c^{-2}. From the observed rates Belle determines

$$B(B \to Y(3940)K) \times B(Y(3940) \to \omega J/\psi) = (0.71 \pm 0.13 \pm 0.31) \times 10^{-4}$$

The $Y(3940)$ was later confirmed by BaBar, although with a lower mass ($3914.6^{+3.8}_{-3.4} \pm 1.9$ MeV c^{-2}) and width ($34^{+12}_{-8} \pm 5$ MeV c^{-2}) and a rate of

$$B(B^+ \to Y(3940)K^+) \times B(Y(3940) \to \omega J/\psi) = (0.49 \pm 0.10 \pm 0.05) \times 10^{-4}$$

in agreement with Belle. Consistent values of the observed masses suggest that the $X(3940)$ and the $Y(3940)$ may be the same state.

In addition, a third state with a similar mass, the $Z(3930)$ was discovered by Belle in two-photon collisions[2] $\gamma\gamma \to D\bar{D}$ with a mass of (3929 ± 5) MeV c^{-2} [11]. This particle is interpreted as the $\chi_{c2}(2P)$ charmonium state.

Y(4260)

The $Y(4260)$ was reported by BaBar as a broad $J^{PC} = 1^{--}$ resonance in the invariant mass spectrum of $J/\psi\pi^+\pi^-$ in $e^+e^- \to \gamma_{ISR}J/\psi\pi^+\pi^-$ initial state radiation events [12]. Their data can be modeled by a single resonance with a mass of about 4260 MeV c^{-2} and width of about 90 MeV c^{-2}, or by multiple narrow resonances that can't be resolved.

The $Y(4260)$ was confirmed by CLEO in ISR events [13], and by Belle [14], who also found a second cluster of events around 4.0 GeV c^{-2}, called $Y(4008)$.

Additional states observed through ISR include the $Y(4350)$ observed by BaBar and confirmed by Belle, and the $Y(4660)$ observed by Belle.

1.6 THE CHARGED STATE $Z^-(4430)$

All these observations, claimed in the recent years, were unexpected and do not fit easily with the charmonium description. Anyway, being neutral states, they can still be explained "stretching" the charmonium model with motivated modifications. The observation in 2007 of a new charged state, the $Z(4430)$ provided a real breakthrough in the spectroscopy of XYZ mesons since this state, being charged, cannot be interpreted as a charmonium state.

In mid-2007, Belle reported a study of the $B \to K\pi^-\psi(2S)$ decay where a narrow enhancement in the $\pi^-\psi(2S)$ mass distribution at $M = (4433 \pm 5)$ MeV c^{-2}(Fig. 7) was observed [2]. The natural width is compatible with zero and the B meson decay rate to this

2 Initial State Radiation (ISR), events where the interaction is between photons emitted from the electron and positron beams before the e^+e^- collision.

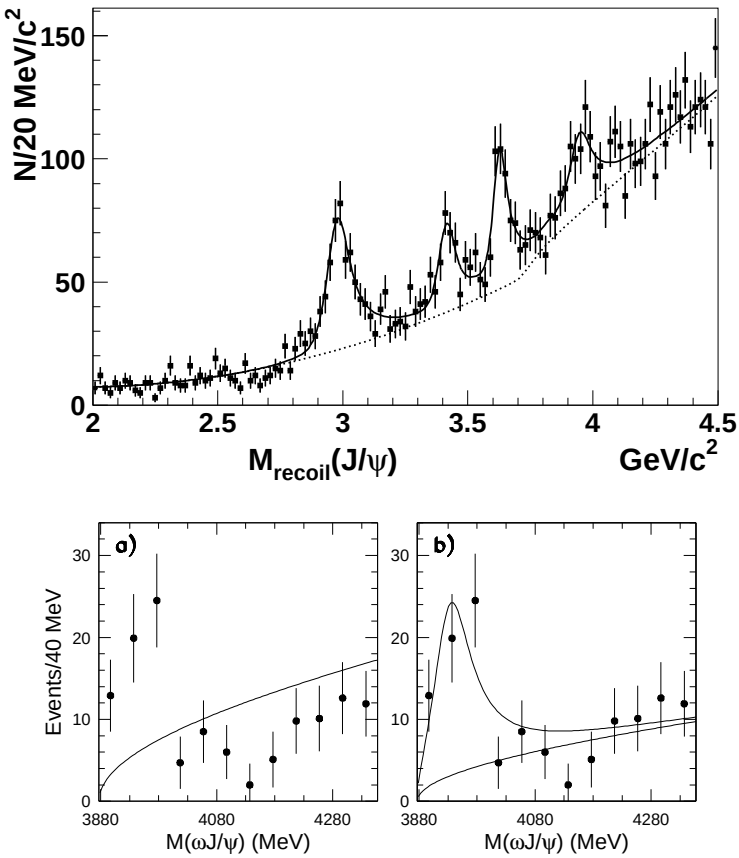

Figure 4: Top: distribution of the mass of the system recoiling against J/ψ in inclusive $e^+e^- \to J/\psi X$ events at Belle. The $X(3940)$ is visible as the enhancement just below 4 GeV c^{-2} in addition to previously reported η_c, $\chi_c 0$ and $\eta_c(2S)$ peaks. Bottom: $Y(3940)$ signal in the $\omega J/\psi$ mass distribution in $B \to \omega J/\psi K$ decays at Belle. The curve in (a) is the result of a fit that includes only a phase-space-like threshold function, while the curve in (b) also includes a Breit-Wigner resonance term.

state, which is called $Z^-(4430)$, is similar to that for the $X(3872)$ and $Y(3940)$, suggesting that the $Z^-(4430)$ has a substantial branching fraction to $\pi^-\psi(2S)$ and, thus, a partial decay width for this mode that is on the MeV scale. There have been no reports of a $Z^-(4430)$ in the $\pi^- J/\psi$ decay channel.

1.6.1 Belle analysis

The Belle experiment analyzed a sample of 657×10^6 $B\bar{B}$ pairs. They studied the $\pi^-\psi(2S)$ invariant mass distribution in $B^0 \to K^+\pi^-\psi(2S)$ and $B^- \to K^0_S\pi^-$ decays, where the $\psi(2S)$ decay either to l^+l^- or $\pi^+\pi^- J/\psi$ with $J/\psi \to l^+l^-$ ($l = e$ or μ). Both charged and neutral ($K^0_S \to \pi^+\pi^-$) kaons are used.

In the Dalitz plot (Fig. 8) of $M^2(K^+\pi^-)$ *vs* $M^2(\pi^-\psi(2S))$ for the $B^0 \to K^+\pi^-\psi(2S)$ candidate events a narrow band at $M^2_{K^+\pi^-} \simeq 0.8\ GeV^2$, corresponding to $B^0 \to K^*(892)^0[\to K^+\pi^-]\psi(2S)$, is evident. There are also indication of a broader $K^*(1430)^0$ signal near $M^2_{K^+\pi^-} = 2.0\ GeV^2$. The events in these two regions of the Dalitz are excluded from the analysis.

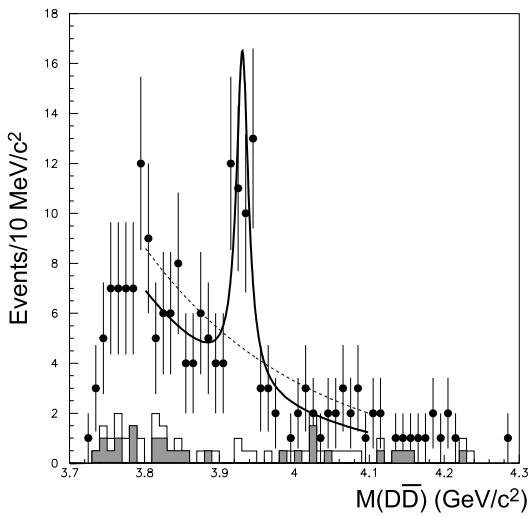

Figure 5: The m($D\bar{D}$) distribution with the $D^0\bar{D}^0$ and D^+D^- modes at Belle. The curves show the fits with (solid line) and without (dashed line) a $Z(3930)$ resonance component. The histogram shows the distribution from the D-mass sidebands.

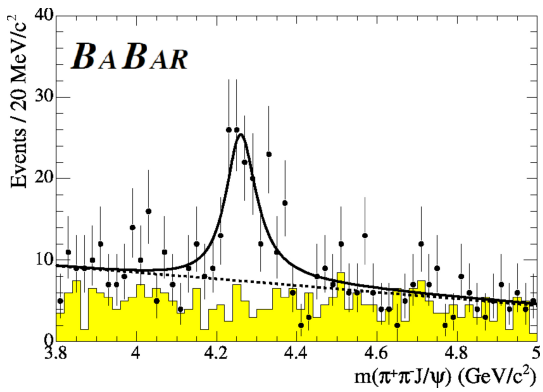

Figure 6: Distribution of the $J/\psi\pi^+\pi^-$ invariant mass at BaBar. The points with error bars represent data and the shaded histogram shows the distribution from the J/ψ-mass sidebands. The solid curve shows the result of the $Y(4260)$ resonance fit; the dashed curve represents the background component.

With these selections Belle observed a relatively narrow peak in the $\pi^-\psi(2S)$ mass distribution at $M = (4433 \pm 4(stat) \pm 2(syst))$ MeV c^{-2} with width $\Gamma = 45^{+18}_{-13}(stat)^{+30}_{-13}(syst)$ MeV c^{-2} and significance of 6.5σ.

The branching fraction was measured using only the signal from neutral B-mesons.

$$B(B^0 \to Z^-K^+, Z^- \to \psi(2S)\pi^-) = (4.1 \pm 1.0(stat) \pm 1.4(syst)) \times 10^{-5}$$

In a subsequent analysis Belle performed a detailed study of the Dalitz plot, and confirmed the observation with a slightly adjusted significance of 6.4σ.

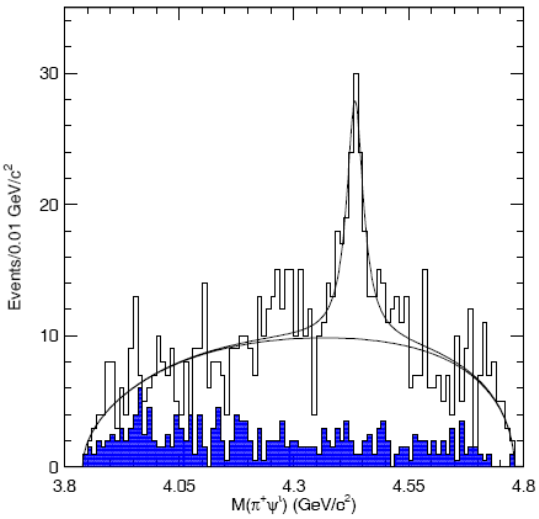

Figure 7: The $\pi^-\psi(2S)$ invariant mass distribution for $B \to K\pi^-\psi(2S)$ decays at Belle.

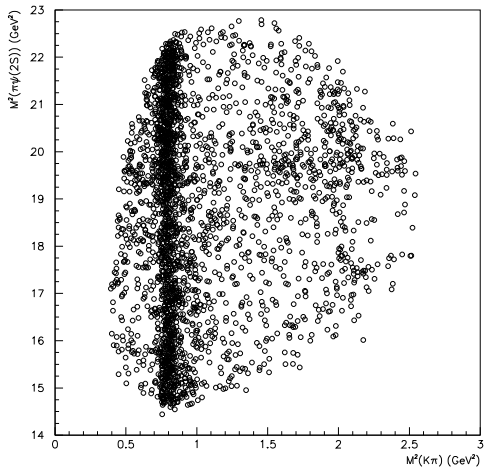

Figure 8: Dalitz plot of the $B^0 \to \psi(2S)K^+\pi^-$ decay with $M^2(\psi(2S)\pi^-)$ (vertical) vs $M^2(K^+\pi^-)$ (horizontal) from Belle.

1.6.2 BaBar analysis

After the surprising Belle's discovery, in 2008, the BaBar collaboration reported its own search for $Z^-(4430)$ mesons using 455×10^6 $B\bar{B}$ pairs [15], a data sample significantly smaller than Belle's sample. They considered the decay of the $Z^-(4430)$ to $J/\psi\pi^-$ or $\psi(2S)\pi^-$ in $B \to J/\psi\pi^-K$ and $B \to \psi(2S)\pi^-K$ decays.

Applying an event selection similar to the Belle's one they saw no significant evidence for a $Z^-(4430)$ signal for any of the processes investigated in the total $J/\psi\pi^-$ or $\psi(2S)\pi^-$ mass distribution, nor in the corresponding distributions for the regions of $K\pi^-$ mass

for which observation of the $Z^-(4430)$ signal was reported by Belle. BaBar found that the $J/\psi\pi^-$ mass distribution is compatible with the simulations of background while in the $\psi(2S)\pi^-$-mass distribution a 2.7 standard deviation excess is present but at a slightly different mass, $\approx 43\,\mathrm{MeV}\,c^{-2}$ higher (4.7σ) than Belle's measurement. BaBar estimated the following upper limits for the branching fractions at 95% confidence level: $B(B^- \to Z^-\bar{K}^0, Z^- \to J/\psi\pi^-) < 1.5 \times 10^{-5}$, $B(B^0 \to Z^-K^+, Z^- \to J/\psi\pi^-) < 0.4 \times 10^{-5}$, $B(B^- \to Z^-\bar{K}^0, Z^- \to \psi(2S)\pi^-) < 4.7 \times 10^{-5}$, $B(B^0 \to Z^-K^+, Z^- \to \psi(2)\pi^-) < 3.1 \times 10^{-5}$. These limits are still compatible with the rate measured by Belle.

1.7 XYZ EXOTIC STATES: THEORETICAL MODELS

The experimental observation of the states described above challenges the Quark Model. Hadrons like the XYZ particles have features recalling the charmonium phenomenology (mass, decays) but not supported by the expected structure (spin, CP quantum numbers) for a $c\bar{c}$ state. The development of numerical lattice QCD provides the tools to build alternative models or expansion of the CQM, but until now, there were few experimental results supporting the need for a stronger effort in understanding charmonium spectroscopy above the open-charm threshold.

Many theoretical models have been developed, prompted by the recent experimental discovery. We will briefly outline in the following some of the most popular interpretations that have been proposed to understand the phenomenology of XYZ states.

Threshold effect

This description is applied to resonances with mass compatible with a $D\bar{D}$ system. In particular, it was proposed as a possible explanation for the $X(3872)$. It suggests that the observed signals originate from dynamical effect, not as bound states but as virtual states, caused by the proximity to the open-charm threshold. When two charmed mesons are produced in a small phase-space region, they may interact exchanging pions. The force can be attractive but the interaction is not strong enough to form a bound state. However it has been argued that this may produce structures in the cross sections and mass distributions similar to the ones observed by experiments [16].

Charmonium hybrids

A possible interpretation for some of this resonances could be found in the Charmonium Hybrids model. A hybrid state $q\bar{q}g$ resulting from a combination of $(q\bar{q})_8$, a quark and an anti-quark in color-octet, with an excited gluon was proposed. Such states would have exotic quantum numbers, not consistent with the constituent quark model, thus explaining some of the observed resonances. For instance the $Y(4260)$ could fit this model; since this state wasn't observed in open charm decays even if its mass is greater than the $D\bar{D}$ threshold, it was proposed that it may be a $c\bar{c}g$ hybrid meson.

However, lattice QCD predicts the lowest charmonium hybrid states to have masses of roughly $4200\,\mathrm{MeV}\,c^{-2}$ and a $c\bar{c}g$ description could not model a charged state. Therefore, this model cannot explain all the XYZ particles.

Multiquark states

The models described above are extensions of the charmonium interpretation and not prescribe aggregates of quarks invoking more than a $q\bar{q}$ pair. The fact that some characteristics of the observed exotic states seem to exclude a charmonium-like description, with a single $c\bar{c}$ pair, has stimulated construction of more complex model, which depart more

significantly from the charmonium interpretation and allow for bound states of more than two quarks. These have been further motivated by the observation of a charged state, which would definitively suggest multiquark interpretations. Many variant of multiquark models have been proposed, but they can be roughly classified into two broader classes: molecules and tetraquarks.

MOLECULE: It is a resonance formed by two charmed mesons loosely bound together. There are two different mechanisms that contribute to the bond: residual quark-color interactions at short distance and pion exchange at large distance. Molecular states are not isospin eigenstates and their distinctive decay pattern tend to be the sum of the two mesons inside the molecule. In fact they are weakly bound and tend to decay as if they are free. The $X(3872)$ qualify as a molecule-like bound state of a D^0 and a D^{*0} meson, since its mass is nearly equal to the sum of the two charmed mesons; on the other hand, the high production rate measured at CDF seem not to be consistent with the constraint imposed by the molecular interpretation. So far, it has not been possible to produce predictions of possible molecular state with well-defined mass values, due to the large number of degrees of freedom of this model.

TETRAQUARK: This second type of multiquark is, instead, a tightly bound four-quark state. The tetraquark can be described as a diquark-diantiquark structure in which the quarks group into color-triplet scalar and vector clusters. The dominating interaction is a simple spin-spin interaction. Decays are expected to proceed via rearrangement processes, followed by dissociation, so that final state with charmonium states are possible. This model also allow description of multiplets with nonzero charged members, unlike the standard charmonium spectrum or the charmonium hybrids.

Implications for the $Z^-(4430)$

The $Z^-(4430)$ has a nonzero electric charge, which is not possible for $c\bar{c}$ charmonium states or $c\bar{c}$-gluon hybrid mesons. It is, therefore, a prime candidate for a multiquark meson. Maiani et al. [17] suggest that the $Z^-(4430)$ is a diquark-antidiquark state with flavor $[cu][\bar{c}\bar{d}]$ and is the radial excitation of an $X^-_{ud}(1^{+-};1S)$ state with mass 3880 MeV c^{-2}. The tetraquark hypothesis suggests that the $Z^-(4430)$ will have neutral partners decaying to $\psi(2S)+\pi^0/\eta$ or $\eta_c(2S)+\rho^0/\omega$. If the $Z^-(4430)$ is a molecule, assuming that $D^*\bar{D}_1$ in S-wave, it will have $J^P = 0^-$, 1^- or 2^-, with the lightest state expected to e 0^-. In contrast, a tetraquark would have $J^P = 1^+$. The molecule would decay via the decay of its constituent mesons into $D^*D^*\pi$, whereas the tetraquark would fall apart into $D\bar{D}^*$, $D^*\bar{D}^*$, $J/\psi\pi$, $J/\psi\rho$, $\eta_c\rho$, and $\psi(2S)\pi$ - but not into $D\bar{D}$ due to its unnatural spin parity.

In conclusion, no single model seems to be able to successfully describe in a complete and consistent manner the whole phenomenology of the observed XYZ states. An intense experimental and theoretical activity is ongoing and will hopefully provide a more complete understanding in the next few years.

1.8 EXPERIMENTAL ASPECTS

The largest experimental contribution to the spectroscopy of the XYZ mesons came from e^+e^- machines operating at the $\Upsilon(4S)$ resonance (B-Factories). Some other contributions came from the Tevatron, which is a hadron collider, and are likely to come soon from Large Hadron Collider (LHC), another hadron collider. In the following, we discuss the peculiar features of the hadronic environment and compare them with their e^+e^- counterparts. This may provide a better understanding of the experimental difficulties encountered in the measurements presented in this thesis, and of the strategy adopted to overcome them.

1.8.1 The B-Factories

Following the original 1987 proposal by Oddone, the latest evolution of accelerators for the study of flavor physics are the B-Factories: high-luminosity e^+e^- colliders with asymmetric beam energies that produce $\Upsilon(4S)$ resonances with $0.4 - 0.6$ Lorentz boost. The $\Upsilon(4S)$ meson decay 96% of the times into $B\bar{B}$ pairs ($B = B^0$ or B^+) which in turn decay in vertices typically spaced apart by $200 - 300\,\mu\text{m}$. Since the decay of the b quark into charm is favored by the quark-mixing matrix, the production rate of charmonium-like intermediate states may be large. Operating the colliders at an energy corresponding to the $\Upsilon(4S)$ resonance, just above the open beauty threshold, reduce backgrounds because of tight kinematic constraints and absence of fragmentation products.

The experiments installed at the B-Factories (BaBar and Belle) were large-acceptance asymmetric spectrometers with excellent performance in reconstructing charged-particle trajectories (silicon micro-vertex detectors plus drift chambers with helium-based gas admixtures in 1.5 T magnetic fields), that allowed discrimination of heavy-flavor decay vertices. Redundant information from silica quartz (BaBar) or aerogel (Belle) Cerenkov counters, time-of-flight detectors, thallium-doped cesium iodide electromagnetic calorimeters, and the outermost layers of muon detectors allow identification of muons, electrons and hadrons.

Both Belle and BaBar have ceased their operation, in 2010 and 2008, after collecting 779 and 467 million of $B\bar{B}$ pairs respectively.

1.8.2 The hadron collider environment

The primary advantage of high-energy hadron colliders in this physics is the large cross-section for heavy-flavor production. At the Fermilab Tevatron $p\bar{p}$ collider, the dominant production process is non-resonant incoherent b-quark or c-quark pair-production of the type $p\bar{p} \to q\bar{q}X$ with cross sections of the order $10 - 100\,\mu\text{b}$. This is large compared with production cross-sections at e^+e^- machines (1 nb at the $\Upsilon(4S)$ resonance).

However, the hadron collider environment has its disadvantages. The large heavy-flavor cross-section is still about three order of magnitudes smaller than the $p\bar{p}$ inelastic cross-section. This poses a challenging task for the trigger systems. In this respect, the component of momentum of heavy-flavor hadrons perpendicular to the beam line (transverse momentum) provides a first discrimination from light-quark background, generally distributed at lower values. But the transverse momentum distribution of heavy-flavor hadrons is a rapidly falling function: most of them have low transverse momenta and decay into particles often having $p_T < 1\,\text{GeV}\,c^{-1}$. The need to select low-momentum particles conflicts with the accept-rate limitations of the data acquisition systems. Furthermore, since the longitudinal component of momenta is frequently large, their decay products tend to be boosted along the beam direction, thus escaping the detector acceptance.

Reconstruction of heavy flavor decays in a hadron collider is also plagued by complex event structures. Different sources contribute particles entering the detector acceptance in each collision.

HARD INTERACTION – in most hard $p\bar{p}$ interactions, only one proton constituent (a valence — u, d — or a "sea" quark, or a gluon) undergoes hard-scattering against one antiproton constituent. This two-to-two parton scattering is the leading interaction that may produce the heavy-flavor pair and additional particles through initial and final state radiation.

UNDERLYING EVENT – when a hard collision occurs, the remnants of proton and antiproton rearrange in color-neutral hadrons which may have a momentum perpendicular to the beam sufficient to enter the detector acceptance. The underlying event also includes the products of multiple parton interactions, i. e., multiple hard-scattering between different constituents of the same $p\bar{p}$ pair.

HADRON FRAGMENTATION PROCESS – quarks are never observed as independent entities, but are confined inside hadrons. Fragmentation (or hadronization) is the long-distance, non-perturbative QCD process of transition from a single, final-state quark to an observable color-singlet hadron. In this process, a number of accompanying hadrons is produced in a local region around the hadronizing quark, as a result of the fragmentation of color lines of strong force.

PILE-UP EVENT – when a beam of protons crosses a beam of antiprotons, multiple hard interactions may occur between different proton-antiproton pairs. Each hard interaction contribute with an associated fragmentation process and underlying event.

Occasionally, products of interactions of the beams with residual gas contaminating the vacuum of the beam-pipe add to the above sources. As a consequence, in a $p\bar{p}$ collider as the Tevatron, high particle multiplicities per event are observed ($\mathcal{O}(100)$ charged particles with $p_T \gtrsim 300\,\mathrm{MeV}\,c^{-1}$), with multiple production vertices, and event shapes lacking well-defined structures. In hadron-hadron collisions, therefore, extraction of heavy-flavor signals from the large background is the first experimental challenge.

The next chapter describes in detail the Tevatron collider and the CDF experiment.

2 THE UPGRADED COLLIDER DETECTOR AT THE FERMILAB TEVATRON

The analysis reported in this thesis is based on data produced in proton-antiproton collisions at a center of mass energy of 1.96 TeV. The collision products and their properties are inferred from the measurements on the "stable" particles that interact with the detector instrumentation.[1]

This chapter provides a concise description of the complex infrastructure, accelerator and detector, involved in producing our data sample. A more detailed description of the tracking and the muon detection systems is given, for the crucial role they have in the present analysis.

2.1 THE FERMILAB TEVATRON COLLIDER

The Tevatron collider is an accelerator that provides collisions of antiprotons with protons at a center-of-mass energy of 1.96 TeV. The Tevatron is an underground circular proton synchrotron, 1 km in radius, at the last stage of a system of accelerators, storage rings, and transfer lines located at the Fermi National Accelerator Laboratory (Fermilab) about 50 km west from Chicago. While the machine operates in collider mode, "bunches" of protons, circulating clockwise (as seen from above) and spaced by 396 ns, collide against a similar beam of antiprotons accelerated counter-clockwise, both at energies of 980 GeV. A bunch is a collection of particles contained within one radio-frequency "bucket" (defined below).

The Tevatron was commissioned in 1983 as the first large-scale superconducting synchrotron in the world and, since then, various periods of operations occurred. Each extended period of Tevatron collider operations is conventionally identified as a Run.[2] Table 5 contains a summary of the Tevatron operations and performance since its construction. The present analysis uses the data collected in Run II.

The performance of the Tevatron collider is evaluated in terms of two key parameters: the available center-of-mass energy, $\sqrt{s}$, and the instantaneous luminosity, $\mathscr{L}$. The former defines the accessible phase-space for the production of resonances in the final states. The latter is the coefficient of proportionality between the rate of a given process and its cross-section σ:

$$\text{rate [events s}^{-1}] = \mathscr{L}\,[\text{cm}^{-2}\,\text{s}^{-1}] \times \sigma\,[\text{cm}^2]\,. \tag{2.1}$$

The time-integral of the eq. (2.1) is therefore a measure of the expected number of events n, produced in a finite time T:

$$n(T) = \int_0^T \mathscr{L}\sigma\,dt\,, \tag{2.2}$$

while the time-integral of the luminosity is the integrated luminosity:

$$\mathscr{L}_{\text{int}} = \int_0^T \mathscr{L}\,dt\,. \tag{2.3}$$

1 Stable in this context refers to particles (μ, K, π) whose lifetime and typical transverse momenta at CDF are such that they traverse a fraction of the active material sufficient to reconstruct their trajectory.

2 The Run is not to be confused with the *run*, defined in CDF as a continuous period of data-taking in approximately constant detector and beam conditions.

Date		$\sqrt{s}$ [TeV]	$\mathscr{L}$ [cm^{-2} s^{-1}]	$\int \mathscr{L}\, dt$ [pb^{-1}]
Mar 1983	End of the construction	–	–	–
Jul 1983	Proton energy: 512 GeV	–	–	–
Oct 1983	Fixed-target program	–	–	–
Feb 1984	Proton energy: 800 GeV	–	–	–
Oct 1985	First $p\bar{p}$ collisions	1.6	10^{24}	–
Oct 1986	Proton energy 900 GeV	–	–	–
Jun 1988–May 1989	Run 0	1.8	2×10^{30}	$\simeq 4.5$
Aug 1992–Feb 1996	Run I	1.8/0.63	28×10^{30}	$\simeq 180$
Aug 2000	Beam energy: 980 GeV	–	–	–
Mar 2001	Run II start	1.96	5×10^{30}	–
Jul 2010	Best performances	1.96	4.02×10^{32}	$\simeq 6900$

Table 5: Chronological overview of the Tevatron operation and performance. The fourth column reports the peak luminosity. The fifth column reports the delivered integrated luminosity. The last row shows the best performances as of this writing.

Assuming an ideal head-on $p\bar{p}$ collision with no crossing angle between the beams, the instantaneous luminosity is defined as

$$\mathscr{L} = 10^{-5} \frac{N_{\mathrm{p}} N_{\bar{\mathrm{p}}} B f \beta\gamma}{2\pi\beta^{\star}\sqrt{(\epsilon_p + \epsilon_{\bar{p}})_x (\epsilon_p + \epsilon_{\bar{p}})_y}} \mathcal{H}(\sigma/\beta^{\star}) \qquad [10^{30}\,\mathrm{cm}^{-2}\,\mathrm{s}^{-1}]\,. \tag{2.4}$$

It depends on the following Tevatron parameters: the number of circulating bunches in the ring ($B = 36$), the revolution frequency ($f = 47.713$ kHz), the Lorentz relativistic factor (boost, $\beta\gamma = 1045.8$ at 980 GeV), the average numbers of protons ($N_{\mathrm{p}} \approx 250 \times 10^9$) and antiprotons ($N_{\bar{\mathrm{p}}} \approx 10^9$) in a bunch, an empiric "hourglass" factor ($\mathcal{H} = 0.6 - 0.7$), which is a function of the ratio between the longitudinal r.m.s. width of the bunch ($\sigma_z \approx 60$ cm) and the "beta function" calculated at the interaction point ($\beta^{\star} \approx 31$ cm), and the 95% normalized emittances of the beams ($\epsilon_{\mathrm{p}} \approx 18\pi$ mm mrad and $\epsilon_{\bar{\mathrm{p}}} \approx 13\pi$ mm mrad after injection).[3] The dominant limiting factor of the luminosity is the availability of monochromatic antiprotons that can be efficiently transferred through the accelerator chain for final collisions.

The Tevatron is an approximately circular synchrotron employing 772 dipole, 2 half-dipole, and 204 quadrupole superconducting magnets. Each is approximately 6 m long, 4 tons in mass, and is made of NbTi alloy filaments embedded in copper, kept at 4.3 K temperature by a large cryogenic system. A 4400 A current flows through each magnet to produce the 4.2 T magnetic field necessary to keep the particles on their orbit, while they are accelerated by eight radio-frequency (RF) cavities driven at approximately 53.105 Hz. Motions or friction by the approximately 4000 N cm^{-1} of outward pressure are avoided by epoxy-covered steel collars bound around the magnets.

The particles are accelerated through the RF buckets. A bucket is one interval of the longitudinal restoring force provided by the RF cavities that results in a stable phase-space where a bunch may be captured and accelerated. In the following, we describe the procedure for obtaining a continuous period of collider operation using the same collection of protons and antiprotons, called a store. Further details can be found in ref. [18].

3 The hourglass factor is a parameterization of the longitudinal profile of the beams in the collision region, which assumes the shape of an horizontal hourglass centered in the interaction region. The beta function is a parameter convenient for solving the equation of motion of a particle through an arbitrary beam transport system. The emittance ϵ measures the phase-space occupied by the particles of the beam. Three independent two-dimensional emittances are defined. The quantity $\sqrt{\beta\epsilon}$ is proportional to the r.m.s. width of the beam in the corresponding phase plane.

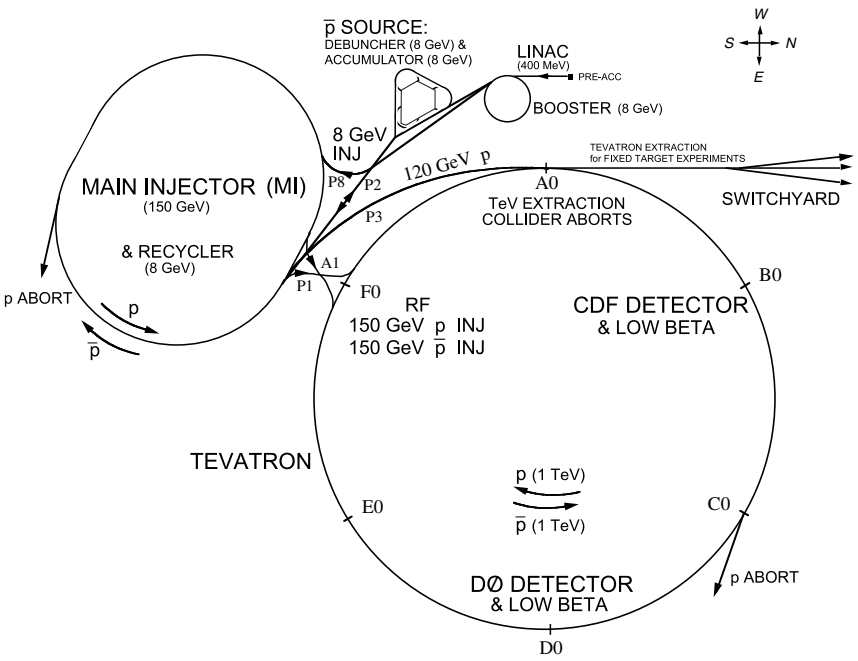

Figure 9: Illustration of the Fermilab Tevatron collider.

2.1.1 Proton production

Hot hydrogen gas is passed through a magnetron, which extracts a 50-55 mA current of 15–22 keV H^- ions, subsequently accelerated every 66 ms to 750 keV by a three-staged diode-capacitor voltage multiplier (Cockroft-Walton) accelerator. The proton beam, segmented into bunches, is then injected into a two-staged 150 m long linear accelerator (Linac, see fig. 9). First, a drift tube accelerator resonating at 201.249 MHz accelerates bunches of protons up to 116 MeV; then, a side-coupled cavity accelerator at 804.996 MHz increases their energy to 401.5 MeV before injection into the Booster.

The Booster (see fig. 9) is an alternating gradient synchrotron (orbit radius of 75.5 m) that accelerates protons to 8 GeV in 33 ms, sweeping from 38 to 53.105 MHz. At injection, a thin carbon foil is used to strip the electrons from the H^- ions to obtain protons. Injecting H^- ions rather than protons into the Booster allows the injection to proceed over multiple revolutions of the beam around the Booster Ring (usually 10-12). If protons were instead injected, the magnetic field used to inject new protons onto orbit in the Booster would also deflect the already revolving protons out of orbit. There are two basic modes during collider operations: antiproton accumulation and injection.

2.1.2 Antiproton production and accumulation

In accumulation mode, one set of 84 proton bunches (approximately 8×10^{12} p in total) is extracted from the Booster at 8 GeV and injected into the Main Injector every 2.2 s. The Main Injector (see fig. 9) is a 53.105 MHz circular synchrotron (528.5 m in radius), with 18 accelerating cavities and conventional magnets. The protons are accelerated to 120 GeV, and then extracted and directed to the antiproton production station, a rotating 7 cm-thick target made of nickel alloys containing chromium, iron and other metals.

The particles produced in the interaction are spatially wide-spread. They are collected and focused with a cylindrical lithium lens ($760\,\mathrm{T\,m^{-1}}$).[4] Negatively-charged secondaries at $8\mathrm{GeV}\,c^{-1}$ are momentum-selected by a 1.5 T pulsed dipole magnet. Typically, 21 antiprotons are collected for each 10×10^6 protons on target, resulting in a stacking rate of approximately 10–20 $\mathrm{mA\,h^{-1}}$. The emerging antiprotons have a bunch structure similar to the one of the incident protons and are delivered to the Debuncher storage ring (see fig. 9).

This rounded triangular synchrotron, 90 m of mean radius, transforms the antiproton pulses in a continuous beam of monochromatic antiprotons. Stochastic cooling and bunch rotation are applied during many cycles.[5] From the Debuncher, $8\,000 \pm 0\,018$ GeV antiprotons are transferred with $60 - 70\%$ efficiency into the Accumulator, a concentric storage ring 75 m in mean radius (see fig. 9), where they are stacked and cooled with a variety of systems until the maximum antiproton intensity is reached. Since 2004, optimized antiproton accumulation is achieved using the Recycler Ring (see fig. 9). This is a constant 8 GeV energy storage-ring placed in the Main Injector enclosure, that uses permanent magnets. It is used to gather antiprotons that are periodically transferred from the Accumulator (95% transfer efficiency) thus maintaining it at its optimum intensity regime. Recently, relativistic electron cooling was successfully implemented in the Recycler, further enhancing the Tevatron performance [20].[6]

2.1.3 Injection and collisions

Every 10-20 h, antiproton accumulation is stopped in preparation for injection. A set of seven proton bunches is extracted from the Booster, injected into the Main Injector, accelerated to 150 GeV, coalesced with $\approx 90\%$ efficiency into a single bunch of $\approx 300 \times 10^9$ p, and then injected into the Tevatron.[7] This process is repeated every 12.5 s, until 36 proton bunches, separated by 396 ns, are loaded into the Tevatron central orbit. Typically, 65% of the protons in the Main Injector are successfully transferred to the Tevatron. The electrostatic separators (about 30 pairs of metal plates) are then activated in the Tevatron, in preparation for antiproton injection.

Four sets of 7-11 $\bar{\mathrm{p}}$ bunches are extracted from the Accumulator (or from the Recycler) to the Main Injector, accelerated to 150 GeV, coalesced with $\approx 80\%$ efficiency into four $\approx 30 \times 10^9$ $\bar{\mathrm{p}}$ bunches separated by 396 ns, and then injected into the Tevatron, where protons are counter-rotating. Protons and antiprotons circulate in the same enclosure, sharing magnet and vacuum systems. The separators minimize the beam-beam interactions, by keeping the proton and the antiproton beams, each about half a millimeter thick, into two non-intersecting closed helical orbits separated by approximately five millimeters ($3 - 5\sigma$) as they revolve in opposite directions. This allows controlling each beam nearly independently. The injection process is repeated nine times until 36 antiproton bunches circulate in the Tevatron.

Sweeping the Tevatron RF by ≈ 1 kHz, the beam is then accelerated in about a minute from 150 to 980 GeV, at which energy one proton completes the full revolution of the Tevatron circumference in 21 µs at $0.999\,999\,6\,c$. The beams are finally brought into collision at the two instrumented interaction-points located along two straight sections of the Tevatron: DØ and BØ, where the DØ and CDFII detectors, respectively, are located.

4 Lithium is used to minimize beam loss from multiple-scattering.

5 *Stochastic cooling* is a technique used to reduce the transverse and energy spread of a particle beam without any accompanying beam-loss. This is achieved by applying iteratively a feedback mechanism that senses with extreme sensitivity the beam deviation from the ideal orbit with electrostatic plates, processes and amplifies it, and transmits an adequately-sized synchronized correction pulse to another set of plates downstream [19]. Bunch rotation is an RF manipulation technique that, using adequate phasing, transforms a beam with a large time spread and a small energy spread in a beam with a large energy spread and a small time spread, or vice versa.

6 Electron cooling is a method of damping through the interaction between the antiproton beam and an electron beam propagating together at the same average velocity.

7 Coalescing is the process of compacting into one dense bunch many smaller bunches.

Although the power produced in the collision is only 1–2 W, the stored energy of the beam is about 1.7 MJ, corresponding, approximately, to the kinetic energy of a 4.5 t truck moving at 100 km h^{-1}.

Special high-power quadrupole magnets ("low-β squeezers"), installed on the beam pipe at either side of the detectors, reduce the transverse spatial spread of the beams to maximize the collision rate in the interaction regions. The resulting transverse spatial distribution of the luminous region is approximately a two-dimensional Gaussian, with $\sigma_T \approx 30\,\mu$m. The typical longitudinal dimension of a bunch is 60–70 cm. The interaction regions have a roughly Gaussian distribution along the beam direction, with r.m.s. width $\sigma_z \approx 28$ cm. The center of the luminous region is shifted toward the nominal interaction point by fine tuning of the squeezers. The 36 bunches of protons (antiprotons) are distributed among the 1113 buckets in three equally spaced "trains" of 12 bunches each. The inter-bunch spacing is 396 ns (21 buckets) within a train, while a 2.6 µs spacing (139 buckets, "abort gap") is kept between trains. The abort gap allows antiprotons injection (in coincidence with the proton abort gap) without perturbing the already revolving protons with the injecting magnet. Furthermore, when beam abortion is needed, the abort gap allows ramping-up the deflecting magnets without interfering with the beam during the transient, possibly damaging the detectors. As a consequence of this bunch distribution, the average bunch-crossing rate is 1.7 MHz, resulting from a 2.53 MHz rate, when the proton and antiproton trains are crossing, and zero rate in correspondence of the abort gaps.

The transverse profile of the beam is shaped to its optimized configuration to avoid detector damage from the tails of the p ($\bar{\text{p}}$) distributions interacting with the beam pipe: retractable collimators (iron plates) are moved perpendicularly toward the beam and trim-off the residual halo. When the beam profile is narrow enough and the conditions are safely stable, the detector is powered and the data-taking starts.

The number of overlapping inelastic interactions N for each bunch crossing is a Poisson-distributed variable that depends on the instantaneous luminosity. The observed distribution of the multiplicity of interaction vertices yields $\bar{N} \approx 0.2$, 1.0, 2.0, and 6.0 for respectively, $\mathscr{L} \approx 1 \times 10^{31}$, 5×10^{31}, 10×10^{31}, and 30×10^{31} luminosities. The luminosity decreases as a function of time during the store because of the interactions of the beam with residual molecules of gas that escaped the vacuum of the beam pipe, beam-halo interactions, and $\bar{\text{p}}$ depletion due to the collisions. During the 10–20 h of a store, the luminosity decreases by a factor of 5–15. Just after the final injection, a new antiproton accumulation cycle is started. When the antiproton stack is sufficiently large and the colliding beams are degraded, the detector high-voltages are switched-off and the store is dumped. The beam is extracted via a switch-yard and sent to an absorption zone.

Beam abortion can occur also accidentally when a superconducting magnet rises its temperature above the critical value (*i. e.*, the magnet "quenches"), destroying the orbit of the beams. The lapse between the end of a store and the beginning of collisions of the next one is typically 1 h, during which time calibrations of the sub-detectors and cosmic rays tests are usually performed.

2.1.4 Tevatron performance

In Run II the Tevatron is running at an center-of-mass energy of 1.96 TeV with an inter bunch-crossing time of 396 ns. Its performance in terms of luminosity has been steadily improving.

Currently it has the record of highest peak luminosity for a hadron collider of 4.02×10^{32} cm^{-2} s^{-1}. As of June 2010, physics quality data corresponding to 6.9 fb^{-1} are stored. The plot in fig. 10 shows the integrated luminosity since the beginning of Run II.

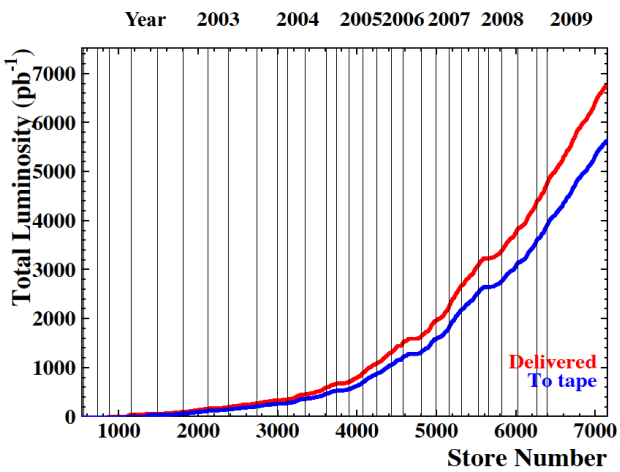

Figure 10: Integrated Luminosity since the beginning of Run II.

2.2 THE CDF II DETECTOR

The CDF in Run II (CDFII) detector is a large multi-purpose solenoidal magnetic spectrometer surrounded by 4π fast, projective calorimeters and fine-grained muon detectors. It is installed at the BØ interaction point of the Tevatron (see fig. 11) to determine energy, momentum and the identity of a broad range of particles produced in 1.96 TeV $p\bar{p}$ collisions. It was designed, built, and operated by a team of physicists, technicians, and engineers that, as of this writing, spans 60 institutions of 14 countries. Several upgrades modified the design of the original facility commissioned in 1985.[8] The most extensive upgrade started in 1995 and led to the current detector whose operation is generally referred to as CDFII.

2.2.1 Coordinates and notation

CDFII employs a right-handed Cartesian coordinate system with origin in the BØ interaction point, assumed coincident with the center of the drift chamber (see sec. 2.3.5). The positive z-axis lies along the nominal beam-line pointing toward the proton direction (east). The (x, y) plane is therefore perpendicular to either beams, with positive y-axis pointing vertically upward and positive x-axis in the horizontal plane of the Tevatron, pointing radially outward with respect to the center of the ring.

Since the colliding beams of the Tevatron are unpolarized, the resulting physical observations are invariant under rotations around the beam line axis. Thus, a cylindrical (r, φ, z) coordinate system is particularly convenient to describe the detector geometry. Throughout this thesis, *longitudinal* means parallel to the proton beam direction (i. e. to the z-axis), and *transverse* means perpendicular to the proton beam direction, i. e. in the $(x, y) \equiv (r, \varphi)$ plane.

In hadron collisions the longitudinal momentum of the colliding partons is unknown on an event-by-event basis. It is customary to use a variable invariant under $\hat{z}$ boosts as an unit of relativistic phase-space, instead of the polar angle θ. This variable is the *rapidity* defined as

$$Y = \frac{1}{2} \ln \left[\frac{E + p\cos(\theta)}{E - p\cos(\theta)} \right], \tag{2.5}$$

8 Originally, the CDF acronym was meant for Collider Detector Facility.

where $(E, \vec{p})$ is the energy-momentum four-vector of the particle. However, a measurement of rapidity still requires a detector with accurate particle identification capabilities because of the mass term entering E. Thus, for practical reasons, it is often preferred to replace Y with its approximate expression η in the ultra-relativistic limit, usually valid for products of high-energy collisions:

$$Y \xrightarrow{p \gg m} \eta + \mathcal{O}(m^2/p^2), \tag{2.6}$$

where the *pseudo-rapidity* $\eta \equiv -\ln[\tan(\theta/2)]$ is only function of the momenta. As the event-by-event longitudinal position of the actual interaction is distributed around the nominal interaction point with 30 cm r.m.s. width, it is useful to distinguish *detector pseudo-rapidity*, η_{det}, measured with respect to the $(0,0,0)$ nominal interaction point, from *particle pseudo-rapidity*, η, which is measured with respect to the z_0 position of the real vertex where the particle originated.[9]

Mapping the solid angle in terms of (pseudo)-rapidity and azimuthal angle is also convenient because the density of final-state particles in energetic hadronic collisions is approximately flat in the (Y, φ) space. Other convenient variables are the transverse component of the momentum with respect to the beam axis (p_{T}), the "transverse energy" (E_{T}), and the approximately Lorentz-invariant angular distance ΔR, defined as

$$\vec{p}_{\text{T}} \equiv (p_x, p_y) \rightarrow p_{\text{T}} \equiv p\sin(\theta), \quad E_{\text{T}} \equiv E\sin(\theta), \quad \text{and} \quad \Delta R \equiv \sqrt{\eta^2 + \phi^2}. \tag{2.7}$$

Throughout this thesis, the magnitude of the vector $\vec{p}_{\text{T}}$ (and of any vector $\vec{v}$) is indicated as

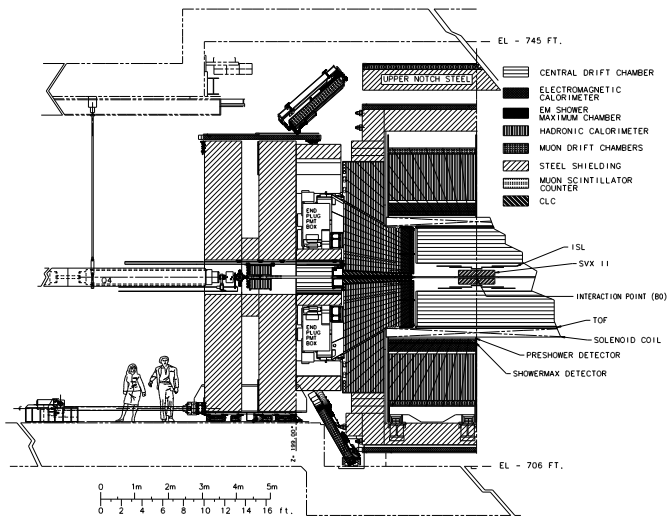

Figure 11: Elevation view of one half of the CDFII detector.

p_{T} (v) , instead of $|\vec{p}_{\text{T}}|$ $(|\vec{v}|)$, for a simpler notation.

9 An idea of the difference is given by considering that $\eta_{\text{det}} \approx \eta \pm 0.2$ if the particle was produced at $z = 60$ cm from the nominal interaction point.

2.2.2 Overview

CDFII (see fig. 11) is a 5000 t assembly of sub-detectors, $\approx$ 16 m in length by $\approx$ 12 m in diameter, which can be moved from its garaged position, in the CDF assembly building, to its operation position on the Tevatron beam line. The 31.4 m move takes one day. The CDFII detector was designed and constructed with an approximately cylindrically symmetric layout both in the azimuthal plane and in the "forward" ($z > 0$, east) "backward" ($z < 0$, west) directions with spatial segmentation of its sub-components roughly uniform in pseudo-rapidity and azimuth. CDFII is composed of several specialized subsystems, each one designed to perform a different task, arranged in a standard layout for multipurpose detectors; starting from the interaction point, particles emitted within the acceptance region encounter in sequence: a thin wall beryllium vacuum pipe, a high-precision tracking system composed by an inner silicon system and an outer drift-chamber, a time-of-flight detector, a solenoidal magnet and its return steel yoke, finely segmented sampling calorimeters, and muon detectors.

Its main features are an excellent tracking performance, which provides high mass resolution and precisely reconstructed positions of decay-vertices, good electron and muon identification capabilities combined with charged-hadron identification, and an advanced trigger system that fully exploits the high event-rates. A detailed description of the CDFII detector can be found in ref. [21] and in references therein.

2.3 THE TRACKING SYSTEM

Three-dimensional charged particle tracking is achieved through an integrated system consisting of three silicon inner sub-detectors and a large outer drift-chamber, all contained in a superconducting solenoid (see fig. 12). The 1.41 T magnetic field and the 130 cm total lever arm provide excellent tracking performances.

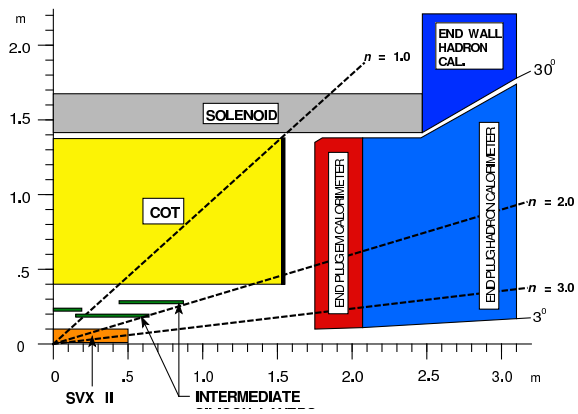

Figure 12: Elevation view of one quadrant of the inner portion of the CDFII detector showing the tracking volume surrounded by the solenoid and the forward calorimeters.

In the central region ($|\eta_{\text{det}}| \lesssim 1$), 7 silicon samplings (one in the (r, φ) view plus six in the (r, φ, z) view), and 96 chamber samplings (48 (r, φ) plus 48 (r, z)) are available between 1.6 and 132 cm. In the forward and backward regions ($1 \lesssim |\eta_{\text{det}}| \lesssim 2$), 8 silicon samplings (one in the (r, ϕ) view plus seven in the (r, ϕ, z) view) are available between 1.6 and 29 cm, along with partial information from the chamber.

The high number of samplings over the 88 cm lever arm of the chamber ensure precise determination of curvature, azimuth, and pseudo-rapidity of the tracks in the central region. The chamber provides also track seeds for pattern-recognition in silicon.

The core of the silicon detector is the Silicon VerteX (SVXII) detector. It provides five three-dimensional measurements that extend the lever arm by 41.5 cm toward the beam thus allowing more precise determination of the trajectories and identification of decay-vertices displaced from the beam-line. The SVXII has an outer and an inner extension. The outer extension, *i. e.*, the Intermediate Silicon Layers (ISL), provides a single (double) three-dimensional silicon measurement in the central (forward-backward) region, at intermediate radial distance from the chamber. The ISL allows efficient linking between tracks reconstructed in the chamber and hits detected in the SVXII, and extends the track finding at pseudo-rapidities $1 \lesssim |\eta_{\rm det}| \lesssim 2$, where the chamber coverage is partial. The inner extension, the Layer 00 (L00), is a light-weight silicon layer placed on the beam-pipe. It recovers the degradation in resolution of the reconstructed vertex position due to multiple scattering on the SVXII read-out electronics and cooling system, installed within the tracking volume. The integrated design of the tracking system allowed commonality of components among sub-detectors (read-out chip, support structures, etc.) thus simplifying construction and operation.

All 722 432 channels from the $\approx 7.0\,\mathrm{m}^2$ silicon active-surface employ 5644 radiation-tolerant, custom integrated read-out chips of the same type. This chip allows independent cycles of digitization of data and analog processing of subsequent data. The discriminated differential pulse from each channel is preamplified, digitized and propagated to the downstream data-acquisition. The ISL and the SVXII, whose mass is approximately 128 kg, share the carbon-fiber supporting structure.

The total amount of material in the silicon system, averaged over φ and z, varies roughly as $0.1X_0/\sin(\theta)$ in the $|\eta_{\rm det}| \lesssim 1$ region, and roughly doubles in $1 \lesssim |\eta_{\rm det}| \lesssim 2$ because of the presence of cables, cooling bulk-heads, and portions of the support frame.[10] The average amount of energy loss for a charged particle is roughly 9 MeV. The total heat load of the silicon system is approximately 4 kW. To prevent thermal expansion, relative detector motion, increased leakage-current, and chip failure due to thermal heating, the silicon detectors and the associated front-end electronics are held at roughly constant temperature ranging from $-6\,^\circ\mathrm{C}$ to $-10\,^\circ\mathrm{C}$ for L00 and SVXII, and around $10\,^\circ\mathrm{C}$ for ISL, by an under-pressurized water and ethylene-glycol coolant flowing in aluminum pipes integrated in the supporting structures.

2.3.1 The magnet

A 1.4116 T solenoidal magnetic field is maintained in the region $r \lesssim 150\,\mathrm{cm}$ $|z| \lesssim 250\,\mathrm{cm}$ by circulating a 4650 A current (current density $1150\,\mathrm{A\,m^{-1}}$) through 1164 turns of an aluminum-stabilized NbTi/Cu super-conducting coil. The field is oriented along the positive $\hat{z}$ (proton) direction and is uniform to within 0.1% in the $|z| \lesssim 150\,\mathrm{cm}$ volume, where tracking measurements are made (see fig. 12). The tiny non-uniformities, mapped out during detector construction, are treated as small perturbations in the track-fitting algorithms. During data-taking, the field is continuously monitored by nuclear magnetic resonance probes with 0.01% accuracy. Any deviation from the mapped values is applied as a correction to the measured track parameters. The threshold to radially escape the magnetic field for a charged particle is $p_{\rm T} \gtrsim 0.3\,\mathrm{GeV}/c$ while the trajectory of a charged particle with $p_{\rm T} = 30\,\mathrm{GeV}/c$ deviates only 1.6 cm from a straight path of 150 cm. The solenoid is 4.8 m in length, 1.5 m in radius, $0.85X_0$ in radial thickness (for normally incident particles.), and is cooled by forced flow of two-phase helium. Outside the coil, the return of the field flux is a box-shaped steel yoke, 9.4 m high by 7.6 m wide by 7.3 m long. It avoids

10 The symbol X_0 indicates the radiation length.

interference between the field and the proper operations of the photo-multiplier tubes (PMT) used in the calorimeters.

2.3.2 Layer 00

The L00 is the innermost layer of the silicon detector [22]. It consist of a single, castellated layer of single-sided, AC-coupled silicon sensors mounted directly on the beam pipe at radii, alternating in φ, of 1.35 or 1.62 cm from the beam. It provides full azimuthal and $|z| \lesssim 47$ cm longitudinal coverage. Longitudinally adjacent sensors (0.84 (or 1.46) cm $\times$ 7.84 cm) are ganged in modules of 15.7 cm active-length arranged into twelve partially-overlapping φ sectors, and six longitudinal barrels. These radiation-tolerant sensors are biased to $\mathcal{O}(500)$V, which allows full depletion after $\mathcal{O}(5)$Mrad integrated radiation doses. The strips are parallel to the beam axis allowing sampling of tracks in the (r, φ) plane. The inter-strip implant pitch of 25 µm with floating alternate strips results in 50 µm read-out pitch. The analog signals of the 13 824 channels are fed via fine-pitch cables, up ≈ 50 cm long, to the front-end electronics outside the tracking volume.

2.3.3 Silicon VerteX detector II

The SVXII is a fine resolution silicon micro-strip vertex detector that provides five three-dimensional samplings of tracks at 2.45 (3.0), 4.1 (4.6), 6.5 (7.0), 8.2 (8.7), and 10.1 (10.6) cm of radial distance from the beam with full pseudo-rapidity coverage in the $|\eta_{\text{det}}| \lesssim 2$ region (see fig. 12 and fig. 13(a)) [23]. This corresponds to a length of $|z| \lesssim 96$ cm along the beam-line, sufficient to cover the $\sigma_z \approx 28$ cm longitudinal spread of the luminous region. The SVXII has a cylindrical geometry coaxial with the beam, and its mechanical layout is segmented in three 32 cm axial sections ("barrels") times twelve 30° azimuthal sectors ("wedges") times five equally-spaced radial layers. A small overlap between the edges of adjacent azimuthal sectors helps wedge-to-wedge alignment (see fig. 13(b)).

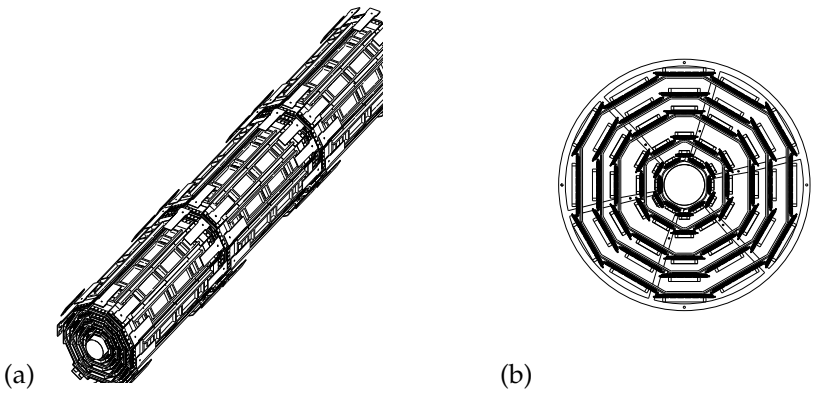

Figure 13: Schematic illustration of the three instrumented mechanical barrels of SVXII (a) and of the cross-section of a SVXII barrel in the (r, φ) plane (b).

Sensors in a single layer are arranged into independent longitudinal read-out units, called "ladders". Each ladder comprises two, double-sided sensors and a multi-layer electronic board, all glued on a carbon-fiber support. Front-end electronics, biasing circuits, and fan-out are located on the board that serves the pair of sensors whose strips are wire-bonded together resulting in a 15 cm active length. At a given radial layer and azimuth, each barrel contains pairs of ladders stacked length-wise head-to-head to keep the read-out electronic

at the two outside extremities of the barrel (see fig. 13(a)). The active surface consists of double-sided, AC-coupled, 7.5 cm $\times$ 1.5–5.8 cm silicon sensors with micro-strips implanted on a 300 µm thick, high resistivity bulk. Bias is applied through integrated poly-silicon resistors. On one side, all sensors have axial strips (*i. e.*, parallel to the beam direction) spaced by approximately 60–65 µm, for a precise reconstruction of the φ coordinate. On the reverse side, the following combination of read-out pitch (strip orientations with respect to the beam) is used: 141 µm (90°), 125.5 µm (90°), 60 µm (−1.2°), 141 µm (90°), 65 µm (1.2°), from the innermost to the outermost layer for reconstructing the z coordinate. A total of 405 504 electronics channels are used for SVXII.

2.3.4 Intermediate Silicon Layers

The ISL is a silicon tracker placed at intermediate radial distance between the SVXII and the drift chamber (see fig. 12), and covering the $|\eta_{\text{det}}| \lesssim 2$ pseudo-rapidity range for a total length of 174 cm along z [24]. At $|\eta_{\text{det}}| \lesssim 1$ a single layer of silicon sensors is mounted on a cylindrical barrel at radius of 22.6 (or 23.1 cm). At $1 \lesssim |\eta_{\text{det}}| \lesssim 2$ two layers of silicon sensors are arranged into two pairs of concentric barrels (inner and outer). In the inner (outer) barrel, staggered ladders alternate at radii of 19.7 and 20.2 cm (28.6 and 29.0 cm). One pair of barrels is installed in the forward region, the other one in the backward region. Each barrel is azimuthally divided into a 30° structure matching the SVXII segmentation. The basic read-out unit consists of an electronic board and three sensors ganged together resulting in a total active length of 25 cm. ISL employs 888 5.7 cm $\times$ 7.5 (6.7) cm double-sided, AC-coupled, 300 µm-thick sensors. Each sensor has axial strips spaced by 112 µm on one side, and 1.2°-angled strips spaced 112–146 µm on the reverse, for 303 104 total channels.

2.3.5 Central Outer Tracker

A multi-wire, open-cell drift chamber provides charged particle tracking at large radii in the central pseudo-rapidity region ($|\eta_{\text{det}}| \lesssim 1$, see fig. 12) [25]. The Central Outer Tracker (COT) has an hollow-cylindrical geometry, its active volume spans from 43.4 to 132.3 cm in radius and $|z| \lesssim 155$ cm in the axial direction. Arranged radially into eight "super-layers", it contains 96 planes of wires that run the length of the chamber between two end-plates (see fig. 14(a)). Each super-layer is divided into φ cells; within a cell, the trajectory of a charged particle is sampled at 12 radii (spaced 0.583 cm apart) where sense wires (anodes) are strung. Four super-layers employ sense-wires parallel to the beam axis, for the measurement of the hit coordinates in the (r, φ) plane. These are radially interleaved with four stereo super-layers whose wires are alternately canted at angles of +2° and −2° with respect to the beam-line. Combined read-out of stereo and axial super-layers allows the measurement of the (r, z) hit coordinates. Each super-layer is azimuthally segmented into open drift-cells. The drift cell layout (see fig. 14(b)) consists of a wire plane closed azimuthally by cathode sheets spaced approximately 2 cm apart. The wire plane contains sense wires alternating with field-shaping wires, which control the gain on the sense wires optimizing the electric field intensity. The cathode is a 6.35 µm-thick Mylar sheet with vapor-deposited gold shared with the neighboring cell.[11] Innermost and outermost radial extremities of a cell (*i. e.*, the boundaries between super-layers) are closed both mechanically and electrostatically by Mylar strips with an additional field-shaping wire attached, the shaper wire.

Both the field sheet and wire plane have a center ($z \approx 0.0$ cm) support rod that limits motion due to electrostatic forces. Each wire plane contains 12 sense, 13 field-shaping, and 4 shaper wires, all made of 40 µm-diameter gold-plated tungsten. Wire planes are

11 Gold, used also for the wires, was chosen because of its good conductivity, high work function, resistance to etching by positive ions, and low chemical reactivity.

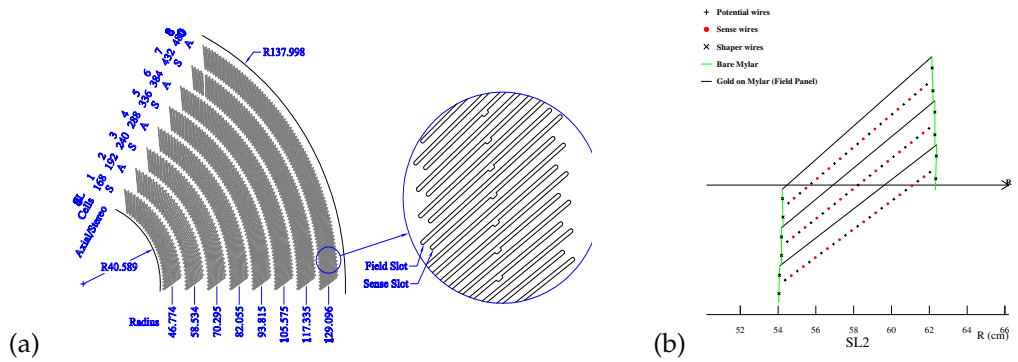

Figure 14: A 1/6 section of the COT end-plate (a). For each super-layer the total number of cells, the wire orientation (axial or stereo), and the average radius [cm] are given. The enlargement shows in detail the slot were wire planes (sense) and field sheet (field) are installed. Sketch of an axial cross-section of three cells in super-layer 2, (b). The arrow shows the radial direction.

not aligned with the chamber radius: a $\zeta = 35°$ azimuthal tilt (see fig. 14(b)) partially compensates for the Lorentz angle of the drifting electrons in the magnetic field.[12] The tilted-cell geometry helps in the drift-velocity calibration, since every high-p_T (radial) track samples the full range of drift distances within each super-layer. Further benefit of the tilt is that the left-right ambiguity is resolved for particles coming from the z-axis since the ghost track in each super-layer appears azimuthally rotated by $\arctan[2\tan(\zeta)] \approx 54°$, simplifying the pattern recognition problem.

A 50 : 50 gas admixture of argon and ethane bubbled through isopropyl alcohol (1.7%) flows at $9.45\,\mathrm{L\,min^{-1}}$ in the active volume of the chamber with its pressure being continuously monitored by four probes. Since 2003, the flux has been increased by a factor of ten to contrast the adverse effect of wire aging. High voltage is applied to the sense and field-shaping wires to generate a $1.9\,\mathrm{kV\,cm^{-1}}$ drift electric-field. This value, combined with the drift gas, results in a maximum drift-time of about 177 ns along a maximum drift-distance of 0.88 cm, allowing for read-out and processing of the COT data between two consecutive bunch-crossings. The average $180\,\mathrm{kV\,cm^{-1}}$ field present at the surface of the sense wire produces typical gains of 2×10^4. The 30 240 sense wires are read-out by the front-end chip, which provides input protection, amplification, shaping, baseline restoration, discrimination, and charge measurement. The input-charge information is encoded (logarithmically) in the signal width for dE/dx sampling, and is fed to a time-to-digital converter that records leading and trailing-edge times of signal in 1 ns bins. Hit times are later processed by the pattern recognition software to reconstruct trajectories. The material of the COT corresponds to an average $0.017 X_0$ for tracks at normal incidence.

2.3.6 Tracking performance

Within an uniform axial magnetic field in vacuum, the trajectory of a charged particle produced with non-zero initial velocity in the bending plane of the magnet is described by

12 In the presence of crossed electric ($\vec{E}$) and magnetic ($\vec{B}$) fields, electrons drifting in a gas move at an angle ζ with respect to the electric field direction, given by $\zeta \approx \arctan\left(v(E, B = 0)B/kE\right)$, where $v(E, B = 0)$ is the drift velocity without a magnetic field, and k is a $\mathcal{O}(1)$ empirical parameter that depends on the gas and on the electric field. A common solution for this problem consists in using tilted cells (*i. e.*, tilted drift electric field) that compensate the Lorentz angle linearizing the time-to-distance relation.

an helix. The arc of an helix described by a particle of charge q in the magnetic volume of CDF is parameterized using three transverse, and two longitudinal parameters:

$\boldsymbol{c}$ – signed helix (half)-curvature, defined as $C \equiv \frac{q}{2R}$, where R is the radius of the helix. This is directly related to the transverse momentum: $p_{\mathrm{T}} = \frac{cB}{2|C|}$;

$\boldsymbol{\varphi_0}$ – φ direction of the particle at the point of closest approach to the z-axis;

$\boldsymbol{d_0}$ – signed impact parameter, *i. e.*, the distance of closest approach to the z-axis, defined as $d_0 \equiv q(\sqrt{x_c^2 + y_c^2} - R)$, where (x_c, y_c) are the coordinates of the center-guide;

$\boldsymbol{\lambda}$ – the helix pitch, *i. e.*, $\cot(\theta)$, where θ is the polar direction of the particle at the point of its closest approach to the z-axis. This is directly related to the longitudinal component of the momentum: $p_z = p_{\mathrm{T}} \cot(\theta)$;

$\boldsymbol{z_0}$ – the z coordinate of the point of closest approach to the z-axis.

The trajectory of a charged particle satisfies the following equations [26]:

$$x = r\sin(\varphi) - (r + d_0)\sin(\varphi_0) \tag{2.8a}$$
$$y = -r\cos(\varphi) + (r + d_0)\cos(\varphi_0) \tag{2.8b}$$
$$z = z_0 + s\lambda, \tag{2.8c}$$

where s is the projected length along the track, $r = 1/2C$, and $\varphi = 2Cs + \varphi_0$. The reconstruction of a charged-particle trajectory consists in determining the above parameters through an helical fit of a set of spatial measurements ("hits") reconstructed in the tracking detectors by clustering and pattern-recognition algorithms. The helical fit takes into account field non-uniformities and scattering in the detector material. A concise overview of the tracking algorithms is given in the following, see [27, 28] for more details.

Tracking in the COT

The COT efficiency for tracks is typically 99%. The single-hit resolution is 140 µm, including a 75 µm contribution from the $\approx$ 0.5 ns spread in the measurement of the time of the interaction. Internal alignments of the COT cells are maintained within 10 µm using cosmic rays. Curvatures effects from gravitational and electrostatic sagging are under control within 0.5% by equalizing the difference of E/p between electrons and positrons as a function of $\cot(\theta)$. The typical resolutions on track parameters are the following: $\sigma_{p_{\mathrm{T}}}/p_{\mathrm{T}}^2 \approx 0.0015\,(\mathrm{GeV}/c)^{-1}$, $\sigma_{\varphi_0} \approx 0.035°$, $\sigma_{d_0} \approx 250\,\mu\mathrm{m}$, $\sigma_\theta \approx 0.17°$, and $\sigma_{z_0} \approx 0.3\,\mathrm{cm}$ for tracks fit with no silicon information or beam constraint.

Tracking in the silicon detector

The signal-to-noise ratio ranges from 14 : 1 for the (r, φ) layers of the SVXII to 10 : 1 for the L00. The best (r, φ) position resolution achieved is 9 µm, using two-strip clusters in SVXII. The z_0 resolution is typically 70 µm. An active real-time optical survey keeps the SVXII axis parallel to the beam within 20 µm along the SVXII length. Tight assembling tolerances (10 µm in φ and 40 µm in r) combined with a set of off-line algorithms provide internal and global L00, SVXII, and ISL alignment accurate within 20 µm, and constantly monitored in time. The excellent overall accuracy of the silicon alignment is confirmed by the fluctuations of the measured impact parameters of prompt particles as a function of z and φ, which do not exceed 2 µm. This can be compared with a typical impact parameter resolution of a few tenths of microns. The average offline tracking efficiency is 94%. In the $1 \lesssim |\eta| \lesssim 2$ region, where no COT coverage is present, seeding the silicon-only track with calorimeter information provides efficiencies over 70%, with minimal fake rates.

The silicon information improves the impact parameter resolution of tracks which, depending on the number (and radial distance) of the silicon hits, may reach $\sigma_{d_0} \approx 20\,\mu\text{m}$. This value, combined with the $\sigma_{\text{T}} \approx 30\,\mu\text{m}$ transverse beam size, is sufficiently small with respect to the typical transverse decay-lengths of heavy flavors (a few hundred microns) to allow separation of their decay-vertices from production vertices. The silicon tracker improves also the stereo resolutions up to $\sigma_\theta \approx 0.06°$, and $\sigma_{z_0} \approx 70\,\mu\text{m}$, while the transverse momentum and the azimuthal resolutions remain approximately the same of COT-only tracks.

2.3.7 Muon detectors

CDFII is equipped with scintillating counters and drift tubes [29, 30] installed at various radial distances from the beam to detect muons and shielded by the iron structure of the inner detector. Scintillators serve as trigger and vetoes while the drift chambers measure the φ coordinate using the absolute difference of drift electrons arrival time between two cells, and the z coordinate by charge division. These systems cover the whole range of pseudorapidity $|\eta_{\text{det}}| < 2$ and are used only to identify the penetrating muon reconstructing a small segment of their path (stub) sampled by the chambers. The momentum measurement is performed by pointing back the stub to the corresponding track in the COT. The shield is constituted by the iron of the calorimeter, the return yoke and further steel walls intended to filter out the punch-through of hadrons. It also means that low energy muons, with p_{T} less than $\simeq 1.5\,\text{GeV}/c$, are absorbed in the inner detector and do not reach the muon chambers. Finally, the additional shielding results in multiple Coulomb scattering, which deflects the muon trajectory and must be taken into account in track-to-stub matching.

There are four muon chambers in use at CDFII: the Central MUon detector (CMU), Central Muon uPgrade (CMP), Central Muon eXtension (CMX), and Intermediate MUon detectors (IMU). The scintillators (CSP,CSX, and BSU) are placed near each drift tubes to measure and minimize backgrounds coming from out-of-time interactions in the beampipe.

The CMU is positioned around the Central HAdronic (CHA) at $r = 347\,\text{cm}$, and provides coverage in the $\eta_{\text{det}} < 0.6$ region. It is made of 144 φ segments, or modules. Each module has four layers of four rectangular drift cells divided into East and West portions, with each cell containing a 50 ¯m stainless steel wire at the center, in the same argon-ethane-alcohol mix as in the COT. The sense-wires for the first and third (and second and fourth) radial layer are ganged together in readout. Each wire pair is instrumented with a TDC to measure the muon's φ location and an ADC to measure the muon's z location. The maximum drift time in the CMU is $\simeq 800\,\text{ns}$. The minimum muon p_{T} required to reach the CMU is $\simeq 1.4\,\text{GeV}\,c^{-1}$. The hit position resolution in the CMU is 250 ¯m in $r - \varphi$ and $\simeq 1.2\,\text{mm}$ in z.

The CMP provides the same $|\eta_{\text{det}}|$ coverage as the CMU, behind an additional 60 cm of steel, which helps to reduce misidentification rate by absorbing penetrating hadrons. The set of muons with stubs in both the CMU and CMP is of particularly high purity ($\simeq 95\%$). The CMP chambers are rectangular, single-wire drift tubes configured in four layers with alternate half-cell staggering. Signals are readout by a single TDC per wire. The maximum drift time in the CMP is $\simeq 1400\,\text{ns}$. The minimum muon p_{T} required to reach the CMP is $\simeq 2.2\,\text{GeV}\,c^{-1}$. Both CMU and CMP provide full φ coverage.

The CMX provides an extension in pseudorapidity coverage to $0.6 < |\eta_{\text{det}}| < 1.0$. Although no additional steel shielding precedes the CMX, additional absorbing material is present because of the longer path through the hadronic calorimeter, magnet yoke and original steel shielding at the larger angle of tracks that reach the CMX. The CMX has four layers of twelve drift tubes for each 15° φ section. The maximum drift time in the CMX tubes is $\simeq 1400\,\text{ns}$. In the analysis described in this chapter were used muons detected in the CMU, CMX and CMP detectors.

The IMU provides coverage for $1.0 < |\eta_{\text{det}}| < 1.5$. It consists of a barrel-shaped array of muon chambers (BMU), and two arrays of scintillators, one barrel-shaped mounted parallel to the beamline (BSU), and one ring-shaped mounted perpendicular to it (TSU). The BMU consists of a single-wire rectangular drift tubes mounted in four half-cell-staggered stacks, each covering 1.25° in φ. The maximum drift time in the IMU tubes is $\simeq 800$ ns. The BSU scintillators each cover 2.5° in φ and a range of 1.25 in η_{det} The TSU scintillators each cover 5° in φ.

	CMU	CMP/CSP	CMX/CSX	IMU
Pseudorapidity range	$\eta_{\text{det}} < 0.6$	$\eta_{\text{det}} < 0.6$	$0.6 < \eta_{\text{det}} < 1.0$	$1.0 < \eta_{\text{det}} < 1.0$
Azimuthal coverage (Âř)	360	360	360	360
Max. drift time (ns)	800	1400	1400	800
Number of channels	2304	1076/269	2208/324	1728
Pion interaction length	5.5	7.8	6.2	6.2-20
Min. μ p_{T} (GeV c^{-1})	1.4	2.2	1.4	1.4-2.0

Table 6: Design parameter of the muon detectors.

2.4 OTHER DETECTORS

We briefly outline the other CDFII subdetectors which are not used in this thesis.

2.4.1 Time of Flight detector

The Time Of Flight detector (TOF) is a cylindrical array made of 216 scintillating bars [31] and it is located between the external surface of the COT and the cryostat containing the superconducting solenoid. Bars are 280 cm long and oriented along the beam axis all around the inner cryostat surface at an average radial distance of 138 cm. Both longitudinal sides of the bars collect the light pulse into photomultiplier and measure accurately the timing of the two pulses. The time between the bunch crossing and the scintillation signal in these bars defines the β of the charged particle while the momentum is provided by the tracking system. Particle Identification (PID) information is available through the combination of TOF information and tracking measurements. The measured mean time resolution is now 110 ps. This guarantees a separation between charged pions and kaons with $p_{\text{T}} \lesssim 1.6\,\text{GeV}/c$ equivalent to 2σ, assuming Gaussian distributions. Unfortunately, in high luminosity conditions the occupancy of the single bars determines a degradation in efficiency, which is about 60% per track.

2.4.2 Calorimeters

Outside the solenoid, scintillator-based calorimeters covers the region $\eta_{\text{det}} \leq 3.6$, and are devoted to the measurement of the energy deposition of photons, electrons and hadrons using the shower sampling technique.

The basic structure consists of alternating layers of passive absorber and plastic scintillator. Neutral particles and charged particles with a transverse momentum greater than about 350 MeV/c are likely to escape the solenoid's magnetic field and penetrate into the CDFII calorimeters. These are finely segmented in solid angle around the nominal collision point, and coarsely segmented radially outward from the collision point (in-depth segmentation.) Angular segmentation is organized in projective towers. Each tower has a truncated-pyramidal architecture having the imaginary vertex pointing to the nominal interaction

point and the base is a rectangular cell in the $(\eta_{\text{det}}, \varphi)$ space. Radial segmentation of each tower instead consists of two compartments, the inner (closer to the beam) devoted to the measurement of the electromagnetic component of the shower, and the outer devoted to the measure of the hadronic fraction of energy. These two compartments are read independently through separated electronics channels.

A different fraction of energy release in the two compartments distinguishes photons and electrons from hadronic particles. CDFII calorimeters are divided in several independent subsystems presented in the following subsections.

Central region: CEM, CHA, WHA

The radial extension of the calorimeters in the central region is $1.73\,\text{m} < r < 3.5\,\text{m}$. The Central ElectroMagnetic Calorimeter (CEM) [32, 33] is constructed as four azimuthal arches (NE, NW, SE, SW) each of which subtends 180° and is divided into twelve 15° wedges. A wedge consists of 31 layers of 5 mm thick polystyrene scintillator interleaved with 30 aluminum-clad lead 3.2 mm thick sheets, divided along η_{det} into ten towers ($\delta\eta_{\text{det}} \approx 0.11$ per tower). To maintain a constant thickness in X_0, compensating the $\sin(\theta)$ variation between towers, some lead layers are replaced with increasing amounts of acrylic as a function of η_{det}. Light from each tower is collected by sheets of acrylic wavelength shifter at both azimuthal tower boundaries and guided to two phototubes per tower. The spatial resolution of the CEM is about 2 mm. The outer two towers in one wedge (known as chimney towers) are missing to allow solenoid access, for a resulting total number of 478 instrumented towers. At a radial depth of $5.9X_0$, which is approximately the depth corresponding to the peak of shower development, the CEntral Strip multi-wire proportional chambers (CES) measure the transverse shower shape with ≈1.5 cm segmentation. A further set of multi-wire proportional chambers, the Central Pre-Radiator (CPR) [34] is located in the gap between the outer surface of the solenoid and the CEM. It monitors photon conversions started before the first CEM layer. Phototube gains are calibrated once per store using an automated system of Xenon or LED light flashers.

The hadronic compartment is the combination of two sub-systems: the CHA and Wall HAdronic (WHA) [35] calorimeters. Analogously as in the CEM, in both systems four "C"-shaped arches contain 48 wedges. Each CHA wedge is segmented into 9 η_{det} towers matching in size and position the CEM towers. The WHA wedge instead consists of 6 towers of which three are matching CHA towers. Radially a CHA tower is constructed of 32 layers of 2.5 thick steel absorber alternating with 1.0 cm thick acrylic scintillator. The WHA towers structure is similar but there are only 15 layers of 5.1 cm thick absorber.

The total thickness of the electromagnetic section corresponds to approximately $19X_0$ ($1\lambda_{\text{int}}$, where λ_{int} is the pion nuclear absorption length in units of $\text{g}\,\text{cm}^{-2}$), for a relative energy resolution $\sigma_E/E = 13.5\%/\sqrt{E\sin(\theta)} \oplus 2\%$. The total thickness of the hadronic section corresponds to approximately $4.5\lambda_{\text{int}}$, for an energy resolution of $\sigma_E/E = 50\%/\sqrt{E\sin(\theta)} \oplus 3\%$ for the central, and $\sigma_E/E = 75\%/\sqrt{E\sin(\theta)} \oplus 4\%$ for the end-wall.

Forward region: PEM, PHA

The coverage of the $1.1 \leq |\eta_{\text{det}}| \leq 3.6$ region relies on the scintillating tile Plug calorimeter [36, 37, 38] which is composed of two identical devices, one installed in $\eta_{\text{det}} > 0$ region and the other in the $\eta_{\text{det}} < 0$ region. Each of these two halves has electromagnetic and hadronic compartments (see fig. 15(b)).

In each half, the absorber of the Plug ElectroMagnetic calorimeter (PEM) consists of 23 "doughnuts"- shaped lead plates, 2.77 m in outer diameter, which have a central hole where the beam pipe is located. Each plate is made out of 4.5 mm thick calcium-tin-lead sandwiched between two 0.5 mm thick stainless-steel sheets. Between the absorber plates are inserted the 4 mm thick scintillator tiles organized azimuthally in 15° triangularly-shaped

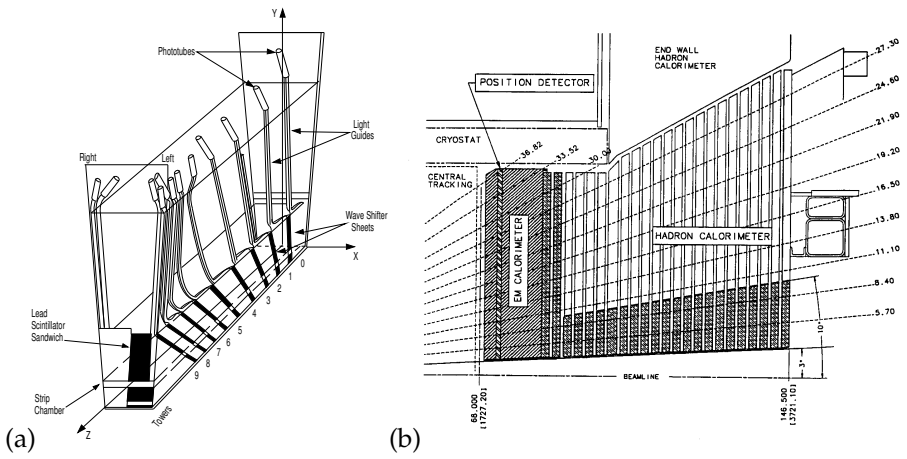

Figure 15: Schematic illustration of an azimuthal sector of the central electromagnetic calorimeter (a). Elevation view of one quarter of the plug calorimeter (b).

wedges. The signal of each tile is collected independently by embedded wavelength-shifter fibers which guide it to the photomultipliers. A preshower detector consist of a thicker (10 mm) amount of scintillator installed in the first layer of PEM, while shower maximum sampling is performed at radial depth of $\approx 6X_0$ by two tilted layers of scintillator strips (pitch 5 mm).

Each half of the hadronic compartment, Plug HAdronic calorimeter (PHA), is azimuthally subdivided in 12 wedge-shaped modules each subtending 30°. In depth each module consists of 23 layers of 5 cm thick iron absorber alternated with 6 mm scintillator layers. Within each sampling layer the scintillator is arranged in tiles similar to those used in the PEM.

The total thickness of the electromagnetic section corresponds to approximately $21X_0$ ($1\lambda_{\text{int}}$), for an energy resolution of $\sigma_E/E = 16\%/\sqrt{E\sin(\theta)} \oplus 1\%$. The total thickness of the hadronic section corresponds to approximately $7\lambda_{\text{int}}$, for an energy resolution of $\sigma_E/E = 74\%/\sqrt{E\sin(\theta)} \oplus 4\%$.

2.4.3 Cerenkov Luminosity Counters

The luminosity ($\mathscr{L}$) is inferred from the average number of inelastic interactions per bunch crossing ($\overline{N}$) according to $\overline{N} \times f_{\text{b.c.}} = \sigma_{\text{p}\bar{\text{p}}-\text{in.}} \times \varepsilon \times \mathscr{L}$, where the bunch-crossing frequency ($f_{\text{b.c.}}$) is precisely known from the Tevatron RF, $\sigma_{\text{p}\bar{\text{p}}-\text{in.}} = 59.3 \pm 2.3$ mb is the inelastic p$\bar{\text{p}}$ cross-section resulting from the averaged CDF and E811 luminosity-independent measurements at $\sqrt{s} = 1.8$ TeV [39] extrapolated to $\sqrt{s} = 1.96$ TeV, and ε is the efficiency for detecting an inelastic scattering.

The Cherenkov Luminosity Counters (CLC) are two separate modules, covering the $3.7 \lesssim |\eta_{\text{det}}| \lesssim 4.7$ range symmetrically in the forward and backward regions [40]. Each module consists of 48 thin, 110–180 cm long, conical, isobutane-filled Cerenkov counters. They are arranged around the beam-pipe in three concentric layers and point to the nominal interaction region. The base of each cone, 6–8 cm in diameter and located at the furthest extremity from the interaction region, contains a conical mirror that collects the light into a PMT, partially shielded from the solenoidal magnetic field. Isobutane guarantees high refraction index and good transparency for ultraviolet photons. With a Cerenkov angle $\theta_C = 3.4°$, the momentum thresholds for light emission are 9.3 MeV/c for electrons and 2.6 GeV/c for charged pions. Prompt charged particles from the p$\bar{\text{p}}$ interaction

are likely to traverse the full counter length, thus generating large signals and allowing discrimination from the smaller signals of angled particles due to the beam halo or to secondary interactions. In addition, the signal amplitude distribution shows distinct peaks for different particle multiplicities entering the counters. This allow a measurement of $\overline{N}$ with 4.4% relative uncertainty in the luminosity range $10^{31} \lesssim \mathscr{L} \lesssim 10^{33}\,\mathrm{cm}^{-2}\,\mathrm{s}^{-1}$. This accuracy, combined with the 4% relative uncertainty on the inelastic $p\bar{p}$ cross-section, results in an instantaneous luminosity measured with 5.9% relative uncertainty.

2.5 TRIGGER AND DATA ACQUISITION SYSTEM

From the rule of thumb 1 µb = 1 Hz at $\mathscr{L} = 10^{30}\,\mathrm{cm}^{-2}\,\mathrm{s}^{-1}$, we obtain that, at a typical Tevatron instantaneous luminosity $\mathscr{L} \approx 4 \times 10^{31}\,\mathrm{cm}^{-2}\,\mathrm{s}^{-1}$, and with an inelastic $p\bar{p}$ cross-section of $\sigma_{p\bar{p}-\mathrm{in.}} \approx 60\,\mathrm{mb}$, approximately 2.4×10^6 inelastic collisions per second occur, corresponding to one inelastic $p\bar{p}$ interaction per bunch crossing on average. Since the read-out of the entire detector needs about 2 ms on average, after the acquisition of one event, another approximately 5000 interactions would occur and remain unrecorded. The percentage of events rejected because the trigger is busy processing previous events is referred to as trigger *deadtime*.

On the other hand, the average size of the information associated to each event from the $\mathcal{O}(10^6)$ total CDFII channels is 300 kB. Even in case of deadtime-less read-out of the detector, in order to record all events, an approximate throughput and storage rate of $350\,\mathrm{GB\,s}^{-1}$ would be needed, largely beyond the possibilities of currently available technology.

Since the cross-sections of most interesting processes are 10^3–10^9 times smaller than the inelastic $p\bar{p}$ cross-section, the above problems may be overcome with an on-line preselection of the most interesting events. This is the task of the trigger system, which evaluates the partial information provided by the detector and discards the uninteresting events on-line.

The CDFII trigger is a three-level system that selectively reduces the acquisition rate, with virtually no deadtime, *i. e.*, keeping each event in the trigger memory a time sufficient to allow for a trigger decision without inhibiting acquisition of the following events (see fig. 16). Each level receives the accepted event from the previous one and, provided with detector information of increasing complexity and with more time for processing, applies a logical "OR" of several sets of programmable selection criteria to make its decision.

Prior to any trigger level, the bunched structure of the beams is exploited to reject cosmic-ray events by gating the front-end electronics of all sub-detectors in correspondence of the bunch crossing. The front-end electronics of each sub-detector, packaged in Versa Module Eurocard modules hosted in about 120 crates, has a 42-cells deep pipeline synchronized with the Tevatron clock-cycle (*i. e.*, 132 ns).

The Tevatron clock picks-up a timing marker from the synchrotron RF and forwards this bunch-crossing signal to the trigger and to the front-end electronics. Since the inter-bunch time is 396 ns, the pipeline collects data corresponding to a maximum of $42 \times 132/396 = 14$ bunch crossings, automatically rejecting 2/3 of cycles corresponding to the crossing of empty buckets. For each crossing, data enter the pipeline for read-out and eventual use at Level-2, and a Level-1 decision on a preceding crossing is made before the corresponding data reach the end of the pipeline. The Level-1 has $132\,\mathrm{ns} \times 42 \simeq 5.5\,\mu\mathrm{s}$ to make its decision before the contents of the buffer is deleted. On a Level-1 accept, the data from the Level-1 buffer are passed to the four-cell Level-2 buffer integrated in the front-end electronics of each sub-detector, and the event is queued for a Level-2 decision. While data in a Level-2 buffer are being processed, they cannot be overwritten by incoming data corresponding to a subsequent Level-1 accept. If a Level-1 accept occurs while all four Level-2 buffers are occupied, trigger deadtime occurs. The $5.5\,\mu\mathrm{s} \times 4 \simeq 20\,\mu\mathrm{s}$ latency of the Level-2 decision is less than approximately 80% of the average time between Level-1 accepts, to minimize

deadtime. On a Level-2 accept, the entire detector is read-out, thereby emptying a cell in all detector buffers for the next event; the event is queued for read-out in Level-3 and for eventual storage to permanent memory.

The following description emphasizes the aspects of the trigger specific to this analysis, the di-muon trigger, which is optimized to select events where low-p_T,opposite-charge di-muons consistent with charmonium decays are present

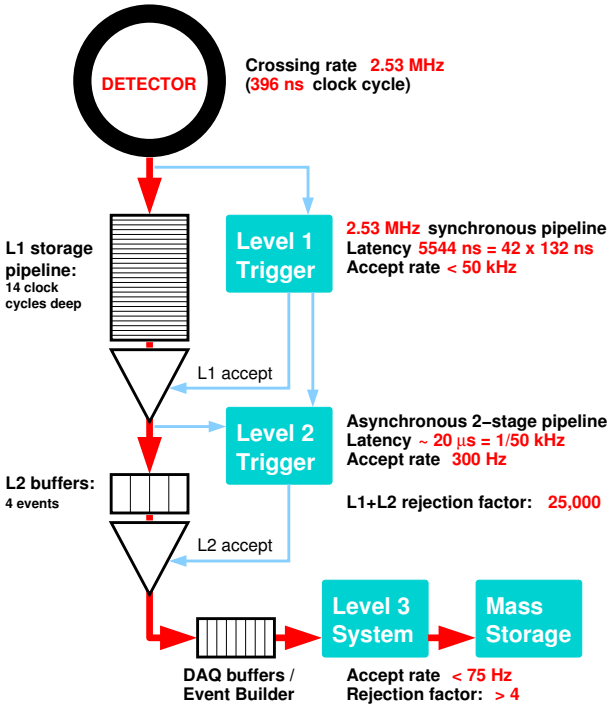

Figure 16: Functional block diagram of the CDFII trigger and data acquisition system.

The di-muon trigger relies on a clear signature of two muons coming from J/ψ(or $\psi(2S)$)$\rightarrow$ $\mu^+\mu^-$ decays. In order to make trigger decisions, it uses the drift chamber tracking and muon system information available at Level-1. Level-2 is used to tighten any existing requirements of Level-1, e.g. on the transverse momentum, and Level-3 uses more precise determination of several event variables, such as the transverse momentum of tracks, better track-stub matching, di-muon mass, etc. Although we refer to it as a single entity, the di-muon trigger is in fact a combination of two triggers: CMU-CMU, where both muons are found in the most central muon chamber, and CMU-CMX, where one muon is found in the CMU and one in the CMX. We describe the CMU-CMU trigger, and then comment on the differences in the CMU-CMX.

2.5.1 Level-1

At Level-1, a synchronous system of custom-designed hardware processes a simplified subset of data in three parallel streams to reconstruct coarse information from the calorimeters (total energy and presence of single towers over threshold), the COT (two-dimensional tracks in the transverse plane), and the muon system (muon stubs in the CMU, CMX, and CMP chambers). A decision stage combines the information from these low-resolution

physics objects, called "primitives", into more sophisticated objects, e. g. track primitives are matched with muon stubs, or tower primitives, to form muon, electron, or jet objects, which then undergo some basic selections.[13]

Drift chamber track-processor

The eXtremely Fast Tracker (XFT) is a custom processor that identifies two-dimensional tracks in the (r, φ) view of the COT (transverse plane) in time with the Level-1 decision. It uses pattern matching to first identify short segments of tracks and then to link them into full-length tracks [41]. After classifying the hits of the four axial COT super-layers in "prompt" (0–66 ns) or "delayed" hits (67–220 ns), depending upon the observed drift-time within the cell, track segments are reconstructed in each axial super-layer. A pattern-matching algorithm searches for coincidences between the observed combinations of hits in each super-layer — a minimum of 11 (out of 12) hits is required — and a set of predetermined patterns. If a coincidence between segments crossing four super-layers is found, two-dimensional XFT-tracks are reconstructed by linking the segments. The segments are compared with a set of about 2400 predetermined patterns corresponding to all tracks with $p_T \gtrsim 1.5\,\mathrm{GeV}/c$ originating from the beam line. The comparison proceeds in parallel in each of the 288 azimuthal 1.25°-sectors in which XFT logically divides the chamber. If no track is found using all four super-layers, then the best track found in the innermost three super-layers is output. The track-finding efficiency and the fake-rate with respect to the off-line tracks depend on the instantaneous luminosity, and were measured to be $\varepsilon \approx 96\%$, and 3%, respectively, for tracks with $p_T \gtrsim 1.5\,\mathrm{GeV}/c$ at $\mathscr{L} \simeq 10^{31}\,\mathrm{cm}^{-2}\,\mathrm{s}^{-1}$. The observed momentum resolution is $\sigma_{p_T}/p_T^2 \approx 0.017\,(\mathrm{GeV}/c)^{-1}$, and the azimuthal resolution is $\sigma_{\varphi_6} \approx 0.3°$, where φ_6 is the azimuthal angle of the track measured at the sixth COT super-layer, located at 106 cm radius from the beam line.

The eXTRaPolation unit (XTRP) is the system that receives track information from XFT and extrapolates the tracks to the calorimeters and muon systems to look for matches in energy deposition or muon stubs. Muons and di-muon primitives are derived from hits in the muon chambers or coincidences of hits with the scintillators. This provides information which can be used immediately at Level-1 for triggering decision.

The following terminology is specific to triggering on CMU muons. A *stack* is a set of four drift cells stacked on top of each other. The CMU has 288 stacks in each of the East and West sides of the detector. A *Level 1 stub* is a track segment in a stack such that cells 1 and 3 or cells 2 and 4 have hits separated by no more than 396 ns. A *tower* is a set of two neighboring stacks. A tower has *fired* when one or both stacks have a Level-1 stub, and is *empty* otherwise. A *muon tower* is a fired tower matched with an XFT track.

In order to keep the Level-1 decision time short enough to remain synchronous, only information about which towers have fired is used in triggering, rather than detailed hit positions and direction. The XFT reports the p_T and φ_6, as well as the charge of the track to the XTRP. The XTRP extrapolates this track to the CMU radius and creates a *footprint*, a 3σ window in φ (wide enough to account for multiple Coulomb scattering). If a tower is found within that footprint, it is a muon tower. The CMU-CMU trigger requires that at least two muon towers be found such that they are either on opposite sides of the detector or are separated by at least tow other towers.

The CMU-CMX trigger uses a similar algorithm. The changes to the decision algorithm arise from differences between the CMU and CMX detectors. In the CMU-CMX case, only XFT tracks with $p_T > 2.2\,\mathrm{GeV}\,c^{-1}$ are used to match to the CMX as the extra material that muons pass through to reach the CMX limits further the momentum requirements on the muon, and no azimuthal separation is required because the muons are by definition in different subdetector volumes.

13 A particle jet is a flow of observable secondary particles produced in a spatially collimated form, as a consequence of the hadronization of partons produced in the hard collision.

2.5.2 Level-2

At Level-2, an asynchronous system of custom-designed hardware processes the time-ordered events accepted by the Level-1. Additional information from the shower-maximum strip chambers in the central calorimeter and the axial hits in the SVXII is combined with Level-1 primitives to produce Level-2 primitives. A crude energy-clustering is done in the calorimeters by merging the energies in adjacent towers to the energy of a seed tower above threshold. Level-1 track primitives matched with consistent shower-maximum clusters provide refined electron candidates whose azimuthal position is known with 2° accuracy. Information from the (r, φ) sides of the SVXII is combined with Level-1 tracks primitives to form two-dimensional tracks with resolution similar to the off-line one. Finally, an array of programmable processors makes the trigger decision, while the Level-2 objects relative to the following event accepted at Level-1 are already being reconstructed.

2.5.3 Level-3

The digitized information relative to the Level-2-accepted event reaches Level-3 via optical fibers and it is fragmented across all sub-detectors. It is collected by a custom hardware switch that arranges it in the proper order and transfers it to commercial computers, running LINUX and organized in a modular and parallelized structure of 16 subsystems [42]. The ordered fragments are assembled in the *event record*, a block of data that univocally corresponds to a bunch crossing and is ready for the analysis of the Level-3 software. The event reconstruction benefits from full detector information and improved resolution with respect to the preceding trigger levels, including three-dimensional track reconstruction, tight matching between tracks and calorimeter or muon information, and calibration information. If an event satisfies the Level-3 requirements, the corresponding event record is transferred to mass storage at a maximum rate of $20\,\mathrm{MB\,s^{-1}}$. A fraction of the output is monitored in real time to search for detector malfunctions, to derive calibrations constants and to graphically display events. The Level-3 decision is made after the full reconstruction of the event is completed and the integrity of its data is checked, a process that takes a few milliseconds.

Trigger algorithms are among the few elements of the experimental apparatus which are continuously improved and optimized, as this process does not require performing expensive and time-consuming hardware upgrades to the detector. The di-muon trigger has undergone constant revision in order to carry out such optimization. While the core logic outlined above is more or less constant, other parameters been changed often to improve the trigger. Such parameters include requirements on the p_{T} of the XFT tracks, the difference in φ between the two muons $\Delta\varphi$, and their transverse mass M_T. In addition, some of the triggers are prescaled, which means that only one of N events is kept. This is done in order to deal with periods of high luminosity when triggering on every event that passes the nominal requirements would overwhelm the Data AcQuisition (DAQ) system. An improvement of static prescaling is dynamic prescaling, where the trigger automatically adjusts its prescale over the data taking period as luminosity decreases, in order to accept a larger and larger fraction of the fewer and fewer number of events that are passing through the DAQ as the luminosity drops.

2.6 OPERATIONS AND DATA QUALITY

The proper operation of the detector and the quality of the on-line data-taking is continuously ensured by "crews" of three collaborators plus one technician which alternate on duty with eight-hours shifts, plus several sub-detector experts available on request. The on-line

crew, in communication with the Tevatron crew, ensures smooth data-acquisition, monitors the crucial parameters of all sub-detectors, and intervenes in case of malfunctions. The average data-taking efficiency is 85%. The inefficiency is approximately equally shared in a 5% arising at the beginning of the store, when the detector is not powered while waiting for stable beam conditions, a 5% due to trigger deadtime, and a 5% due to unexpected detector or DAQ problems. When no beam is present, cosmic-rays runs are taken, or calibrations of the sub-detector are done. During the Tevatron shut-down periods, the crew coordinates and helps the work of experts that directly access the detector.

Each time that at least one of the trigger paths fires, an "event" is labeled with a progressive number. Events are grouped into runs, i. e. periods of continuous data-taking in constant configurations of trigger table, set of active sub-detectors and so forth.[14] Several parameters of the operations (e. g. beam-line position and slope, set of calibrations, etc.) are stored in the database on a run-averaged format.

All data manipulations occurring some time after the data are written to permanent memories are referred to as *off-line* processes, as opposed to the on-line operations that take place in real time, during the data-taking. The most important off-line operation is the processing with a centralized *production* analysis that generates collections of high-level physics objects suitable for analysis, such as tracks, vertices, muons, electrons, jets, etc. from low-level information such as hits in the tracking sub-detectors, muon stubs, fired calorimeter towers, etc. [43]. During the production, more precise information about the detector conditions (e. g. calibrations, beam-line positions, alignment constants, masks of malfunctioning detector-channels, etc.) and more sophisticated algorithms are used than those ones available at the Level-3 of the trigger. The added information increases the event size by typically 20% after production. The production may be repeated when improved detector information or reconstruction algorithms become available: this typically occurs once per year. The reprocessing uses large farms of commercial processors that reconstruct approximately 10^7 events per day employing approximately 2–5 s per event with 1 GHz CPU[15].

To ensure homogeneous data-taking conditions, each run undergoes a quality inspection. On-line shift operators, off-line production operators, and sub-detector experts certify in what fraction of data the running conditions for all relevant sub-detectors are compliant to physics-quality standards.

When detectable problems of the detector occur, the data-taking is quickly stopped, so very short runs are likely to contain corrupted data. Runs with fewer than 10^8 live Tevatron clock-cycles, or fewer than 10^4 (10^3) Level-1 (Level-2) accepts, or containing data corresponding to an integrated luminosity $\int \mathscr{L}\, dt < 1\,\mathrm{nb}^{-1}$ are excluded from physics analysis. On-line shift operators further exclude the runs in which temporary or test trigger tables were used.[16] Runs whose data underwent problems or software crashes during the production are excluded off-line.

Accurate integrated luminosity measurements are ensured in physics-quality data by requiring the CLC to be operative during the data-taking and by verifying that a set of luminosity and beam-monitor probe quantities are within the expected ranges. Shift operators ensure that Level-1 and Level-2 trigger operate correctly and that the rate of SVXII data corruption errors is smaller than 1%.[17] For analyses that use COT information, the minimum integrated luminosity required is $10\,\mathrm{nb}^{-1}$ and the fraction of noisy COT channels is required to be smaller than 1%.

14 The data acquisition might need to be interrupted and recovered for several motivations, including the need for enabling or disabling a sub-detector, the need for a change in the trigger table, a problem in the DAQ chain and so forth.

15 The event size, and the processing-time increase roughly linearly with the instantaneous luminosity.

16 It is sometimes necessary to test new configurations of the trigger selections in a real data-taking condition to monitor trigger rates, performance and so on.

17 The read-out of the silicon detector and the proper integration of the information in the on-line infrastructure is a complex operation which, occasionally, leads to a certain fraction of data to be improperly processed.

2.7 MONTE CARLO SIMULATION OF DETECTOR AND TRIGGER

Estimation of the fraction of events of a certain type that escape the detector acceptance, or detailed studies of the expected response of the detector to the passage of particles is a common need in many analyses. Usually, complex detector geometries and the numerous effects that need to be accounted for in predicting their response make it the analytical derivation of the relevant distributions impractical or impossible. Monte Carlo (MC) techniques are an useful and widely-used tool to solve this problem. We provide here a short overview of the standard CDFII simulation. Further details can be found in ref. [44].

In the standard CDFII simulation, the detector geometry and material are modelled using the version 3 of the GEANT package [45] tuned to test-beam and collision data. GEANT receives in input the positions, the four-momenta, and the identities of all particles produced by the simulated products that have long enough lifetimes to exit the beam pipe. It simulates their paths in the detector, modelling their interactions (*bremsstrahlung*, multiple scattering, nuclear interactions, photon conversions, etc.) and the consequent generation of signals on a single channel basis. Specific packages substitute GEANT for some sub-detectors: the calorimeter response is simulated with GFLASH, a faster parametric shower-simulator [46] tuned for single-particle response and shower-shape using test-beam data (8–230 GeV electrons and charged pions) and collision data (0.5–40 GeV c^{-1} single isolated tracks); the drift-time within the COT is simulated using the GARFIELD standard package [47] further tuned on data; the charge-deposition model in the silicon uses a parametric model, tuned on data, which accounts for restricted Landau distributions, capacitive charge-sharing between neighboring strips, and noise [48]. Furthermore, the actual trigger logic is simulated. The output of the simulated data mimics the structure of collision data, allowing their analysis with the same reconstruction programs used for collision data.

The detector and trigger configuration undergo variations during data-taking. Minor variations may occur between runs, while larger variations occur, for instance, after major hardware improvements, or Tevatron shut-down periods. For a more detailed simulation of the actual experimental conditions, the simulation has been interfaced with the on-line database that reports, on a run-by-run basis, all known changes in configuration (position and slope of the beam line, relative mis-alignments between sub-detectors, trigger-table used) and local or temporary inefficiencies in the silicon tracker (active coverage, noisy channels, etc.). This allows us to simulate the detailed configuration of any set of real runs and to use it, after proper luminosity reweighing, for modeling the realistic detector response in any given subset of data.

3 STRATEGY, DATASET AND RECONSTRUCTION

With this chapter begins the description of the data analysis and original contribution of the author. It describes the strategy, the physics objects and the samples of data and Monte Carlo used in this work.

3.1 STRATEGY

Two complementary approaches have been identified for the search of $Z^-(4430) \to \psi(2S)\pi^-$ in CDF data. They aim at exploiting in full the experimental opportunities provided by the hadron collisions environment in measurement of heavy flavor physics. On one hand we have tried to reproduce the B-factories analysis searching for the $Z^-(4430)$ as a $\psi(2S)\pi^-$ intermediate resonance in the B^0 decay to $\psi(2S)K^+\pi^-$ final states. We will refer to this as the "displaced" approach. On the other hand we searched inclusively for a $\psi(2S)\pi^-$ resonance at $4.4\,\mathrm{GeV}\,c^{-2}$ without any requirement for presence of a B-decay in the event, what we call a search for "prompt" production.

3.1.1 The "displaced" approach

At present the $Z^-(4430)$ resonance has been observed only as intermediate state in B-decays. Searching for $B^0 \to Z^-K^+ \to \psi(2S)K^+\pi^-$ provides a direct comparison with the results of Belle and BaBar and allow CDF to contribute with discriminant information to confirm the observation from Belle or the null result from BaBar. This approach has also experimental advantages in hadron collisions. Requiring a B hadron decay in the event provides powerful discriminating observables that exploit the B meson high mass and long lifetime to reduce background caused by light-flavor decays. Clearly it also poses different challenges with respect to the e^+e^- collisions. Presumably the main limitation being the possible presence of different and larger sources of backgrounds, some of which unknown, with respect to the B-factories, and the consequent reduction in statistics while attempting to reject them.

3.1.2 The "prompt" approach

The opportunity to search directly for a $\psi(2S)\pi^-$ resonance is unique to high energy hadron collider experiments like CDF and constitutes a supplementary experimental asset to investigate XYZ physics, with respect to B-Factory. The phase-space available for the production of a particle of about $4\,\mathrm{GeV}\,c^{-2}$ is large and, assuming one is capable to control the combinatorial background, the signal of such a resonance may be easily detected, if the production rate is reasonable. Note that this argument is supported by past experience on the $X(3872)$ analysis, published in 2004 by the CDF collaboration [8]. The $X(3872)$ was observed for the first time by Belle as an intermediate $J/\psi\pi^+\pi^-$ resonance in $B^- \to J/\psi\pi^+\pi^-K^-$ decays. CDF then provided the first confirmation of the existence of this state with an analysis that looked for $J/\psi\pi^+\pi^-$ resonances inclusively in $p\bar{p}$ data, finding production cross-sections of $\mathcal{O}(50)$nb.

We therefore chose to search for the $Z^-(4430)$, also exploring inclusively the $\psi(2S)\pi^-$-mass distribution without any requirement of a B decay in the event. We may benefit from a high production rate and, as reference mode, we can use the signal of the $B^- \to \psi(2S)K^-$ (reconstructed as $\psi(2S)\pi^-$), similarly to what was done with the $\psi(2S) \to J/\psi\pi^+\pi^-$ in 2004.

3.2 USEFUL VARIABLES AND PHYSICS OBJECTS

Before discussing the details of trigger and off-line selection, we define some relevant quantities used in the analysis, referred to the processes illustrated in fig. 17.

TRANSVERSE MOMENTUM ($\vec{p}_T$): the projection of the momentum vector onto the plane perpendicular to the proton beam direction, calculated in the laboratory frame.

TRACK: the trajectory of a charged particle with p_T greater than $0.4\,\mathrm{GeV}\,c^{-1}$, parameterized in the axial magnetic field as an helix that fits aligned clusters of hits in the active regions of the tracking system. The track must be associated to, at least, ten axial and ten stereo hits in at least two axial and two stereo superlayers of the drift chamber (COT), and to at least three axial hits in three different layers of the silicon detectors (Sec. 2.3). These requirements were optimized in past CDF measurements to provide tracks with high-precision position determination while keeping track-finding efficiency high. We will show later that more stringent track requirements are more appropriate for our analysis. Tracks are reconstructed using a Kalman-filtering algorithm that propagates both hit and detector alignment information into reconstructed track parameters and their uncertainties. Information on energy loss and multiple Coulomb scattering upstream of the drift chamber is properly accounted for in this propagation. The particle mass appropriate to the hypothesis at hand for each given track (μ,π,K,p) is used to account for multiple scattering and energy losses.

MUON: a track associated to a matching cluster of hits in the muon detectors. We consider two classes of muons: "loose muons", with hits in the inner set of chambers (CMU and CMX) and satisfying the conditions $|\eta| < 0.6$ and $p_T > 1.5\,\mathrm{GeV}\,c^{-1}$ (CMU), or $0.6 < |\eta| < 1.0$ and $p_T > 2.0\,\mathrm{GeV}\,c^{-1}$ (CMX), and "tight muons", with hits also in the outer chambers (CMP) and satisfying the condition $|\eta| < 0.6$ and $p_T > 3.0\,\mathrm{GeV}\,c^{-1}$.

PRIMARY VERTEX: the space-point of the reconstructed primary $p\bar{p}$ interaction. An event may contain multiple primary vertices due to multiple hard $p\bar{p}$ collisions occurring in the same bunch-crossing ("pile-up" event).

SECONDARY VERTEX: the space-point in which the decay of a long-lived particle occurs. Its displacement with respect to the primary vertex in the transverse plane is indicated by the vector

$$\vec{x}_v = (\vec{\beta}\gamma)_T ct = (\vec{p}_T/m)ct, \tag{3.1}$$

for a particle of mass m and momentum p that decays at a time t after its production. All quantities are in the laboratory frame. Multiple secondary vertices may be present in the same event. They can be due to the intersection of tracks from various sources, including the decay of other heavy-flavor particles produced in the event, the decay of additional heavy-flavors produced in a pile-up event, fake (i. e. due to accidental combinations of noise hits) or mis-measured (i. e. partially contaminated by noise hits) tracks.

TRANSVERSE DECAY-LENGTH (L_{xy}): the displacement of the secondary vertex with respect to the primary one, projected onto the transverse momentum vector of the decaying particle (all quantities in the laboratory frame):

$$L_{xy} = \frac{\vec{p}_{\mathrm{T}} \cdot \vec{x}_{\mathrm{v}}}{p_{\mathrm{T}}} \tag{3.2}$$

IMPACT PARAMETER (d_0): the component in the transverse plane of the distance of closest approach between a track and the primary vertex. This is a signed quantity defined as

$$d_0 = \frac{\hat{z} \cdot (\vec{p}_{\mathrm{T}} \times \vec{x}_{\mathrm{v}})}{p_{\mathrm{T}}}, \tag{3.3}$$

where all quantities are in the laboratory frame. The impact parameter is typically different from zero for decay products of long-lived particles, while it is comparable with the convolution of its resolution and the transverse size of the beam ($\approx 40\,\mu\mathrm{m}$) for particles produced in the proximity of the primary vertex (prompt background).

3.3 TRIGGER AND SAMPLES

The dataset analyzed in this work was recorded by the CDFII detector in the March 2001 to July 2009 period and corresponds to an integrated luminosity of $5.7\,\mathrm{fb}^{-1}$ approximately.

The events collected in the dataset are selected through a di-muon trigger (See sec. 2.5.1) that identify interesting events for analysis dealing with di-muon resonances, within the large rate of $p\bar{p}$ collisions. As a consequence, the first unavoidable set of requirements imposed on events for inclusion in the sample is enforced by the trigger system in real time. The JPSI trigger, the specific variant of di-muon trigger used for this selection, is a collection of trigger paths whose more important requirements are summarized in the following:

LEVEL 1
- two XFT tracks matched with two muon stubs
- each CMU (CMX) muon has $p_{\mathrm{T}}^{XFT} > 1.5(2.2)\ \mathrm{GeV}\,c^{-1}$
- $\Delta\Phi_6(CMU, CMU) < 135$ for some paths, no cuts in $\Delta\Phi_6(CMU, CMX)$

LEVEL 2 : all Level-1 triggers are accepted.

LEVEL 3
- two tracks with opposite charge
- $2.7 < M_{\mu\mu} < 4\,\mathrm{GeV}\,c^{-2}$

3.3.1 Monte Carlo samples

In this analysis, a simulation of B or $Z^-(4430)$ signals and decays and of the subsequent detector response is used for several purposes:

- modeling physics background;
- modeling the acceptance and the efficiency of the trigger and reconstruction process;
- determine the signal shape and mass resolution.

Using the framework detailed in sec. 2.7 we produced samples of the following decays.

Signal modes:

- $B^0 \to Z^-[\psi(2S)\pi^-]K^+$ (10^5 simulated events);

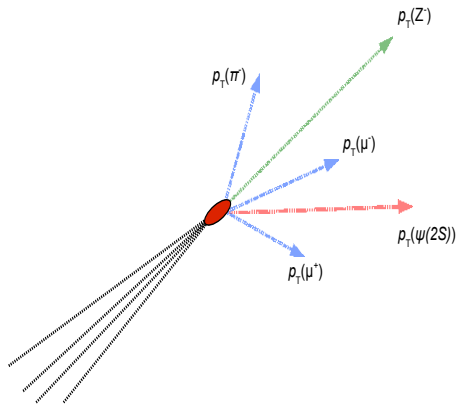

(a)

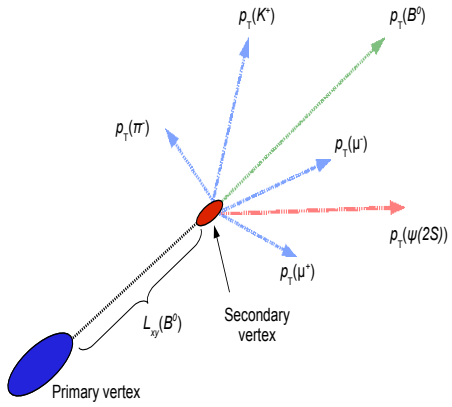

(b)

Figure 17: Illustrations of a $p\bar{p}$ event containing a $Z^- \to \psi(2S) + \pi^-$ (a), and a $B^0 \to \psi(2S)K^+\pi^- \to [\mu^+\mu^-]K^+\pi^-$ (b), both projected into the transverse plane. Ellipses indicate vertices, arrows indicate the transverse momenta (i. e. the direction) of particles. Not to scale.

- $Z^- \to \psi(2S)\pi^-$ (10^5 simulated events). For this mode we generated distinct samples assuming three choice of spin (0,1 and 2) and three different natural width (0, 50 and 100 MeV c^{-2}).

Modes used for acceptance/efficiency calculations.

- $B^+ \to \psi(2S)K^+$ (10^7 simulated events).

Background modes. These are all known b-hadron decays into final states containing a $\psi(2S)$ meson.

- $B^+ \to \psi(2S)K^*(892)^+$ (25×10^6 simulated events);
- $B^+ \to \psi(2S)K^+\pi^+\pi^-$ (25×10^6 simulated events);
- $B^0 \to \psi(2S)K^0$ (25×10^6 simulated events);
- $B^0 \to \psi(2S)K^+\pi^-$ (25×10^6 simulated events);
- $B^0 \to \psi(2S)K^*(892)^0$ (25×10^6 simulated events);
- $B_s^0 \to \psi(2S)\phi$ (25×10^6 simulated events).

The simulated $\psi(2S)$ are forced to decay in two muons while, for the other resonances ($K^*(892)$,K^0,ϕ) all the final state with significant branching ratio reported by the Particle Data Group (PDG) [4] are considered.

3.4 OFF-LINE RECONSTRUCTION

The events satisfying trigger requirements are fully stored as raw data. Offline reconstruction of physics objects follows to reduce the amount of information from the detector to a format and size convenient for the analysis, including information of detector alignments, calibration constants, etc...

In data we reconstructed two independent decay chains: $p\bar{p} \to Z^-[\to \psi(2S)\pi^-] + X$ and $p\bar{p} \to B^0 + X$ followed by B^0 decays to $\psi(2S)K^+\pi^-$. Two decays of the $\psi(2S)$ are considered: $\psi(2S) \to \mu^+\mu^-$ and $\psi(2S) \to J/\psi[\to \mu^+\mu^-]\pi^+\pi^-$.

The reconstruction is solely based on tracking and muon identification information. No attempt is made at event-by-event identification of hadrons, because of the limited particle identification capability of the detector. Also, not all the decay modes analyzed by the experiments at the B-Factories were considered. The $\psi(2S)$ and J/ψ decaying in electron-positron pairs are not included because of the strong degradation of momentum resolution, due to bremsstrahlung in the detector material, while the lower efficiency of K_S^0 reconstruction does not provide a major contribution to statistics from the $B^- \to \psi(2S)K_S^0\pi^-$ sample, at least in this first study.

3.4.1 $\psi(2S)$ candidates

The analysis begins by isolating a sample of well-measured di-muon candidates. The trigger requirements are confirmed offline by selecting events that contain two oppositely charged muon candidates, each with matching COT and muon chamber tracks. The tracks forming the di-muon object are required to satisfy a kinematic vertex fit and, if the di-muon invariant mass is within the $3.4 < M(\mu^+\mu^-) < 3.9\,\mathrm{GeV}\,c^{-2}$ range, the di-muon is considered a valid $\psi(2S)$ candidate. If the di-muon mass is in the $2.85 < M(\mu^+\mu^-) < 3.35\,\mathrm{GeV}\,c^{-2}$ range, the di-muon is considered a valid J/ψ candidate. In this case, the $\psi(2S)$ candidate is reconstructed by combining a pair of oppositely charged tracks with pion mass assignment with the J/ψ candidate. Those tracks are required not to be associated with muons. A kinematic fit is performed on this four-track vertex with the external constraint that the di-muon mass is equal to the known J/ψ mass [4] so that the mass resolution on the $\psi(2S)$ candidate improves.

3.4.2 The $p\bar{p} \to Z^-[\to \psi(2S)\pi^-] + X$ channel

Candidates are reconstructed, in the mass range $4.2 < M(\psi(2S)\pi^\pm) < 5.5\,\mathrm{GeV}\,c^{-2}$, adding a track, with pion mass assignment, to the $\psi(2S)$ vertex. The track is required not to be

associated with a muon. A mass constrained fit is performed on the three(five)-track vertex, using the known $\psi(2S)$ mass [4]. Candidates are required to have $p_{\mathrm{T}} > 3.0\,\mathrm{GeV}\,c^{-1}$.

3.4.3 The $B^0 \to Z^-[\to \psi(2S)\pi^-]K^+$ channel

The reconstruction of the neutral vertex ($V0$, the vertex of two tracks with kaon and pion mass assignment) uses all tracks not associated with muons of the $\psi(2S)$ candidates. Pairs of oppositely charged particles are combined to identify these neutral candidates. Both assignments, π^+K^- and $K^+\pi^-$, are considered. Selection for these neutral vertices is based upon the mass calculated for each track pair and for each assignment. The mass is required to be within the range $0 < M(K^\pm\pi^\pm) < 1.6\,\mathrm{GeV}\,c^{-2}$. This corresponds to the maximum energy available for the two hadrons in the frame of reference of the B^0 at rest ($M_{B^0} - M_{\psi(2S)}$).

B^0 candidates are reconstructed by combining the tracks of the $\psi(2S)$ and $V0$ candidates with additional requirements: muons (and the two tracks, in the $\psi(2S) \to J/\psi\pi^+\pi^-$ case) must satisfy a simultaneous $\psi(2S)$ mass and vertex constrained fit, the neutral vertex must satisfy a vertex constrained fit and all four(six) tracks (two muons and two(four) hadrons) must fit to a single vertex. Furthermore, the B^0 candidates have $p_{\mathrm{T}} > 5.95\,\mathrm{GeV}\,c^{-1}$ and invariant mass within the range $5.1 < M(\psi(2S)V0) < 5.5\,\mathrm{GeV}\,c^{-2}$.

The main structure of the reconstruction code was originally implemented for a previous analysis [49]. The author has modified and updated it for the purpose of this work. In particular, the code performing the reconstruction of the five-track vertex has been developed from scratch for this analysis and this original technical contribution is now part of the CDF standard code.

The next chapters describe in details the analysis of the two different channels.

4 THE "DISPLACED" CHANNEL

In the following is described the "displaced" $Z^-(4430)$ analysis, including the optimization of the offline selection, the inspection of the Dalitz plot and the comparison with B-Factories.

4.1 OPTIMIZATION OF THE $B^0 \to \psi(2S)K^+\pi^-$ SIGNAL

Using the reconstruction detailed in the previous chapter, and a baseline set of simple cuts (Tab. 7) from previous B-physics analyses, we obtain the $\psi(2S)K^+\pi^-$–mass distribution of fig. 18. A clear B^0 signal is shown overlapping a significant background. A fit of the mass distribution using a gaussian function for the signal and a parabola for the background yields $S = 2432 \pm 116$ signal events peaking at $m = 5279\,\mathrm{MeV}\,c^{-2}$ and spread with $\sigma = 7\,\mathrm{MeV}\,c^{-2}$. This is the starting point for our search in the "displaced" channel. In the search for rare processes like the production of exotic $Z^-(4430)$ hadrons, the statistics and the level of background of the final sample are key factors in determining one's analysis sensitivity. A customary approach to increase the sensitivity is to optimize of the analysis selection, that is devising an *unbiased* procedure meant to identify the set of selection requirements optimal for the purpose at hand. In our case, there are non-obvious assumptions one should make on the unknown features of the signal, e.g. its spin, width, etc..., which can makes it difficult an optimization specifically targeted at selecting $Z^-(4430)$ from B^0 decays. We therefore adopt a simplified approach in which we optimize the selection for another signal ($B^0 \to \psi(2S)K^+\pi^-$), using the (unjustified) assumption that optimizing the $B^0 \to \psi(2S)K^+\pi^-$ signal provides an optimization of the $Z^-(4430) \to \psi(2S)\pi^-$ decays that are possibly resonating in its final state. This procedure is certainly unbiased, although probably not optimal, but sufficient for a first study. In this part of the analysis we considered only the sample with $\psi(2S) \to \mu^+\mu^-$ decays.

4.1.1 Study of discriminating observables

We studied the distributions of a number of kinematic and vertex-fit related quantities to identify those more effective in separating the B^0 signal from background.

The selection (Tab. 7) is inclusive enough to act as a starting point for the optimization, but also to allow clear identification of signal and 'sidebands' (background) regions in the mass distribution to be used in the procedure. We defined as signal+background region the mass range within $3\sigma \approx 30\,\mathrm{MeV}\,c^{-2}$ from the known B^0 mass. Similarly, the background is sampled from candidates populating the range between 6 and 12 σ (where σ is the width of the B^0 peak) at higher masses of the known B^0 mass (See fig. 18, in red). We did not use the lower-mass sidebands because at masses lower than the B^0 there are also misreconstructed B-decays which have common features with our signal and are not expected to populate its mass region because of kinematic constraints. The region at higher mass should be a better model for combinatorial background, which is expected to be the dominant source of background under the signal peak. Assuming that candidates populating the high-mass sideband have similar features to background candidates under the signal peak, we compared signal (blue) to background (red) distributions (normalized to the same area) for the following quantities (figs. 19 and 20), after operating a sideband subtraction:

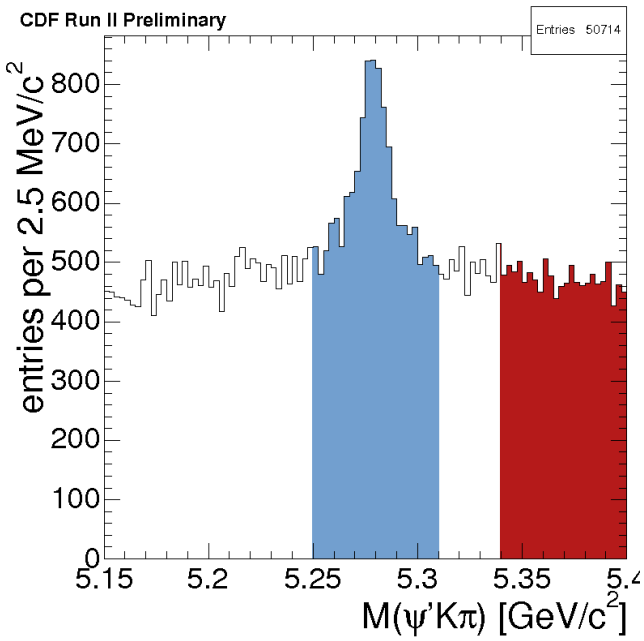

Figure 18: Invariant $\psi(2S)K^+\pi^-$-mass distribution of the events selected through the baseline cuts used as a starting point for the optimization with fit to a Gaussian and a parabola overlaid.

Quantity	Requirement
$m(\psi(2S))$	in [3.60609, 3.76609]
$ct(B^0)$	$> 100\,\mu\text{m}$
$p_T(\psi(2S))$	$> 3\,\text{GeV}\,c^{-1}$
$p_T(K)$	$> 0.9\,\text{GeV}\,c^{-1}$
$p_T(\pi)$	$> 0.4\,\text{GeV}\,c^{-1}$
$p_T(B^0)$	$> 6\,\text{GeV}\,c^{-1}$
$p_T(\mu)$	$> 1.5\,\text{GeV}\,c^{-1}$
$\lvert d_0(V_0 = K\pi)_{\psi(2S)}\rvert$	$< 0.01\,\text{cm}$
$Prob_{\chi^2}(B^0)$	> 0.0001
$Prob_{\chi^2}(\psi(2S))$	> 0.0001

Table 7: Baseline selection.

- transverse momentum of B^0, $\psi(2S)$ and muon candidates;
- decay length of the B^0 candidate;
- impact parameter significance (d_0/σ_{d_0}) for pion and kaon candidates, where σ_{d_0} is the uncertainty on the d_0 determination as returned from the track fit;
- impact parameter of muon and of the neutral vertex (with respect to the $\psi(2S)$ vertex) candidates;
- χ^2-probability of the fits to the B^0, $\psi(2S)$, and neutral vertices;
- mass of the $\psi(2S)$ candidate.

We expect these observables to carry most of the discriminating power since they are sensitive to the features of heavy, long-lived particles like the desired B^0 (transverse momenta, decay length and impact parameters) or they behave differently for combinatorial and physics candidates (χ^2-probabilities). Several distributions show differences between signal and background, which look promising toward an optimization. The ct distribution shows the expected exponential shape for long-lived B^0 candidates and the more steeply decreasing distribution of background. The impact parameters of kaon and pion candidates for signal are more significantly different from zero than their background counterparts, while less discrimination seems achievable by exploiting the impact parameters of the muons and of the neutral vertex. The transverse momenta of signal candidates show also some interesting discrimination, with backgrounds peaking at smaller values. The vertex-fit probabilities for signal candidates show longer tails toward high values, compared to background distributions that peak at zero. All this information is useful in an optimization, although many quantities are correlated so that the net discrimination available may be lower than the apparent contributions of the individual distributions.

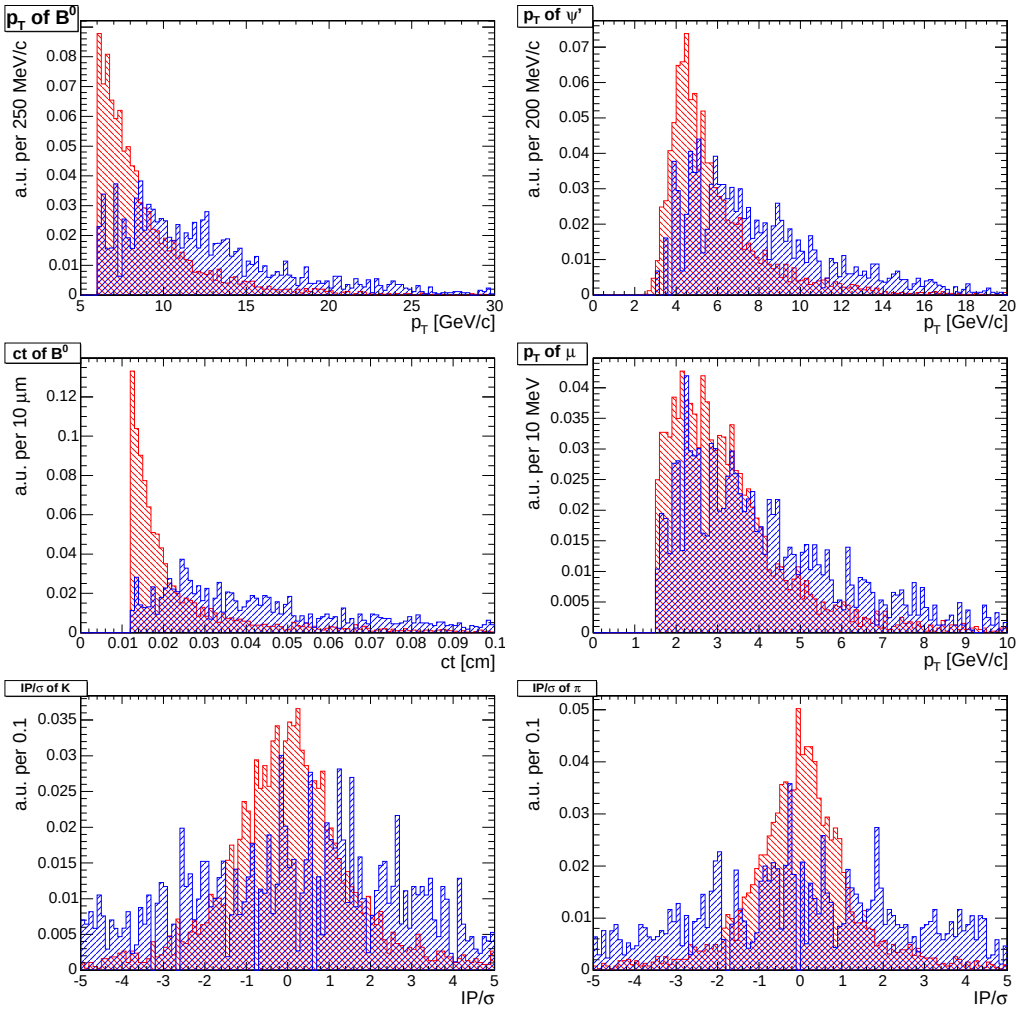

Figure 19: Comparison of sideband-subtracted signal (blue) and background (red) distributions of various kinematic and vertex-quality quantities considered for the optimization.

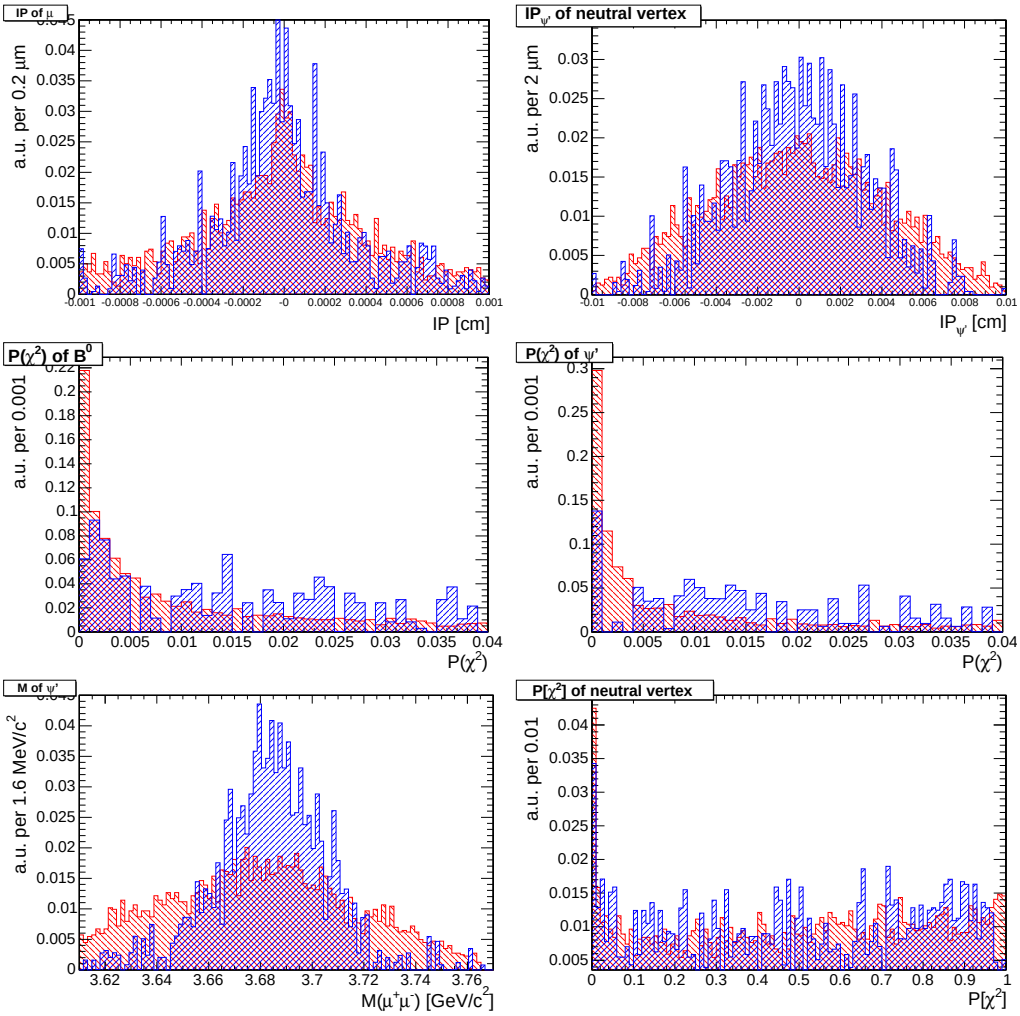

Figure 20: Comparison of sideband-subtracted signal (blue) and background (red) distributions of various kinematic and vertex-quality quantities considered for the optimization.

4.1.2 algorithm and results

For our optimization, we selected a subset of discriminating variable. We chose to use the transverse momenta of the B^0 and $\psi(2S)$ candidates, the impact parameter significance of kaon and pion candidates, the decay-length of the B^0 candidate and the B^0–vertex probability in our optimization. To fully probe the non-factorizable event-density in this six-dimensional space we sampled it according to a discrete grid, detailed in tab. 8. We maximized the figure of merit $f = S/\sqrt{S+B}$ which is used customarily in optimizing prominent signals while keeping enough statistics for precise rate measurements. This somewhat arbitrary choice has probably a marginal impact in our case, where even the choice of optimizing the B^0 signal is known to be suboptimal and is presumably the major limitation of this approach.

Fig. 21 show the value of the figure of merit as a function of the selection probed. Each selection is uniquely identified with an arbitrary integer bitmap I constructed as follows: $I = 10^5 \cdot s_i^{\mathrm{IPsig}(K)} + 10^4 \cdot s_j^{\mathrm{IPsig}(\pi)} + 10^3 \cdot s_k^{p_\mathrm{T}(B)} + 10^2 \cdot s_l^{p_\mathrm{T}(\psi(2S))} + 10 \cdot s_m^{\mathrm{ct}(B)} + s_n^{\mathrm{Prob}(B)}$ where,

Quantity	Range	Step width
$ct(B^0)$	150–300 µm	50 µm
$p_T(\psi(2S))$	3–6 GeV c^{-1}	1 GeV c^{-1}
$p_T(B^0)$	6–12 GeV c^{-1}	2 GeV c^{-1}
$\lvert d_0(K)/\sigma_{d_0}\rvert$	0–4	1
$\lvert d_0(\pi)/\sigma_{d_0}\rvert$	0–4	1
$Prob_{\chi^2}(B^0)$	0.0001–0.0081	0.002

Table 8: Parameters of the optimization algorithm.

for each quantity, s_i is the i-th step in the scan. For each configuration a mass fit similar to the one of fig. 18 was repeated, with a total of 1728 iterations (see Appendix B). This yielded the estimates for S and B used to compute the figure of merit shown in fig. 21. A clear maximum is seen, corresponding to $f \approx 30$. The resulting selection is detailed in tab. 9, with associated mass distribution shown in fig. 22 (left): by maximizing $S/\sqrt{S+B}$ we obtain 1689 ± 59 signal events. The narrow signal is fit with a Gaussian while the model for the background is a parabola. This accounts for the overlapping contribution of a smooth, probably flat combinatorial component, and a wide curve due to signal decays where the $K - \pi$ assignments are swapped. The latter contribution is visible in the mass distribution of simulated signal decays (Fig. 22, right).

Quantity	Requirement for max $S/\sqrt{S+B}$
$ct(B^0)$	> 200 µm
$p_T(\psi')$	> 3 GeV c^{-1}
$p_T(B^0)$	> 6 GeV c^{-1}
$\lvert d_0(K)/\sigma_{d_0}\rvert$	> 1
$\lvert d_0(\pi)/\sigma_{d_0}\rvert$	> 0
$Prob_{\chi^2}(B^0)$	> 0.0021

Table 9: Optimized selection for the B^0 signal.

4.2 THE DALITZ PLOT

One may argue that a selection optimized for the B^0 signal may be very inefficient at collecting $Z^-(4430)$ decays, if any. We decided not to pursue an optimization specifically aimed at maximizing the sensitivity for a $Z^-(4430)$ signal in this part of the work, due to the fact that too many assumptions would be required (e.g. the spin of the $Z^-(4430)$) to simulate the decay. However, even from the B^0-optimized sample, we can extract useful information for further study.

4.2.1 Acceptance

As an initial test, we checked that the above selection does not introduce strong disuniformities in the Dalitz plot acceptance, especially in the region where a possible $Z^-(4430)$ signal may be expected. Fig. 23 (left) shows the Dalitz plot for a simulated sample of non-resonant $B^0 \to \psi(2S)K^+\pi^-$ decays reconstructed through our optimized selection. The quantities

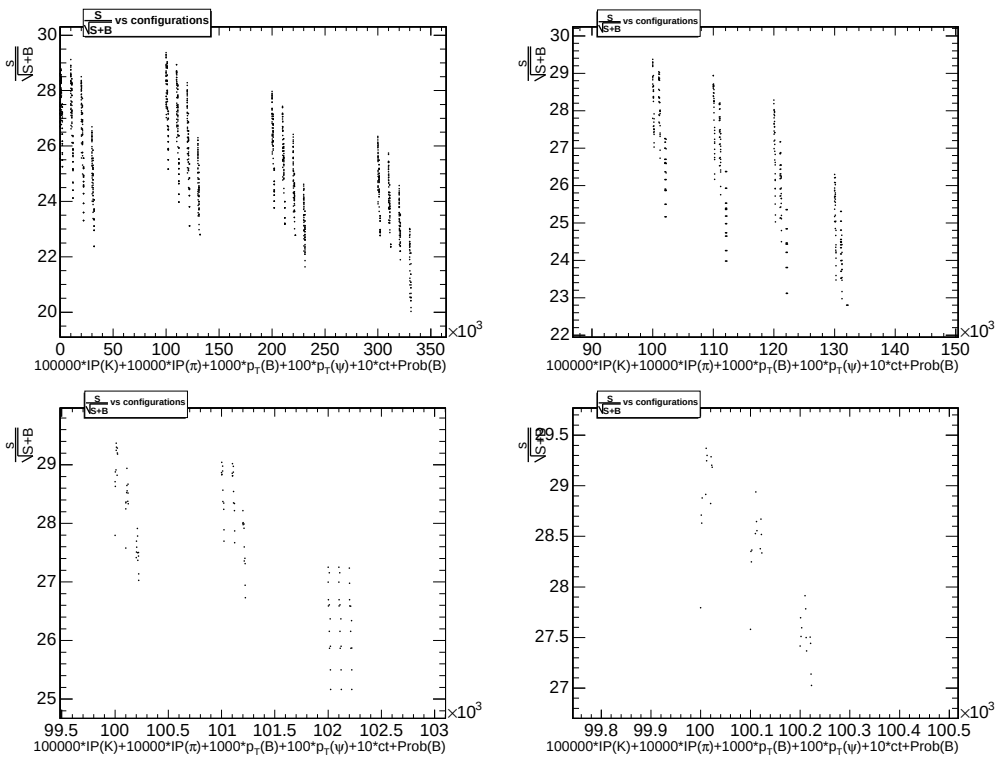

Figure 21: Figure of merit $S/\sqrt{S+B}$ as a function of the integer bitmap chosen to identify the configuration of selection requirements. The three progressive magnifications show in detail the shapes of the figure of merit as a function of the configurations for the different observables.

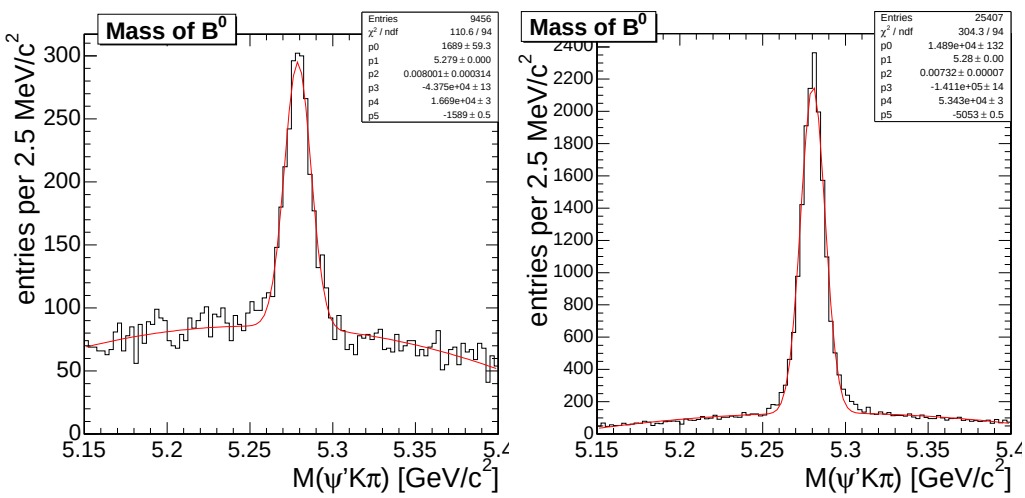

Figure 22: Mass distribution of $B^0 \to \psi(2S)K^+\pi^-$ candidates selected through the optimized selection with fit overlaid, in data (left) and simulation (right).

chosen for the axes are the $K^+\pi^-$ squared mass in the abscissa, and the $\psi(2S)\pi^-$ squared

mass in the ordinate following the Belle and BaBar analyses. The $Z^-(4430)$ signal in data would cluster in a horizontal band centered at $m^2(\psi(2S)\pi^-) \approx 20\ GeV^2c^{-4}$, as shown in fig. 23 (right), for simulation of a spin-0 $Z^-(4430)$ signal with zero natural width. Different choices for spin and width yield similar results.

Inspection of the Dalitz plot shows that our selection does not seem to sculpt the kinematic acceptance for the decays we are searching for; apparently the Dalitz plot is populated uniformly without large variations of density.

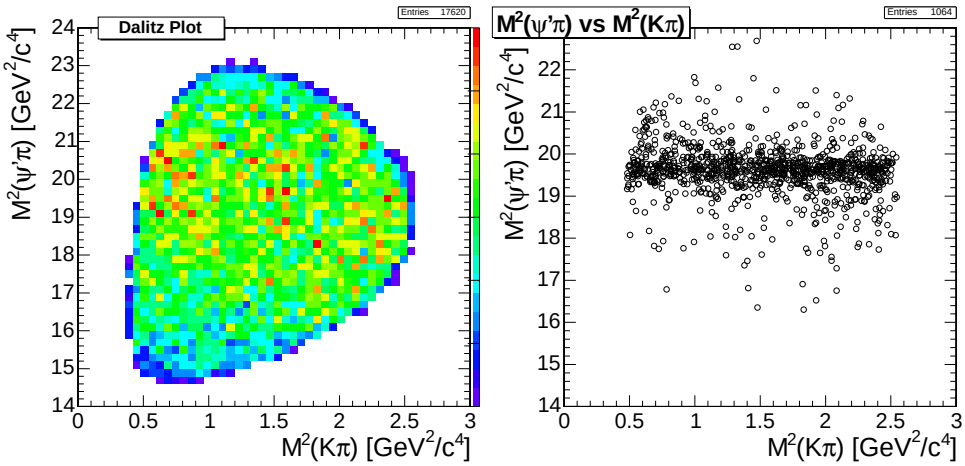

Figure 23: Dalitz plot of the simulated non-resonant $B^0 \to \psi(2S)K\pi$ events (left) and of the simulated spin-0 $Z^- \to \psi(2S)\pi$ decays (right).

4.2.2 Comparison with Belle

Fig. 24 (right) shows the Dalitz plot for B^0 signal candidates in data ($5.255 < m(\psi(2S)K^+\pi^-) < 5.303\,\text{GeV}\,c^{-2}$), whereas in fig. 24 (left) the corresponding plot made by the Belle Collaboration is shown. The gross features of the Dalitz plots look rather similar. In both is clearly visible the vertical band corresponding to the $K^*(892)^0$ resonance at $M^2(K^+\pi^-) \approx 0.7\ GeV^2c^{-4}$, and in Belle's plot also the $K^*(1430)^0$ appears at $m^2(K^+\pi^-) \approx 2\ GeV^2c^{-4}$, while is less clear whether this resonance emerges sufficiently from the background to be visible in our data. An hint for the presence of the $Z^-(4430)$ is visible as an horizontal clustering around $m^2(\psi(2S)\pi^-) \approx 20\ GeV^2c^{-4}$ in Belle's data, while no such structure is visible over the background in CDF data. The background in CDF data seems more prominent than in Belle, as expected from the different experimental environments of the two experiments.

One should also note that, while the CDF plot contains only one final state, i.e. $B^0 \to \psi(2S)[\to \mu^+\mu^-]K^+\pi^-$, Belle includes multiple channels reconstructing the $\psi(2S)$ candidates as di-leptons (e^+e^-, $\mu^+\mu^-$) and from the decay $\psi(2S) \to J/\psi[\to l^+l^-]\pi^+\pi^-$.

4.2.3 The $\psi(2S)\pi^-$ mass distribution

The projections of the CDF Dalitz plot onto both axes are shown in fig. 25. The projection of the $\psi(2S)\pi^-$ mass (right) does not show immediately evident narrow structures, but there are significant contributions that appear to overlap the phase-space curve.

To reduce known background sources that could pollute the region where a $Z^-(4430)$ signal may be present, we removed the $K^*(892)^0$ contribution, very visible in the $m(K^+\pi^-)$ distribution of fig. 25, left. A fit with the sum of a Gaussian and a parabola to the bulk of

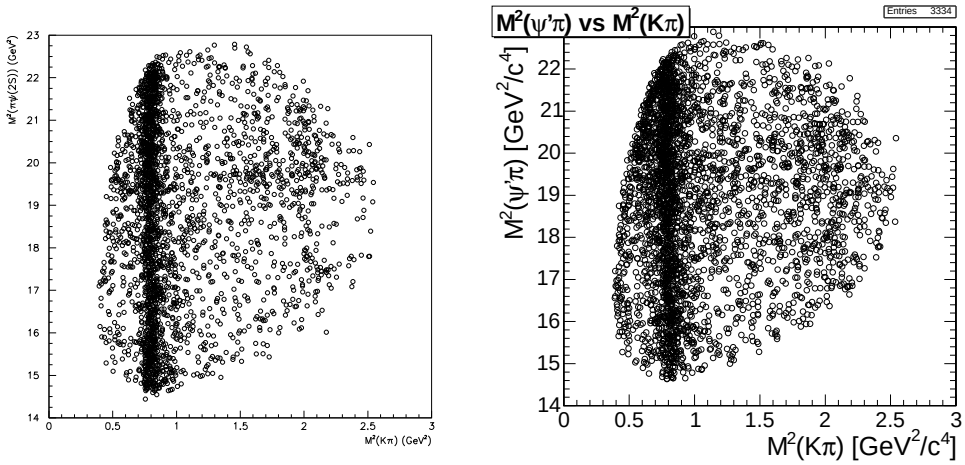

Figure 24: Dalitz plot distribution of CDF events in the signal region (right). Corresponding distributions for Belle data (left).

the $K^*(892)^0$ peak allow removal of all candidates whose mass is within 3σ from the known $K^*(892)^0$ mass [4]. The resulting Dalitz plot and its $m(\psi(2S)\pi^-)$ projection are shown in fig. 26 (right). While Belle also removes the wider $K^*(1430)^0$ resonance, we prefer not to do so for the moment. That contribution is not immediately evident above the background and removing it could adversely impact the already limited size of our sample.

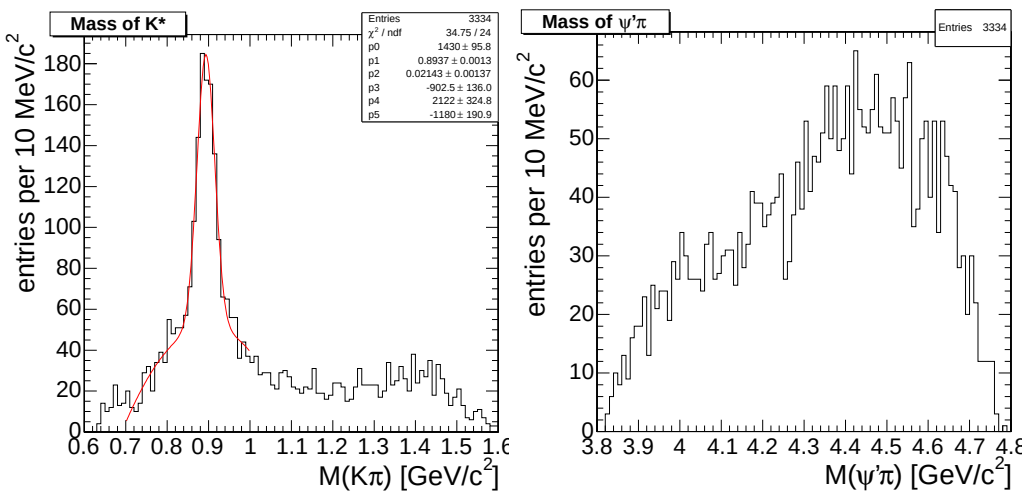

Figure 25: Projections of the Dalitz plot. The invariant $K^+\pi^-$-mass distribution of the sample is on the left panel, with a fit overlaid to the prominent $K^*(892)^0$ peak; the invariant $\psi(2S)\pi^-$-mass distribution of the sample is on the right panel.

Even after subtracting the $K^*(892)^0$, the simple visual inspection of the $\psi(2S)\pi^-$–mass distribution does not suggest an easy comparison with Belle's plot (Fig. 26 (left)). Belle data shows a sharp, narrow peak emerging from a phase-space-like smooth background. Our distribution instead shows a massive, asymmetric bulk of events with no specific narrow structure, but clearly incompatible with simple phase-space.

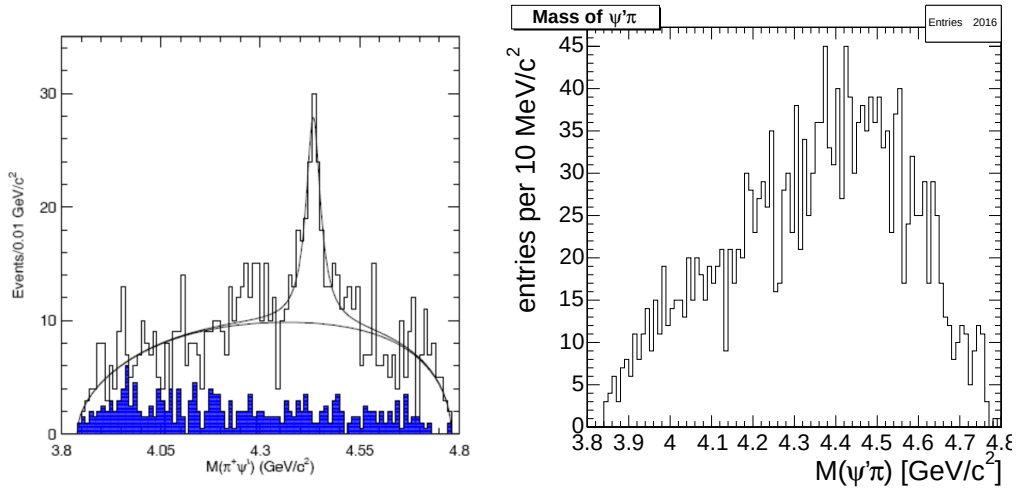

Figure 26: $\psi(2S)\pi^-$–mass distribution after subtraction of the $K^*(892)^0$ resonance for Belle (left) and CDF (right) data.

The first question arising from this comparison is whether the wide bulk we observe could indicate presence of possible narrow signal with degraded mass resolution. Our optimized selection could have isolated a kinematic regime different from the one of Belle, where the resolution of the CDF detector may not be sufficient. Mass plots on the simulated $Z^-(4430)$ signal, however, show that this is not the case (Fig. 27). The simulated spin-0 $Z^-(4430)$ signal, with zero natural width, is clearly visible after the optimized selection with a width compatible with experimental resolution. Similar results are obtained for simulation of $Z^-(4430)$ with spin 1 and 2, and different natural width. We therefore suspect that the excess from the phase-space shape is due to backgrounds. Contributing background can be classified in the following generic classes:

1. non-resonant $B^0 \to \psi(2S)K^+\pi^-$ decays: decays where the $K^+\pi^-$ particles do not resonate into an intermediate metastable particle, and are expected to follow a phase-space distribution across the Dalitz plot.

2. candidates of the type $x \to \psi(2S)h^+h^-$, where h are generic charged particles, and x may identify either a heavy flavored hadron or combinatorial background made of combinations of a real $\psi(2S)$ with random tracks that accidentally seem originated from a common point in space.

3. candidates of the type $x \to h^+h^-h^+h^-$ where even the $\psi(2S)$ candidate originate from combinatorics.

A quantitative estimate of each of the above contributions would be needed to proceed towards a search for any unexpected signal in this channel. However, it will be clear from the next chapters that the inclusive analysis has proved more promising and, for the purpose of this thesis work, we chose to pursue the latter in more detail. For this sample we will just discuss qualitatively some of the features of the above backgrounds.

4.2.4 Non-resonant $B^0 \to \psi(2S)K^+\pi^-$ decays

We studied the shape of non-resonant $B^0 \to \psi(2S)K^+\pi^-$ decays, normalized to their expected contribution in our sample. The shape, obtained from simulated $B^0 \to \psi(2S)K^+\pi^-$

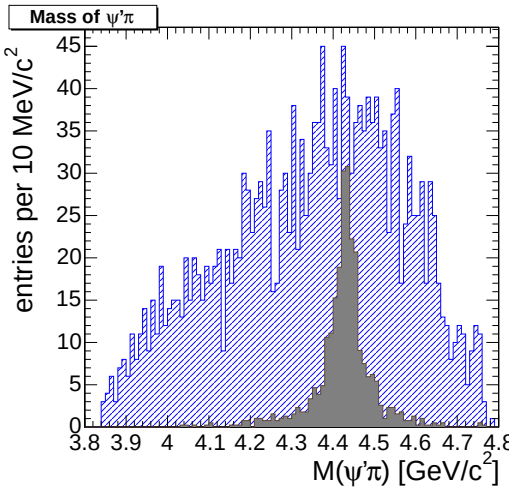

Figure 27: Distribution of the $\psi(2S)\pi^-$-mass with Monte Carlo simulation of a spin-0, 0 MeV c^{-2}-wide Z^- signal overlaid.

decays, reproduces the three-body phase-space distribution. We normalized the simulated sample to the data by rescaling the number of simulated events. The scale factor is obtained from the ratio between the number of events in the region $m^2(K^+\pi^-) > 1.15\ GeV^2/c^4$ and $m^2(\psi(2S)\pi^-) < 18.5\ GeV^2/c^4$ of the Dalitz plot of simulated phase-space $B^0 \to \psi(2S)K^+\pi^-$ decays and the number of B^0 found in the same region in data. These were obtained fitting the B^0 signal in the $\psi(2S)K^+\pi^-$–mass distribution of events restricted to the Dalitz plot range mentioned above. The normalization region was chosen because it is far enough from the $K^*(892)^0$ resonance (which is not simulated in our sample) and marginally contaminated by $K^*(1430)^0$. Overlaying the normalized shape of non-resonant decays to the $\psi(2S)\pi^-$–mass distribution from data we observe that data contain a significant excess of non-phase-space contributions, especially in the region of interest, around the Z^- mass (Fig. 28). These are presumably due to the contribution 2 and 3 described in sec. 4.2.3.

4.2.5 Combinatorial background

Little progress can be made in the "displaced" analysis without a quantitative understanding of the combinatorial background. Many past CDF analyses in flavor physics have shown that use of simulation is of little help in these cases. The complexity of $p\bar{p}$ collisions environment prevents current simulations to reproduce reliably the full details of lower momentum tracks as used in this kind of analyses. For that reason, we prefer to use real data to pursue a deeper understanding of the combinatorial background.

However, it is not straightforward to understand which control samples are suited to estimate this insidious background contributions. As an example of these difficulties we have studied the $\psi(2S)\pi^-$–mass distribution of candidates populating the B^0 mass sidebands, to understand if any of the features of fig. 26 (right) could be explained. Fig. 29 (left) shows in red the $\psi(2S)\pi^-$–mass distributions of candidates in the B^0 mass sidebands ($5.150 < m_{\psi(2S)K\pi} < 5.220\,\text{GeV}\,c^{-2}$) and ($5.330 < m_{\psi(2S)K\pi} < 5.400\,\text{GeV}\,c^{-2}$), compared to the one of candidates populating the B^0 peak (blue), subtracted by the sidebands. Choice of sidebands is illustrated in fig. 29 (right). The two distributions have a different shape, and the "signal" distribution still exhibits a wide cluster of events approximately at $m(\psi(2S)\pi^-) \approx 4.5\,\text{GeV}\,c^{-2}$. However, the choice of using the mass sidebands as control

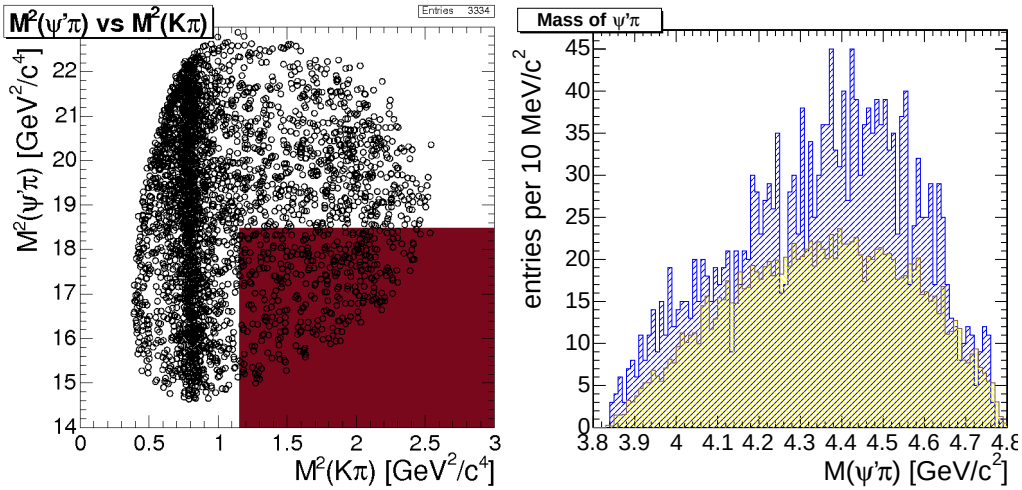

Figure 28: Comparison of non-resonant Monte Carlo events (yellow) and data events (blue). The shadowed area in the Dalitz plot on the left show the normalization region.

sample for background under the peak is based on the assumption that the $\psi(2S)\pi^-$–mass distribution does not vary significantly as a function of the $\psi(2S)K^+\pi^-$ mass. The assumption obviously fails, since there is significant kinematic correlation between the $\psi(2S)\pi^-$–mass and the $\psi(2S)K^+\pi^-$–mass. This is shown in fig. 30, where comparison of sideband-subtracted signal and sideband distributions are shown for two different choices of the sidebands: $5.150 < m_{\psi(2S)K\pi} < 5.220\,\mathrm{GeV}\,c^{-2}$ and $5.330 < m_{\psi(2S)K\pi} < 5.400\,\mathrm{GeV}\,c^{-2}$. This makes it difficult to distinguish differences due to kinematic correlations from those due to different physics contributions that may populate different regions of the $m_{\psi(2S)K\pi}$ distribution.

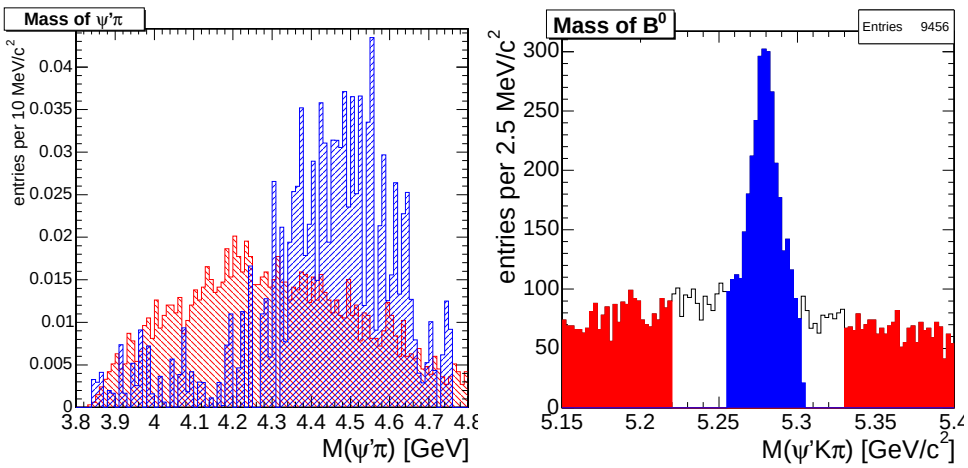

Figure 29: Left plot: Invariant $\psi(2S)\pi^-$–mass distribution of events populating the B^0 peak region (blue) and the B^0 mass sidebands regions (red). Contribution of $K^*(892)^0$ has been subtracted. The right plots shows the choice for the sidebands and signal regions.

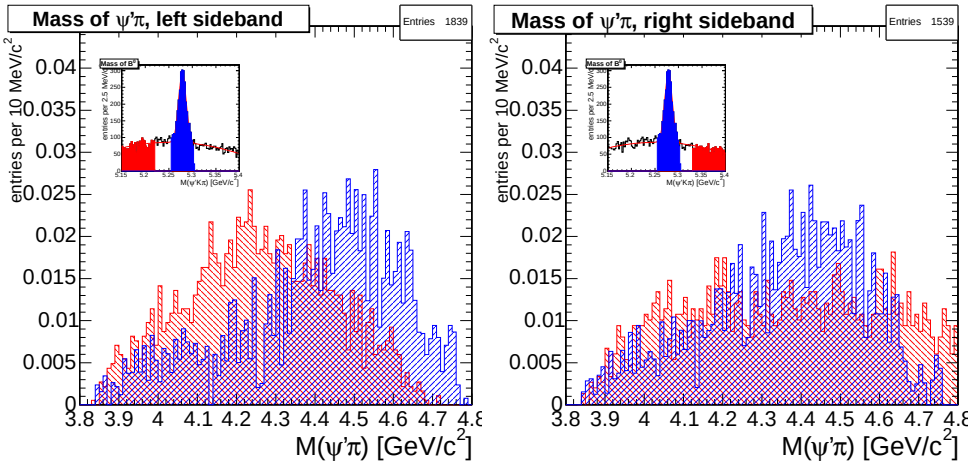

Figure 30: Invariant $\psi(2S)\pi$–mass distribution of events populating the B^0 peak region (blue) and the two choices of the B^0 mass sidebands regions (red) as illustrated in the insets. Contribution of $K^*(892)^0$ has been subtracted.

This simple test with sidebands is described just as an example of the difficulties one can encounter in dealing with backgrounds in this channel. We did not pursue this further, nor we explored in details other solutions because we preferred to focus on the direct search as it will be clear from the following chapters.

4.3 SUMMARY OF THE "DISPLACED" APPROACH

From this exploration of the "displaced" sample, we understood some aspects of the main issues that a CDF search for $Z^-(4430)$ as intermediate state in B-decays would imply.

On the positive side we notice that the B^0 yield at CDF is comparable to those of the B-factories, as summarized in tab. 10. Considering that the B–factories have no major

	$B^0 \to \psi(2S)K\pi$ $\psi(2S) \to l^+l^-$	$B^0 \to \psi(2S)K\pi$ $\psi(2S) \to J/\psi\pi^+\pi^-$	Details
Belle (657M $B\bar{B}$)	1089 ± 34	1166 ± 37	$J/\psi, \psi(2S) \to \mu\mu, ee$
BaBar (455M $B\bar{B}$)	2021 ± 53		$J/\psi, \psi(2S) \to \mu\mu, ee$
CDF (5.7 fb^{-1})	1689 ± 59	–	$\psi(2S) \to \mu\mu$

Table 10: Comparison of $B^0 \to \psi(2S)K\pi$ yields in CDF, BaBar, and Belle.

data samples to add to their analyses, the scenario appears promising. By the end of Run II CDF will almost double the current statistics and a further signal increase will be gained if we include the $\psi(2S) \to J/\psi\pi^+\pi^-$ decays. The 6-tracks mode ($B^0 \to \psi(2S)[\to J/\psi\pi^+\pi^-]K^+\pi^-$) will probably suffer a significant loss in acceptance with respect to the 4-tracks due to the two soft pions, but the product of branching fractions is more favorable and there will probably be less background, due to the narrower mass peak. Preliminary studies based on simulation show that the acceptance for the 6-tracks mode is 1/7 of the 4-tracks acceptance. Part of this will be compensated by the factor 2.5 gain from the branching ratios, with a total additional signal of roughly 35%.

On the other hand we have larger and different backgrounds compared with those present at B-Factories. The main difficulty seems to estimate (or reject) the contribution due to candidates made of real $\psi(2S)$ and random pairs of tracks. Exploiting refined B^0 selections that use additional information to reject combinatorics may be possible, or different possibilities may be available to model the mass shape of those backgrounds (use candidates with negative decay-lengths, $\psi(2S)K^+\pi^+$ candidates, etc...), but further studies are needed to figure out the best strategy.

During this thesis work, we realized that the "direct" search seems to be a more promising approach. We therefore focused our effort in this direction and the remainder of this thesis describes that part of the analysis.

5 THE "PROMPT" CHANNEL

This chapter provides a description of the optimization of physics objects aimed at the direct search of $Z^-(4430)$ decays. We studied in some detail track and muon quality to reach an optimal configuration, using $B^- \to \psi(2S)K^-$ and $\psi(2S) \to \mu^+\mu^-, J/\psi\pi^+\pi^-$ as benchmark signals.

5.1 MOTIVATION

The search for the $Z^-(4430)$ in prompt production mode is suggested by the large phase-space available in 1.96 TeV collisions to create $\approx 4\,\mathrm{GeV}\,c^{-2}$ resonances, which may result in significantly copious signals if production mechanisms are similar to those of charmonium or heavy flavor particles. This strategy proved already successful in 2004 when CDF confirmed the observation of the $X(3872)$, looking for a production not necessarily associated with a B decay and finding a large signal of 730 ± 90 events, corresponding to effective cross-sections of $\mathcal{O}(50)$nb. The main difficulty of this approach is the control of combinatorial backgrounds, which are particularly harmful in high track multiplicity environment as $p\bar{p}$ collisions. However, despite the experimental challenges, inclusive search is unique to hadron colliders and may provide supplementing information, unavailable at the B-Factories experiments, to understand the phenomenology of XYZ mesons.

5.2 COMBINATORIAL BACKGROUND

Fig. 31 shows the $\psi(2S)\pi^-$–mass distribution of candidates after reconstruction and baseline requirements detailed in 3.4. The distribution shows a smooth shape with a high number of entries per bin. The major contribution to this is due to combinatorial background. In fact, Tevatron $p\bar{p}$ collisions produce a large number of particles per interaction ($20 - 200$ tracks per bunch-crossing at $L = 2 \times 10^{32}\mathrm{cm}^{-2}\,\mathrm{s}^{-1}$). As a consequence, the number of $\psi(2S)\pi^-$ candidates per event passing the preselection requirements of the reconstruction (see Sect. 3.4) can be large for events with a high multiplicity of charged tracks. This is caused by the association of random tracks with the $\psi(2S)$ vertex, that generates several candidates corresponding to the same $\psi(2S)$. Fig. 32 shows the multiplicity of $\psi(2S)$ and $\psi(2S)\pi^-$ candidates. While the large majority of events have only one $\psi(2S)$ candidate with 0.1% contamination of multiple $\psi(2S)$, the situation is strongly different for $\psi(2S)\pi^-$ multiplicities. The distribution peaks at ≈ 5 candidates per event with significant tails extending up to 20 candidates per event. Large combinatorial background would "dilute" any small signal present in data, which would be overwhelmed by the smooth distribution of combinatorics.

In order to limit the adverse effect of too large combinatorial backgrounds, we studied tightened requirements on track and muon quality, which may improve the purity of our $\psi(2S)$ candidates and reduce the probability of associating them with random tracks in common vertices. The studies have been performed using a small subsample of ≈ 200 pb^{-1}, corresponding to about 8 million events, by comparing $\psi(2S)$ and $B^- \to \psi(2S)K^-$ signal yields across different configurations for track and muon quality.

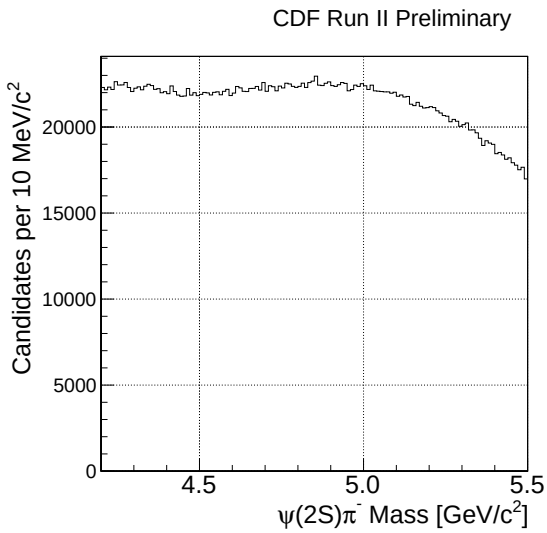

Figure 31: Invariant $\psi(2S)\pi^-$–mass distribution of the candidates selected through the baseline requirements of the reconstruction.

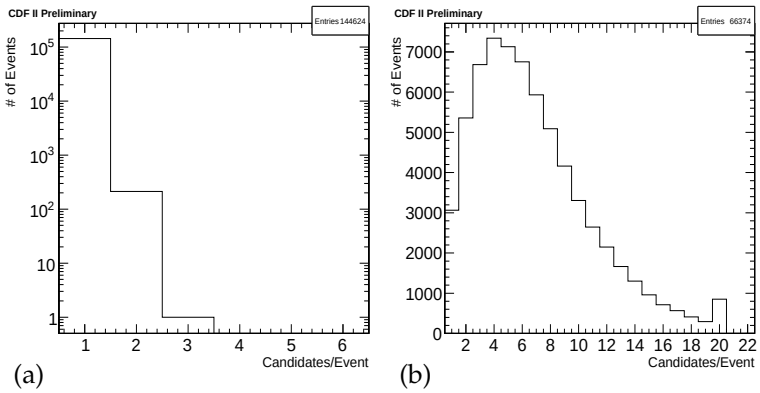

Figure 32: Multiplicity of $\psi(2S)$ (a), and $\psi(2S)\pi$ (b) candidates. In the right plot the last bin contains overflow entries.

5.3 TRACK QUALITY STUDIES

The quality of tracks used in the reconstruction may affect the efficiency and purity of the reconstruction algorithm. Well-reconstructed tracks improve the discriminating power of variables, such as the vertex χ^2 probability, used to reject fake candidates. Usually, a common set of quality requirements is used in heavy flavor analyses at CDF. This was optimized at the beginning of Run II and has become standard practice. However, when specific analyses require it, custom tightened selections may be used.

In our case, the impact of more stringent requirements on track quality has been studied evaluating the yield of $B^- \to \psi(2S)K^-$ decays, with different requirements on the number of associated hits in the drift chamber and silicon detector. We used $B^- \to \psi(2S)K^-$ decays because they reproduce closely the topology and kinematics of $Z^-(4430) \to \psi(2S)\pi^-$ decays, thus being a reliable probe for these studies. We reconstructed the B^- signal as a $\psi(2S)\pi^-$ resonance. The shift in mass and the increased width due to $K-\pi$ misassignment

are not relevant for this study because the B^- shape is still clearly visible and allows estimation of signal and background at a level adequate for our purpose. Mass distributions in fig. 33 show an evident B^+ signal of approximately 150 candidates overlapping a substantial background of $20-30$ candidates per bin. We use a χ^2 fit to fit the distribution modeling the background with a parabola and the signal with a Gaussian (Fig. 33). Quantitative estimation of the uncertainties or a more refined modeling of the distributions are not needed, also because we will be comparing results obtained with same approximations, so any mismodeling will cancel in the ratios, at first order. We probed several different configurations and combinations in terms of silicon and drift chamber hits. An example of the results of these studies is shown in fig. 33 and summarized in table 11.

Minimum COT hits	Minimum silicon hits	Signal	Background	S/B
10 axial and 10 stereo	3 axial	≈ 170	≈ 305	0.5
10 axial and 10 stereo	3 axial and 3 stereo/z	≈ 155	≈ 220	0.7
20 axial and 20 stereo	3 axial and 3 stereo/z	≈ 148	≈ 226	0.7

Table 11: B^- signal and background yield in the $\psi(2S)\pi^-$–mass distribution with different track quality configuration.

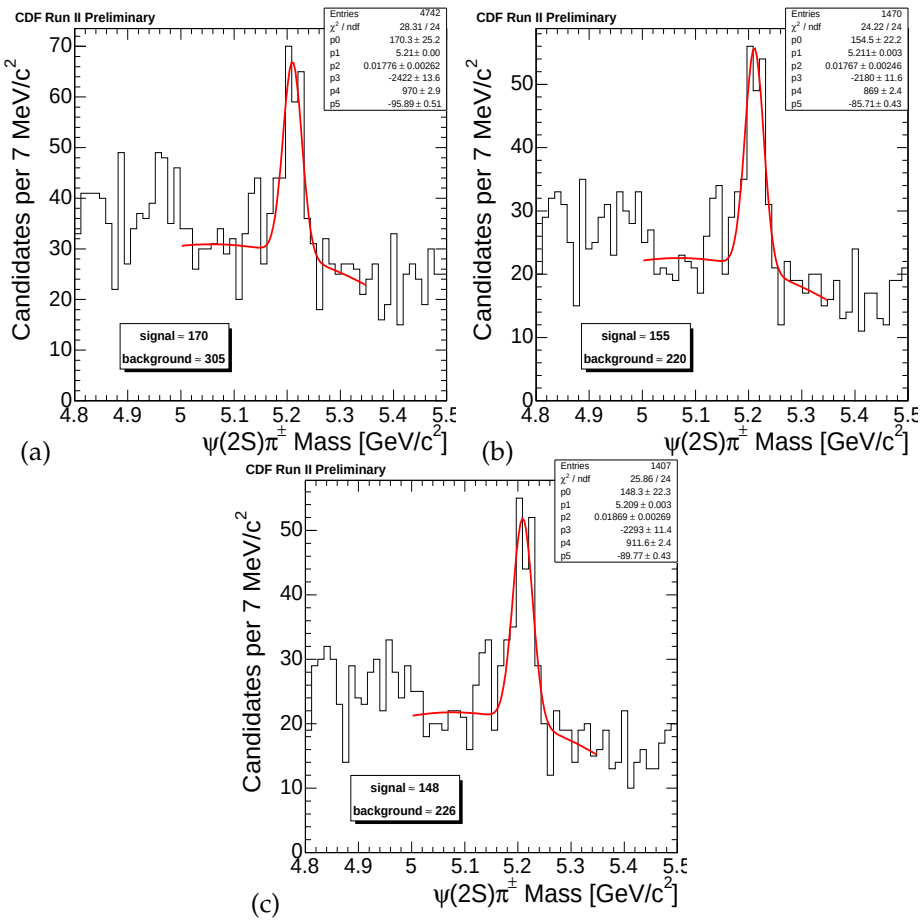

Figure 33: Invariant $\psi(2S)\pi^-$–mass distribution with standard requirements (a), additional requirements on silicon hits (b), additional requirements on both silicon and COT hits (c).

The improvements in signal purity provided by tightened requirements on track quality are limited, in case of additional requirement of silicon hits, or marginal, if any, when varying the number of required hits in the chamber. We therefore chose to tighten only the requirements on silicon hits for all tracks used in the analysis, by requiring at least three axial and three stereo/z hits per track.

5.4 MUON QUALITY STUDIES

Increasing the purity of the $\psi(2S)$ sample may help in reducing combinatorics. Fig. 34 shows that the background contamination under the peak of the $\psi(2S)$ is considerable, with a signal over background ratio of about 0.24. From previous CDF analyses we know that the main contribution to the background come from real muons produced in decay-in-flight of kaons and pions and from hadrons reaching the muon detectors without undergoing interactions with nuclei of the detector material (punch-through). Smaller contributions arise from double semileptonic decays of $b\bar{b}$ pairs, sequential semileptonic decays $b \to c \to s$, and Drell-Yan process. So far we have used loose muons, i.e. those required only to have track-matching with hits in the innermost muon detectors (CMU or CMX). We can reduce the punch-through contribution requiring muons to have an additional matching in the outermost muon detector, the CMP (tight muons). On the other hand, we expect also some reduction of signal, due to the reduced kinematic (p_T threshold increasing from ≈ 2 to $\approx 3\,\mathrm{GeV}\,c^{-1}$) and geometric (coverage reduced from $|\eta| < 1.0$ to $|\eta| < 0.6$) acceptance of the outer layer of muon detectors.

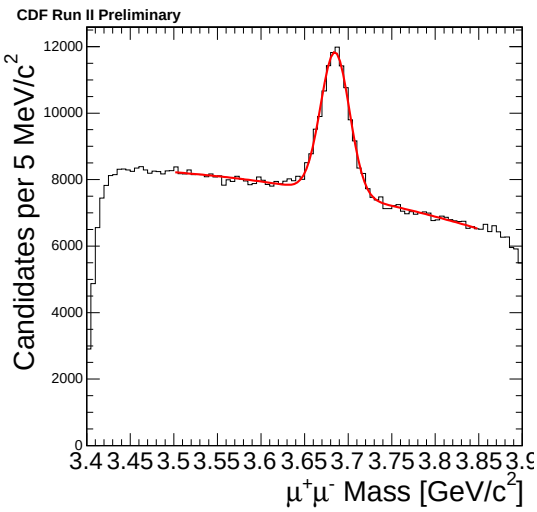

Figure 34: Invariant di-muon mass distribution with baseline requirements.

We have studied how the $\psi(2S) \to \mu^+\mu^-, J/\psi\pi^+\pi^-$ yield and the signal-to-background ratio vary in the following configurations: without any requirement of tight muons, requiring at least one tight muon, or requiring both muons to be tight. The number of signal and background candidates is extracted with a fit of the $\psi(2S)$–mass distribution using a parabola (background) and a Gaussian (signal). A χ^2 fit is performed in a mass region symmetrical around the $\psi(2S)$ peak. The results are shown in table 12 and are discussed in the following.

5.4.1 The $\psi(2S) \to \mu^+\mu^-$ sample

Figure 35 shows how the S/B ratio improves in the di-muon sample after requiring one or two tight muons, increasing from about 0.24 to about 0.6 or 1.5 respectively. On the other hand, the signal yield is reduced by a factor 9 when requiring two tight muons, mostly due to the reduced coverage in pseudorapidity of the outer muon chambers ($|\eta| < 0.6$, to be compared with $|\eta| < 1.0$). We believe this reduction is acceptable, given that the production rate of the $Z^-(4430)$, if it exists, may be high enough to allow some inefficiency while achieving a cleaner muon sample to reduce combinatorics.

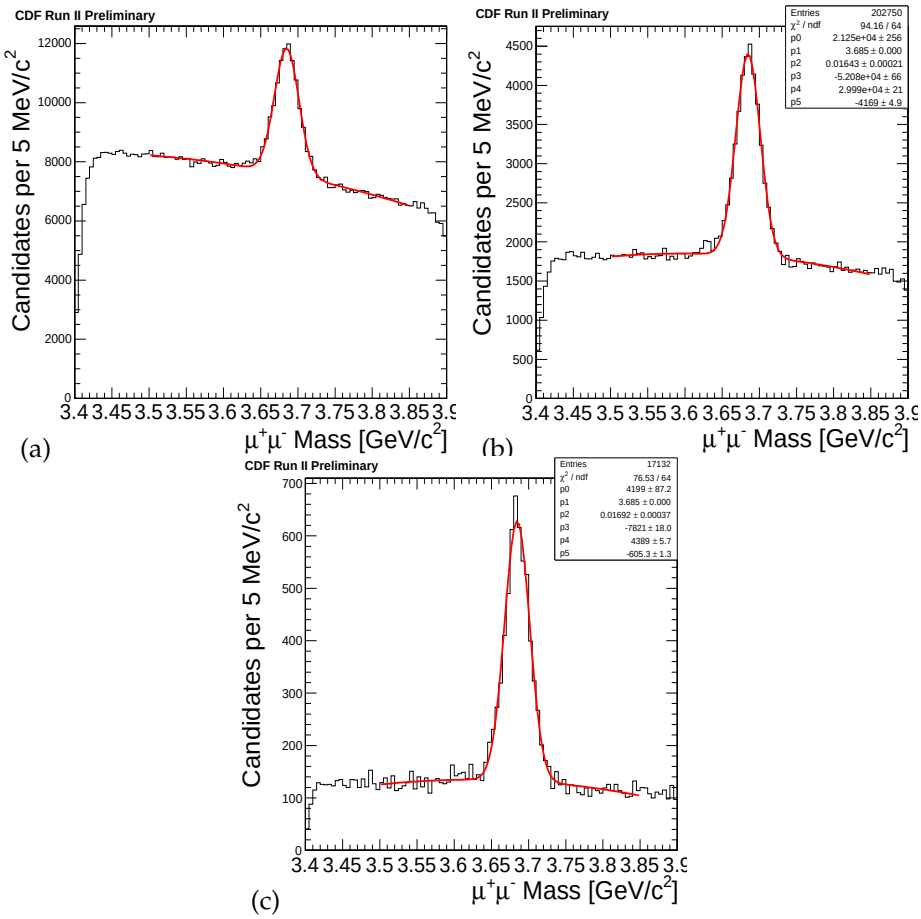

Figure 35: Invariant mass distribution of di-muon $\psi(2S)$ candidates with no tight muon requirements (a), at least one tight muon (b), both tight muons (c).

A muon with p_T greater than 1.5 GeV c^{-1}, approximable to a minimum ionizing particle, looses on average 2 MeV cm^2 g^{-1}, when traversing matter. The mean energy loss of muons across the 60 cm of iron between CMU and CMP is then about 1 GeV. We therefore expect a further inefficiency on signal, when requiring the muons to be tight. We checked if the improvement in purity brought by tight muons (Fig. 35(c)) is only due to the transverse momentum threshold, indirectly applied by requiring the matching with the outermost chamber or if a net benefit is provided by the requirement of additional matching of tracks with muon stubs in the outer chambers.

Fig. 36 shows the di-muon mass distribution for loose muons (a) and for loose muons with p_T greater than 3.0 GeV c^{-1} (b). Also in this case the S/B improves, from 0.24 to 0.77. But the comparison with the distribution in fig. 35(c), where the two tight muons

requirement is applied, shows that there is an additional rejection power in requiring tight muons, which further doubles S/B. The 60 cm-thick layer of iron between inner and outer chambers helps to actually reduce punch-through of hadrons that have additional dense material to pass before reaching the outer chambers.

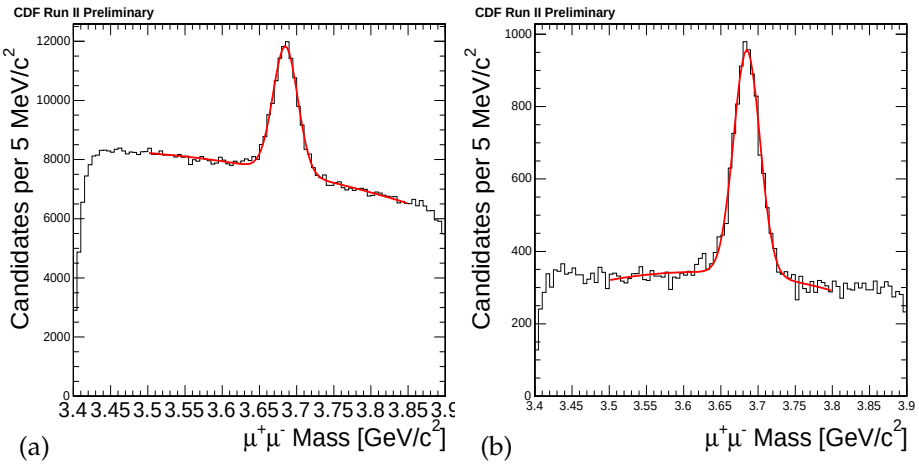

Figure 36: Invariant mass distribution of di-muon $\psi(2S)$ candidates with no tight muon requirements (a), and with the requirement for both muons to have transverse momentum greater than 3.0 GeV c^{-1} (b).

Moreover, if we apply both the requirements, i. e. two tight muons and p_T greater than 3.0 GeV c^{-1} (Fig. 37), we are selecting candidates formed by purer muons combining the benefits of both tight selection and p_T threshold, so that the purity of the $\psi(2S)$ sample further increases with a S/B ratio of about 2.1. Therefore we chose this as our final configuration in the $\psi(2S) \to \mu^+\mu^-$ sample.

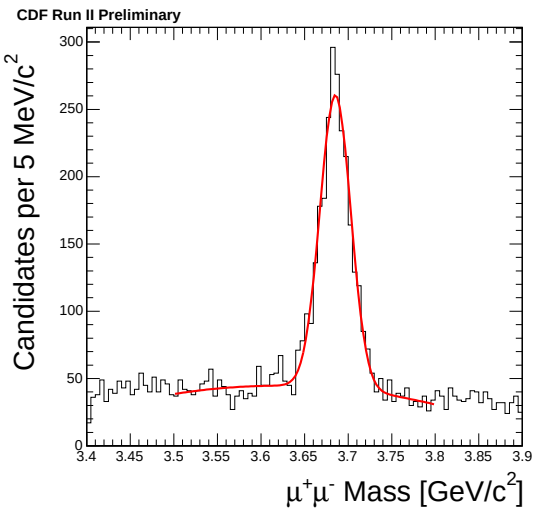

Figure 37: Invariant mass distribution of di-muon $\psi(2S)$ candidates with requirement of two tight muons with transverse momentum greater than 3.0 GeV c^{-1}

5.4.2 The $\psi(2S) \to J/\psi\pi^+\pi^-$ sample

We also evaluated the possibility of improving the signal purity in the $\psi(2S) \to J/\psi\pi^+\pi^-$ decay by requiring tight muons. More background is expected in this case, because of the combinatorics due to the double track association with the J/ψ candidates, but also a better resolution on $\psi(2S)$ mass may be available, because of the mass constraint provided by the J/ψ intermediate state.

Fig. 38 shows the di-muon mass distribution of the J/ψ candidates with different requirements of tight muons. The signal over background ratio increases from about 4 (no requirements) to 13 (both muons tight). The factor 9 reduction of signal is consistent with what observed for the $\psi(2S) \to \mu^+\mu^-$. However, we notice that the purity of this sample is already very high with loose muons ($S/B \approx 4$) and the signal loss due to tightened requirements on muons may not be worth in this case.

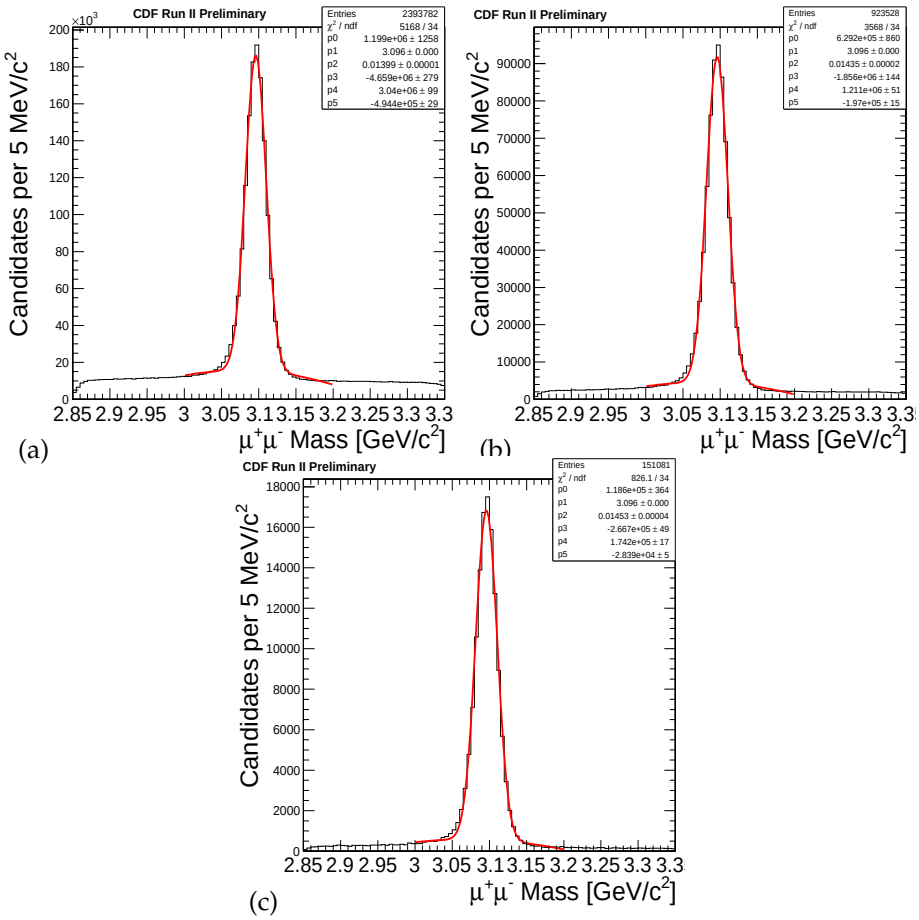

Figure 38: Invariant mass distribution of J/ψ candidates with no tight muon requirements (a), at least one tight muon (b), both tight muons (c).

In addition, studying the J/ψ purity is useful but ultimately we are interested in the final impact on the $\psi(2S)$ sample. If we consider the $J/\psi\pi^+\pi^-$–mass distributions (Fig. 39), the overall benefit of requiring tight muons is reduced with respect to the $\psi(2S) \to \mu^+\mu^-$ sample. The largest contribution to background in this case comes from the combinatorics due to the association of two tracks with the J/ψ candidates and purifying an already pure sample of $J/\psi \to \mu^+\mu^-$ decays provides little benefit.

Table 12 summarizes the results of the studies on muon quality requirements. Note also that the contribution of the $\psi(2S) \to J/\psi\pi^+\pi^-$ sample to the total $\psi(2S)$ yield is small with respect to the $\psi(2S) \to \mu^+\mu^-$ sample. Assuming to use muons of same quality in both channels, adding $\psi(2S) \to J/\psi\pi^+\pi^-$ decays would increase the total signal yield by 20% with loose muons and 40% with tight muons. This, combined with the observed lower $\psi(2S)$ purity, convince us that there are little advantages in adding the $\psi(2S) \to J/\psi\pi^+\pi^-$ sample, at least in this first iteration of the analysis.

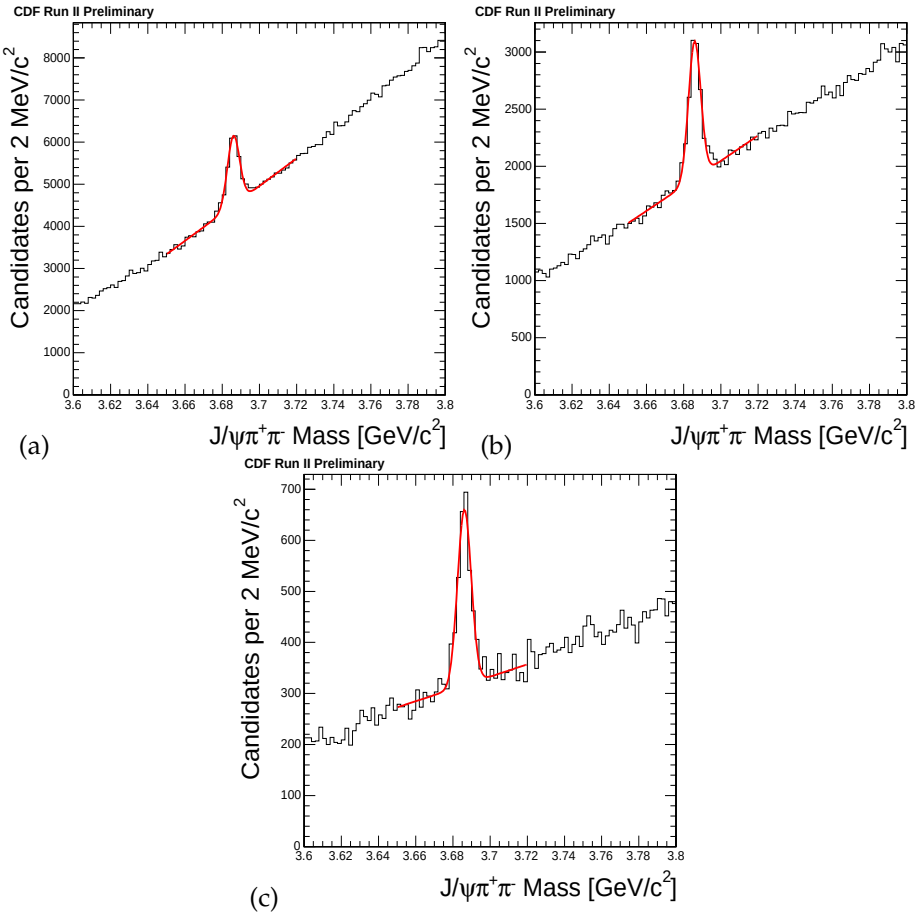

Figure 39: Invariant mass distribution of $J/\psi\pi^+\pi^-$ candidates with no tight muon requirements (a), at least one tight muon (b), both tight muons (c).

5.5 FINAL CONFIGURATION AND FIRST LOOK AT THE $\psi(2S)\pi^-$ MASS DISTRIBUTION

Based on these studies, for this thesis, we decided to perform the analysis using the $\psi(2S) \to \mu^+\mu^-$ sample only, with the requirement for the tracks of three stereo hits, and for both muons to be detected also in the outer chamber. The transverse momentum of the two muons is required to be greater than $3.0\,\mathrm{GeV}\,c^{-1}$.

With the optimal configuration for muons and tracks we perform the reconstruction of the $\psi(2S)\pi^-$ candidates as detailed in Chapter 3. We do not select explicitly the $\psi(2S)$ signal region in mass, but we exploit a basic probability cut ($P[\chi^2]_{\psi'\pi} > 10^{-4}$) on the

Decay channel	Tight muons	Signal (S)	Background (B)	S/B
$J/\psi \to \mu^+\mu^-$	no requirement	10^6	2.5×10^5	4
	≥ 1	6.3×10^5	7.4×10^4	9
	2	1.2×10^5	9350	13
$\psi(2S) \to \mu^+\mu^-$	no requirement	35400	150000	0.24
	≥ 1	21300	35800	0.59
	2	4200	2700	1.56
$\psi(2S) \to J/\psi\pi^+\pi^-$	no requirement	6750	44100	0.15
	≥ 1	4950	18700	0.26
	2	1600	3500	0.46

Table 12: B^- signal and background yield in the $\psi(2S)$–mass distribution with different requirement of tight muons.

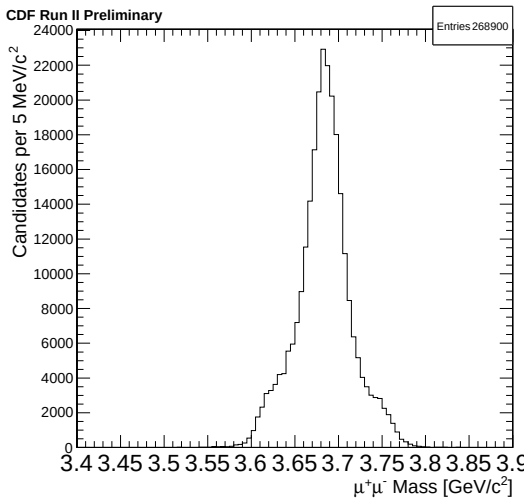

Figure 40: $\psi(2S)$–mass distribution with $P[\chi^2]_{\psi'\pi} > 10^{-4}$.

quality of the vertex fit where the $\psi(2S)$ mass enter as a constraint. Fig. 40 shows that this requirement on fit probability remove candidates far from the peak. Essentially, it corresponds to a selection of the mass region, but slightly improved, because candidates in the mass range are weighed according to the probability to originate from a common vertex.

Looking at the $\psi(2S)\pi^-$ mass distribution resulting from the final configuration (Fig. 41) we see a featureless smooth background distributed with roughly 1700 entries per channel between 4.2 and 5.5 GeV c^{-2}. We see no indication of the $B^- \to \psi(2S)K^-$ signal (reconstructed as $\psi(2S)\pi^-$) that is expected to peak at around 5.2 GeV c^{-2}. The combinatorial background is still copious despite improved muon and track selections.

We therefore search for a $B^- \to \psi(2S)K^-$ signal in the sample, as a first validation of the reconstruction code. The most discriminating information when trying to isolate B decays is the requirement of a displaced secondary vertex, due to the 1.5 ps lifetime of B-hadrons. We know that the selection of candidates with ct (see eq. 3.1) greater than 60 µm preserves roughly 85% of signal, removing a large amount of "prompt" background. With this configuration we obtain the $\psi(2S)\pi^-$–mass distribution in fig. 42, where a prominent B signal is evident at about 5.2 GeV c^{-2}. The shape of the peak has a tail at lower mass because

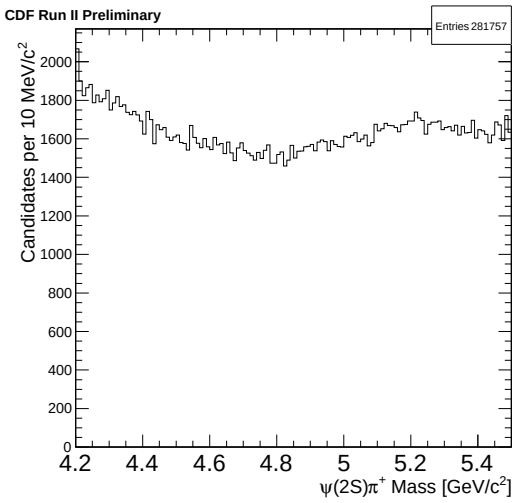

Figure 41: Invariant $\psi(2S)\pi^-$–mass distribution of candidates selected through baseline reconstruction requirements.

of the $K - \pi$ misassignment to the track, but the signal is visible over the combinatorial background, reduced of a factor of about 30 with respect to fig. 41.

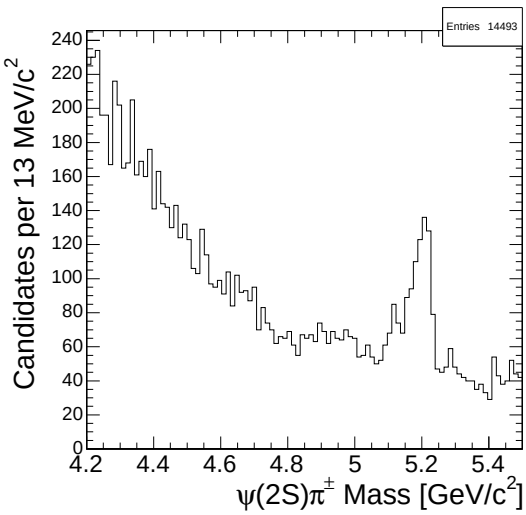

Figure 42: Invariant $\psi(2S)\pi^-$–mass distribution of candidates with $ct > 60\,\mu$m.

The observation of a B signal provides a first validation of our reconstruction code. I provides confidence that the vertex fitting is done correctly and would reconstruct also a $Z^-(4430) \to \psi(2S)\pi^-$ resonance, which has topology and kinematics similar to the $B^- \to \psi(2S)K^-$. However, we aim at searching for the $Z^-(4430)$ signal. We do not know the lifetime of this particle, nor we know what fraction of them would be produced in decays of long lived mesons. We therefore prefer to avoid the requirement of a secondary vertex and we try to extract a visible B signal without any ct requirement.

This is done by requiring tracks with higher transverse momentum and a better vertex quality. Since the b-quark is heavy, B decay products have higher valued transverse momenta than light flavor tracks, and combinatorial candidates have a worse vertex quality than signal. With these requirements ($p_T(\pi) > 3.6\,\mathrm{GeV}\,c^{-1}$ and $P[\chi^2]_{\psi(2S)\pi} > 4 \times 10^{-4}$) the distribution in fig. 43 is obtained. The peak corresponding to the $B^- \to \psi(2S)K^-$ is evident. As expected, the tail due to the wrong mass assignment to tracks is less pronounced than in fig. 42, since we are selecting tracks with relatively high transverse momentum.

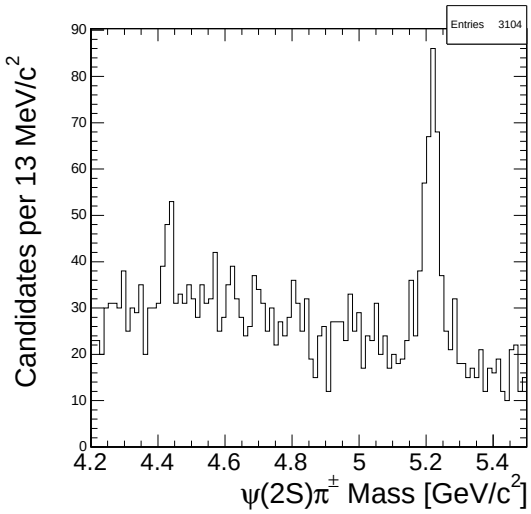

Figure 43: Invariant $\psi(2S)\pi^-$-mass distribution of candidates selected to a tightened set of requirements.

This plot shows also a cluster of candidates at about $4.4\,\mathrm{GeV}\,c^{-1}$, which is the mass range where a $Z^-(4430)$ could appear. We want to check if this interesting structure could be a first indication of a genuine signal of the type we are searching for.

5.6 PEAKING BACKGROUND

Structures like the one observed in fig. 43 at about $4.4\,\mathrm{GeV}\,c^{-2}$ could be caused by other heavy flavor decays (mostly B hadrons, in this mass range) after misreconstruction of final states. In the reconstruction of these processes one or more decay products may be missing and this shifts the mass distribution at lower values with respect to the B-mass, and distorts it. The cluster at $4.4\,\mathrm{GeV}\,c^{-2}$ appears narrow, and usually mass peaks from misreconstructed decays do not show narrow peaks, because of smearing due to misreconstructed kinematics. However, we checked which contributions may populate the region of interest. We are particularly interested at decays of $B \to \psi(2S) + \mathit{anything}$ reconstructed as $\psi(2S)\pi^-$ final states, since we expect these to be the major offenders, being our $\psi(2S)$ selection rather pure. We used samples of B^0, B^+ and B_s^0 decays to any known final state involving a $\psi(2S)$, simulated as detailed in sec. 3.3.1.

Fig. 44 shows the mass distribution of the various simulated contributions, reweighed according to the relative production cross-sections and branching ratios [4]. The distributions have different shapes related with the number of particles, and their species, missing in the misreconstruction. In particular the decays with an intermediate $K - \pi$ resonance ($B \to \psi(2S)K^*(892)$, charged, in red, or neutral, in green) show two distinct broad shapes,

peaking at about 4.7 and 5.1 GeV c^{-2}, depending on which final product, kaon or pion, is missing in the reconstruction. The reconstruction efficiency of the $B^0 \to \psi(2S)K^0$ (yellow) is very low, because the pions from K_S decays do not form a vertex with the $\psi(2S)$, while the $B_s \to \psi(2S)\phi$ contribution is tiny because B_s^0 have a smaller production rate. However, no clear peaking structure in the region around 4.4 GeV c^{-2} is seen. This provides confidence that the observed narrow excess at 4.430 GeV c^{-2} is unlikely to be caused by misreconstruction of known B decays.

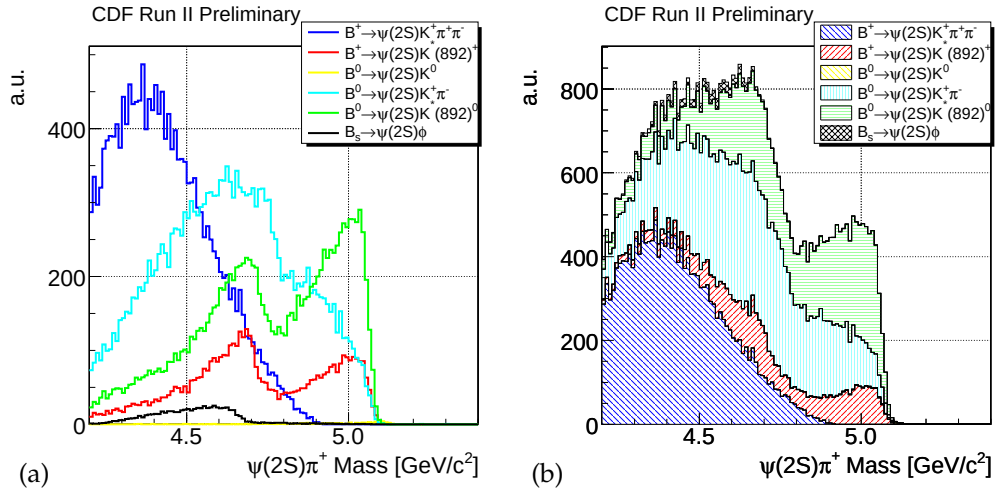

Figure 44: $\psi(2S)\pi^-$–mass distribution of the misreconstructed B decays from simulation superimposed (a) and stacked (b).

5.7 THE $Z^-(4430)$ REGION

A magnification of the region of interest in the range 4.2 GeV $c^{-1} < m_{\psi(2S)\pi^-} < 4.7$ GeV c^{-1} and a fit show that the excess is located at (4432 ± 4) MeV c^{-2} and the width (13 ± 3) MeV c^{-2} is compatible with the width of the nearby B signal[1]. The fit is performed modeling the signal as a Gaussian while the background is approximated to a straight line.

At this point we have multiple independent indications that we may be seeing $Z^-(4430)$ decays in CDF data. We see an excess at the mass where a signal would be expected from Belle's result, with width compatible with experimental resolution, and not caused by any known B-decay source. However, the selection that produced the plot in fig. 43 has been obtained with a manual tuning of the requirements and risk of bias is real in such practices. We therefore decided to do an unbiased optimization of the selection to investigate whether the excess is significant. The next chapter is devoted to the description of optimization and significance estimation.

1 reported uncertainties are only statistical

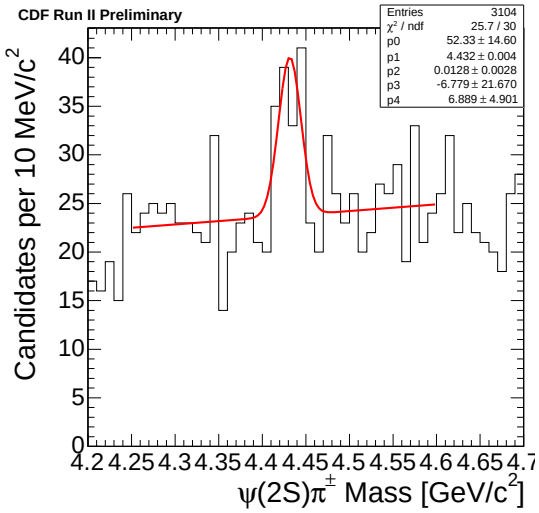

Figure 45: Invariant $\psi(2S)\pi^-$–mass distribution in the region of interest for the $Z^-(4430)$ with fit overlaid.

6 SEARCH OPTIMIZATION

In this chapter we provide a description of the optimization procedure applied in the analysis of the "prompt" channel. The procedure is new and was first applied in this measurement.

6.1 CONCEPT

Optimizing a selection typically involves defining a figure-of-merit suited for the measurement at hand (expected signal-to-noise ratio, expected statistical uncertainty on a given parameter, and so on), and maximizing it as a function of selection requirements on some discriminating quantities used to select the sample. A certain degree of arbitrariness is involved in the choice of the figure of merit and of the discriminating observables, but avoiding biases is always desirable. The optimization is required to be unbiased to ensure reliability and reproducibility of the results: an unbiased optimization minimizes the risk of artificially enhancing signals, or even producing false ones, by avoiding selection requirements that exploit statistical fluctuations of the finite size sample rather than actual differences in parent distributions of different classes of events.

Typical optimizations define a figure of merit $f(\mathcal{S}_i, \mathcal{B}_i)$ as a function of the number of 'signal' events for the i-th configuration of the cuts ($\mathcal{S}_i$), and the number of 'background' events for the same configuration ($\mathcal{B}_i$). The choice of how 'signal' and 'background' events are defined is critical for the prevention of bias in the final result. The best possible choice would be to use high statistics samples of simulated signal and background events, obtain the optimal configuration and apply it to the data. This is certainly unbiased. However, this is optimal only under the assumption that the simulation is accurate enough in reproducing the features of signal, background, and trigger, detector, physics-objects reconstruction etc.. This is rarely the case, especially in hadronic collision environments. A popular 'compromise' is to use simulation just to characterize signal events, typically more reliably simulable than backgrounds, using control samples in data as models of background. This choice is only partially unbiased, because the signal information input to the optimization algorithm is independent from the actual data to be used in the measurement, but the background information is no longer so, being extracted from the data themselves. In addition, this solution may be suboptimal because, often, not all signal features are known or properly reproduced by the simulation. Therefore several, possibly powerful, discriminating variables may remain excluded from optimization. For others, assumptions or manipulations (e.g. reweighting) are required, jeopardizing the optimality of the procedure.

In our case, the main features (p_T-distribution, lifetime, spin, etc.) of the signal are unknown. It would be difficult to pursue an optimization based on $Z^-(4430)$ simulated samples that remains optimal whatever such features of the signal. We decided to use an alternative approach based on data [3]. This is made possible because the mass region where we expect a potential signal is known from Belle's measurement.

6.1.1 A data-based unbiased optimization

The method uses only data to estimate both signal and background yields for any probed configuration. It is implemented as follows:

- Consider the data sample S in which an optimization of the selection is required.
- S is subdivided into two mutually exclusive subsamples, A and B, using a random criterium.
- The same optimization procedure is applied *independently* on both subsamples:
  1. A criterium is defined to identify the signal events $\mathcal{S}_i^A$ surviving the i-th configuration of the selection cuts in sample A — e. g. estimating all events in a specific mass range ('peak');
  2. A criterium is defined to identify the background events $\mathcal{B}_i^A$ surviving the i-th configuration of the selection cuts in sample A — e. g. estimating all events in another mass range ('sidebands');
  3. The chosen figure-of-merit, $f(\mathcal{S}_i^A, \mathcal{B}_i^A)$, is maximized over the space of configurations for the selection requirements (e. g. all combinations of cuts);
  4. The configuration of cuts corresponding to the maximum of f defines the set of cuts optimized in sample A;
  5. Steps 3–4 are repeated in sample B to obtain the set of cuts optimized in sample B, different in general from the one obtained in sample A.
- The final sample used for analysis is obtained by applying to the subsample B the cuts optimized in sample A and viceversa.

Fig. 46 shows a simplified flow chart of the procedure.

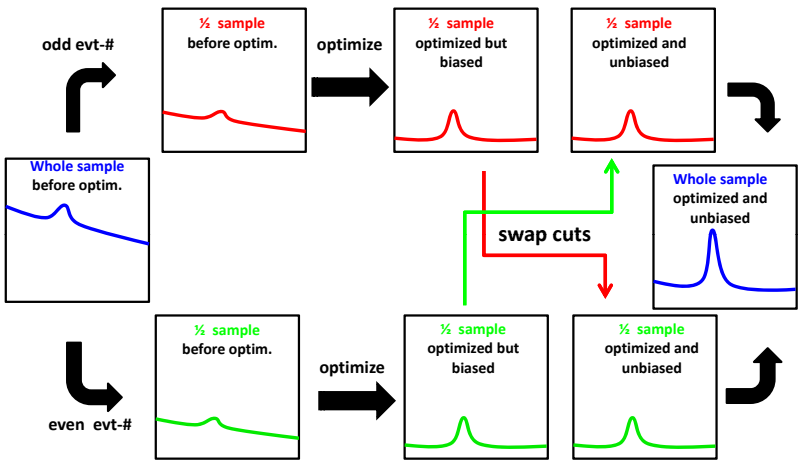

Figure 46: Scheme of the data-based optimization procedure.

The procedure is statistically unbiased. A limitation is that this is scarcely effective for small signals, i. e. signals whose size is comparable with statistical fluctuations of background. In pathologic cases, where the seeked signal may sit on a highly constrained region of the phase-space, one should make sure that a fake signal cannot be built-up from background clustering in that region of phase-space. Explicit checks done in our analysis are described later in this chapter.

6.2 APPLICATION

To apply this optimization method in our analysis we define the following details:

- The two statistically independent subsamples of approximately same size are obtained using the event number, splitting the sample between even and odd events.
- The signal region (S) is defined from Belle's measurement: it is a cluster of events expected at $4.433\,\mathrm{GeV}\,c^{-2}$ which is modeled with a Gaussian function with mean fixed. The width of the Gaussian is fixed at the experimental resolution, assuming negligible natural width for the resonance.
- The background region (B) is evaluated by extrapolating the mass shape in the vicinity of the signal (sidebands) into the signal region ($\pm 2\sigma$). The extrapolation is obtained through an empirical parabolic fit.
- The figure of merit $\frac{S}{1.5+\sqrt{B}}$ is chosen as the one that maximize the chance to obtain a 3σ evidence in any signal search [50].
- Two sets of cuts are obtained based on the event number, an even-optimal configuration and an odd-optimal one. They are swapped, applying the even-optimal configuration to the odd subsample and the odd-optimal configuration to the even sample.

For each subsample the optimization algorithm evaluates the figure of merit for each configuration of cuts on the discriminating variables.

The topology of our channel is rather simple (3-tracks vertex, with an intermediate $\psi(2S)$ resonance). Thus we have a limited number of simple observables effective in discriminating the signal. We chose to optimize the selection using the following ones: transverse momentum of the pion, of the muons, 3-tracks vertex probability and number of $\psi(2S)\pi^-$ candidates per event. The transverse momenta are useful to select products of heavy-flavor decays, vertex probability and number of candidates help in removing combinatorial background. Table 13 reports the details of the sampling of the 4-dimensional space of these variables. Fig. 47 shows the shape of the figure of merit $S/(1.5+\sqrt{B})$, for the even and odd subsamples, as a function of the integer bitmap identifying each configuration of cuts. The integer bitmap is constructed as follows: $I = 10^3 \cdot s_k^{p_\mathrm{T}(\pi)} + 10^2 \cdot s_l^{p_\mathrm{T}(\mu))} + 10 \cdot s_m^{\mathrm{Prob}(Z)} + s_n^{\mathrm{cand}(Z)}$, where, for each quantity, s_i is the i-th step in the scan.

The configuration of cuts corresponding to the maximum of the figure of merit defines the optimized cuts for each subsample. The configurations for the even and odd subsamples are slightly different (Tab. 14). These small differences are expected because of current limited statistics that makes the optimization sensitive to statistical fluctuations around the maximum of $S/(1.5+\sqrt{B})$. The $\psi(2S)\pi^-$–mass distribution of the final unbiased and optimized sample, obtained swapping the configuration of cuts and summing the two subsamples, is shown in fig. 48. We fit this distribution, using a Gaussian and a straight line to model signal and background respectively, leaving all parameters free. The χ^2 fit

Quantity	Range	Step width
$p_{\mathrm{T}}(\pi)$	2.8–3.7 GeV c^{-1}	0.1 GeV c^{-1}
$p_{\mathrm{T}}(\mu)$	3.0–3.5 GeV c^{-1}	0.1 GeV c^{-1}
$P_{\chi^2}(Z)$	10^{-4}–9×10^{-4}	2×10^{-4}
candidates/event	6–14	2

Table 13: Parameters of the optimization algorithm of the data-based procedure.

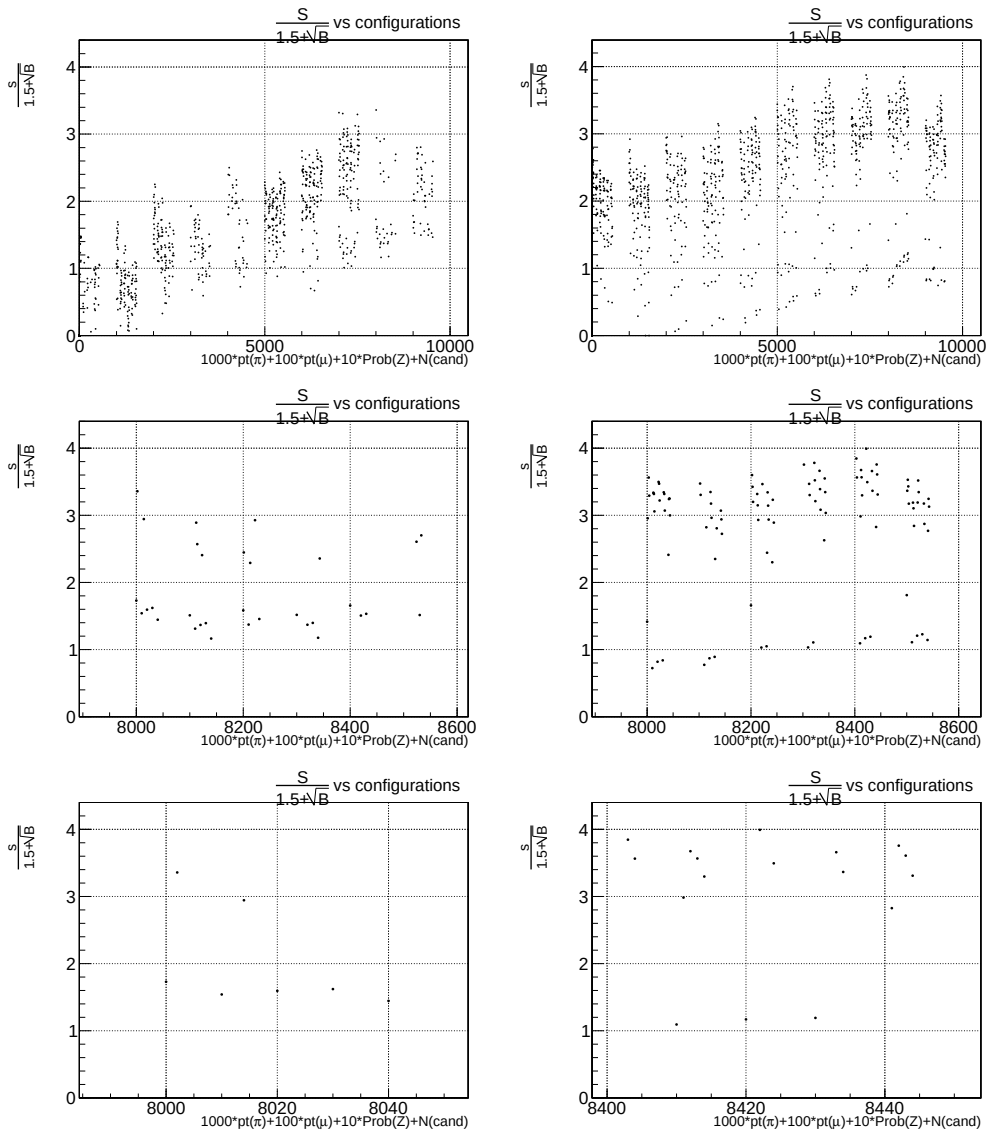

Figure 47: Figure of merit $S/(1.5+\sqrt{B})$ as a function of the integer bitmap chosen to identify the configuration of selection requirements, with magnifications. The optimization of the even-subsample is on the left, the odd-subsample on the right.

determines 48 ± 12 candidates clustering around the mass (4429 ± 4) MeV c^{-2} with width (13 ± 3) MeV c^{-2}. These preliminary values for the parameters seem compatible with Belle's measurement (4433 ± 4) MeV c^{-2}, within uncertainties.

We want now to evaluate the statistical significance of the observed excess.

Subsample	Requirements			
	$p_T(\pi)$	$p_T(\mu)$	$P_{\chi^2}(Z)$	Candidates/event
even	$> 3.6\,\text{GeV}\,c^{-1}$	$> 3.0\,\text{GeV}\,c^{-1}$	$> 10^{-4}$	< 10
odd	$> 3.6\,\text{GeV}\,c^{-1}$	$> 3.4\,\text{GeV}\,c^{-1}$	$> 5 \times 10^{-4}$	< 10

Table 14: Optimized selection from the data-based procedure.

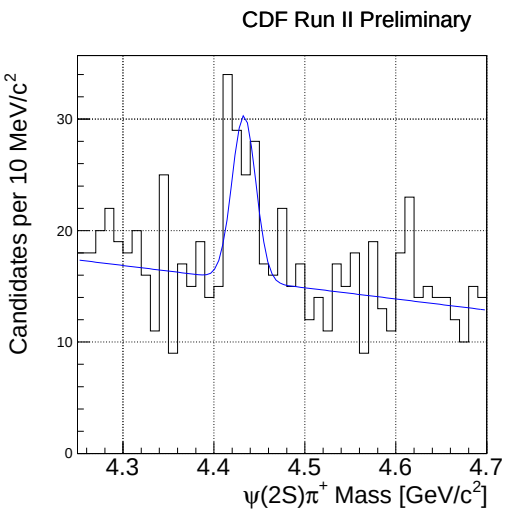

Figure 48: Invariant $\psi(2S)\pi$-mass distribution of the candidates selected through the optimized selection with fit function overlaid.

6.3 SIGNIFICANCE

We estimate the significance of the obtained excess using a Likelihood Ratio (LR) test. We use an unbinned Maximum Likelihood fit in hypothesis of background-only (straight line) or signal+background (Gaussian+straight line) to compare the values of Maximum Likelihood in the two cases. The only free parameter of the signal likelihood is the area of the Gaussian, while the mass is constrained to Belle's measurement, $4.433\,\text{GeV}\,c^{-2}$, and the width to the experimental resolution of $13\,\text{MeV}\,c^{-2}$, as obtained by scaling the observed B^- width with the energy available in the decay.

Fig. 49 shows the results of the fits. The LR obtained from the two fits is 1.0335×10^{-5}. Assuming the quantity $-2 \cdot ln(LR) = 22.25$ to follow a χ^2 distribution with one degree of freedom, the probability of obtaining a background fluctuation as large or larger than observed in data, is 2.4×10^{-6} (p-value). This provides an estimate of the statistical significance of our excess. It is customary to express statistical significance in units (n) of standard deviation of a Gaussian distribution, as in the following formula:

$$n = \sqrt{2} \cdot erf^{-1}(1 - p)$$

where *erf* is the error function of the normal distribution and p is the p-value. We obtain a corresponding value of 4.7σ.

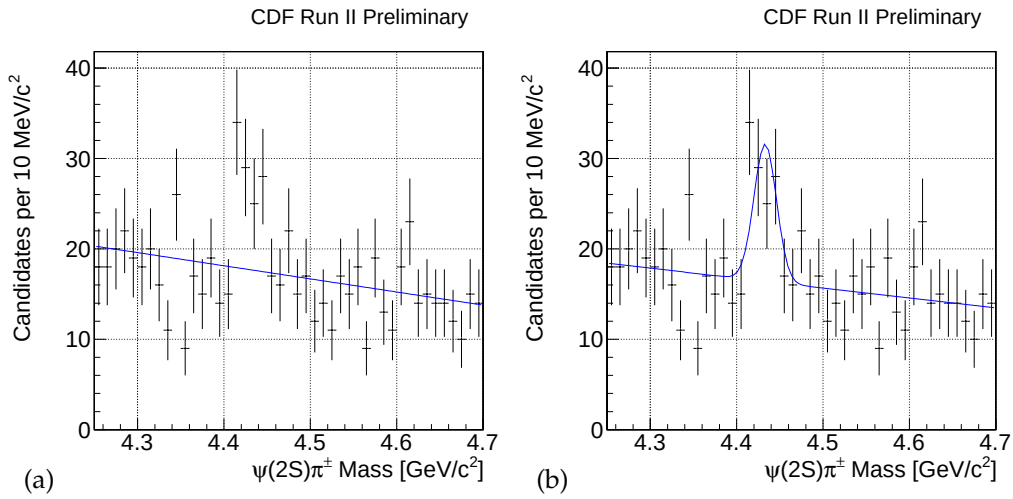

Figure 49: $\psi(2S)\pi^-$ mass distribution with unbinned fit function overlaid, in hypothesis of background only (a) and signal+background (b).

Since the natural width of the resonance is unknown, we also estimate the significance of the excess floating the width parameter. In this case $-2 \cdot log(LR)$ is assumed to follow a χ^2 distribution with two d.o.f. and the p-value obtained is 1.3×10^{-5}, which corresponds to a significance of 4.4σ.

Based on these tests, where the obtained significance greatly exceeds the conventional 3σ threshold, we report evidence of the $Z^-(4430)$ resonance in CDF data. This is the first signal of $Z^-(4430)$ seen in hadrons collisions. This result is also the first significant confirmation of Belle's discovery of the $Z^-(4430)$.

6.3.1 Significance scan

A possible issue of the optimization procedure could rise if a signal is built-up from background that clusters in a specific phase-space region where also the signal would be expected. We checked the optimization sampling a wide mass range to verify if the procedure is able to build a significant signal at mass value where only background is expected.

This is achieved by repeating the full optimization procedure assuming the signal peaking in different mass points. Fig. 50 shows the significance obtained as a function of different masses arbitrarily selected as possible "signal" masses. The only significant signal is obtained at the mass value from Belle's measurement. At all other masses significances below the 1σ level are observed. This provides further confidence that the observed excess is not an artifact of our optimization.

6.4 OPTIMIZATION WITH INDEPENDENT SIGNAL

As a further unbiased check of the presence of a $Z^-(4430)$ resonance in our data, we perform an optimization of the B^- signal yield, fit with a Gaussian, and fitting the underlying

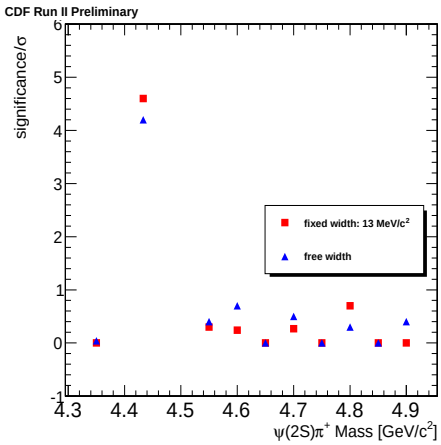

Figure 50: Significance as a function of mass where the signal is assumed expressed in units of standard deviations.

background with a straight line. This procedure is intrinsically unbiased since we are optimizing a completely independent signal than the one we look for. However, it could be strongly suboptimal if $Z^-(4430)$ and B^- features are different as it probably is the case. Table 15 summarizes the sampling details used in this optimization.

Quantity	Range	Step width
$p_T(\pi)$	1.5–5.5 GeV c^{-1}	0.5 GeV c^{-1}
$p_T(\mu)$	3.0–3.5 GeV c^{-1}	0.1 GeV c^{-1}
$P_{\chi^2}(Z)$	10^{-4}–9×10^{-4}	2×10^{-4}
candidates/event	6–21	5

Table 15: Parameters of the optimization algorithm for the B^--based procedure.

Fig. 51 shows the mass distribution corresponding to the optimized selection. A prominent B^- signal appears over a moderate, smooth background, strongly suppressed over the whole range. The structure at 4.430 GeV c^{-2} is still present but its significance, evaluated as described in section 6.3, is now reduced to 2.4σ. This is expected since the B^-, rather than the $Z^-(4430)$, signal was optimized.

The persistence of an excess after an alternative optimization procedure is encouraging and supports the reliability of the results obtained so far.

6.5 SUMMARY OF THE "PROMPT" APPROACH

The search for a $\psi(2S)\pi^-$ resonance without any requirement for presence of a B decay proved successful. With a dedicated, accurate study of track and muon quality aimed at controlling combinatorial background, and using the $B^- \to \psi(2S)\pi^-$ signal as a reference we have extracted a clear signal of about 50 $Z^-(4430) \to \psi(2S)\pi^-$ decays. The statistical significance is well beyond the conventional threshold to claim evidence and studies of peaking background and of the used optimization provide strong confidence that we have found $Z^-(4430) \to \psi(2S)\pi^-$ in CDF data. This is the first $Z^-(4430) \to \psi(2S)\pi^-$ signal seen in hadron collisions and the first confirmation of Belle's measurement.

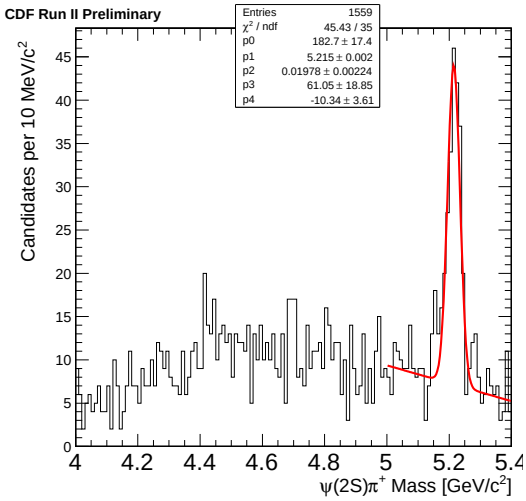

Figure 51: Invariant $\psi(2S)\pi$-mass distribution of the candidates selected through the selection optimized for the B^- signal.

7 CONCLUSIONS AND PROSPECTS

In this thesis we have presented the first search for $Z^-(4430)$ resonances in hadron collisions, using the CDFII detector at the Fermilab Tevatron collider. This was motivated by the unexpected observation of such exotic charged meson by the Belle experiment in 2008, not confirmed by the BaBar experiment. If the existence of the $Z^-(4430)$ is experimentally established, this would be the first unambiguous candidate for a multiquark state.

A coherent and unified analysis method was conceived, aiming at fully exploiting the experimental advantages of the hadron collisions environment. We performed a Belle-like search of the "displaced" $\psi(2S)\pi^-$ resonance as intermediate state in $B^0 \to \psi(2S)K^+\pi^-$ decays, and a search for "prompt" $\psi(2S)\pi^-$ resonances without the requirement of a reconstructed B meson in the event. Different $\psi(2S)$ final states accessible at CDF were studied and explored to increase the analysis' sensitivity.

The "displaced" analysis provided a direct comparison with results from the B-Factories. We isolated a rather pure $B^0 \to \psi(2S)K^+\pi^-$ signal studying the most discriminating observables and optimizing the selection. Inspection of the Dalitz plot showed that acceptance and signal statistics are comparable with those of the B-Factories, but different and larger background contributions are present.

The "prompt" approach proved more effective. We exploited the possibly high production rate of the $Z^-(4430)$, due to the large phase-space available in $p\bar{p}$ collisions at $\sqrt{s} = 1.96\ TeV$. We overcame the main limitation, given by the large combinatorial background, by a dedicated optimization of the reconstruction. The key ingredient in this achievement was the use of the information from the outermost muon chambers, which provide the highest quality muon candidates available at CDF, thus reducing the background. The final selection was obtained through an unbiased data-driven optimization procedure applied in this analysis for the first time. A clear signal was obtained at a mass of (4429 ± 4) MeV c^{-2} with width (13 ± 3) MeV c^{-2}, compatible with Belle's measurement. The statistical significance of the excess is 4.7 standard deviations, which correspond to an evidence of the $Z^-(4430)$ resonance in CDF data. Extensive and detailed tests on the robustness of the signal against artifacts of the optimization procedure or backgrounds from misreconstructed decays have been successfully passed.

We plan to complement the current analysis with a measurement of mass and production rate, using the $B^+ \to \psi(2S)K^+$ signal as a reference and simulations to estimate the relative acceptance and reconstruction efficiencies.

In addition to that, further studies can be performed, such as the measurement of the fraction of $Z^-(4430)$ coming from B decays relative to the promptly produced ones. This, together with the production rate and the information from Belle's measurement, may provide further insight on the phenomenology of this particle.

Another interesting development would be the search for $Z^-(4430) \to J/\psi\pi^-$ decays. While no obvious reasons seem to forbid such a decay, the B-Factories have not yet observed it, and in our case a search would be possible with minimum modifications of the current analysis.

In conclusion, the work described in this thesis has defined a coherent and unified approach to pursue searches for XYZ mesons in hadron collisions. This resulted in the first evidence of $Z^-(4430)$ decays in hadron collisions which, providing the first confirmation of Belle result, establishes the existence of this particle. This measurement is currently being reviewed internally by the CDF collaboration to become a journal paper to be submitted to Physical Review Letters.

A DATA-SIMULATION COMPARISON

We verified the data-simulation agreement of the non-resonant B^0 sample for a number of quantities that have been used in the selection of Chapter 4. Figures 52–53 show the comparison plots where sideband subtracted signal data distributions are in blue and simulated data distributions are in yellow. Clearly the agreement could be improved in several variables, but we chose not to reweigh the simulated data since the observed level of agreement is sufficient for our purposes.

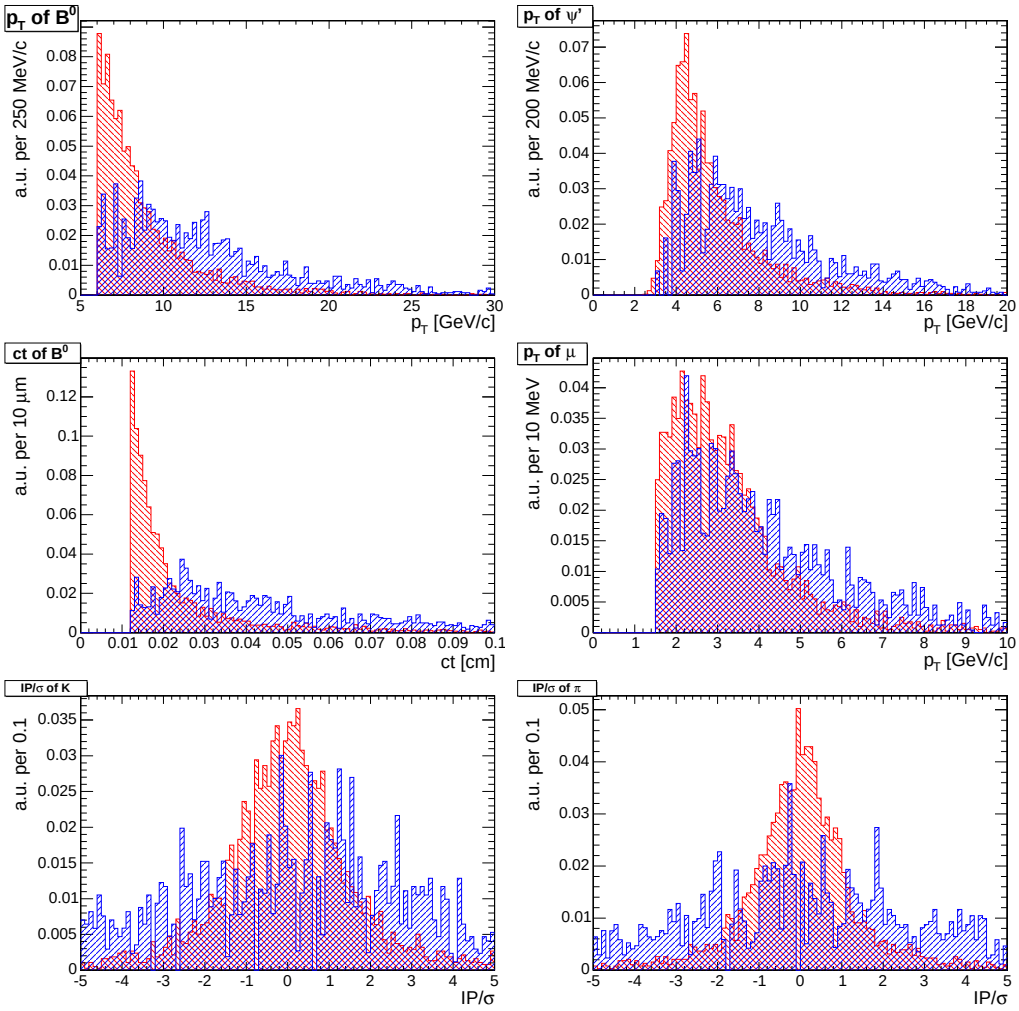

Figure 52: Comparison of sideband-subtracted distributions in data with distributions of simulated samples for several quantities.

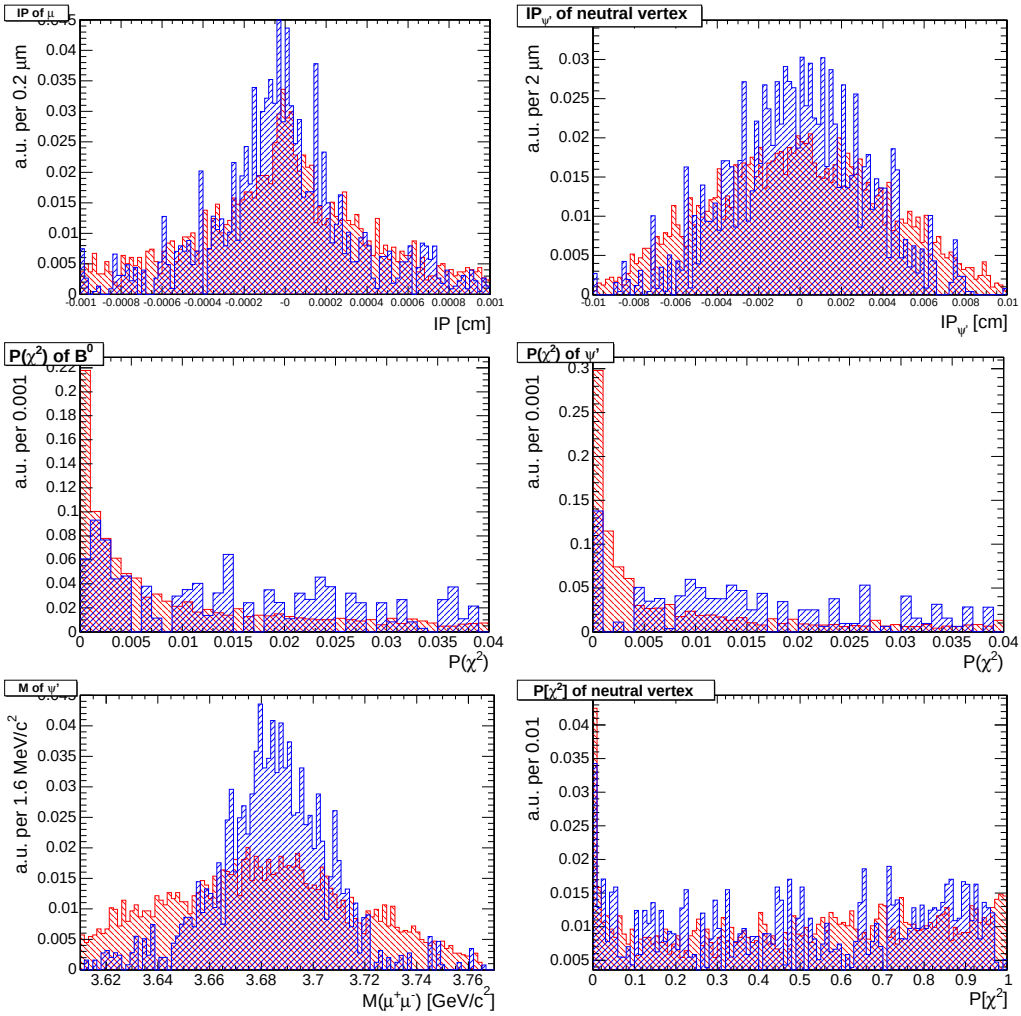

Figure 53: Comparison of sideband-subtracted distributions in data with distributions of simulated samples for several quantities.

B OPTIMIZATION PROCEDURE

The optimization procedure described in Chapter 4 evaluates the value of the figure of merit for 1728 different configurations of the selection. As an example of the distributions probed, fig. 54 and fig. 55 shows the $\psi(2S)K^+\pi^-$–mass distribution corresponding to a few of the 1728 configurations tested by the algorithm.

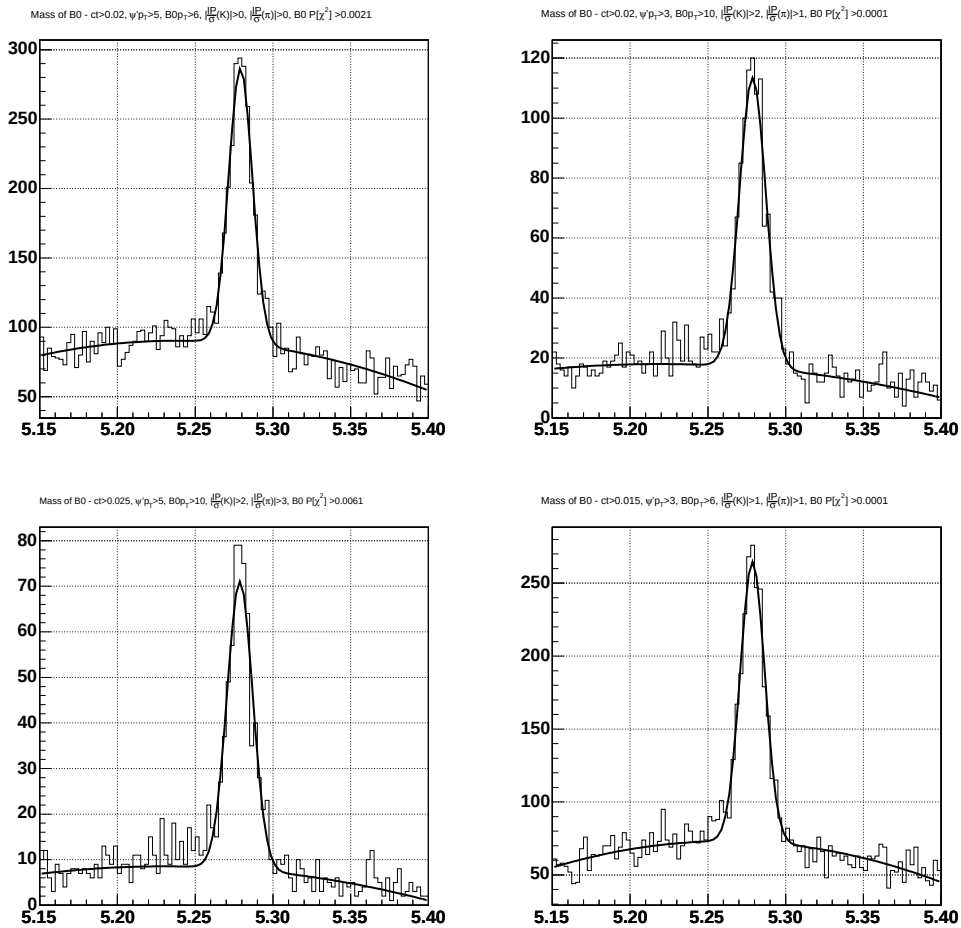

Figure 54: $\psi(2S)K^+\pi^-$–mass distributions of events selected through different configurations of cuts.

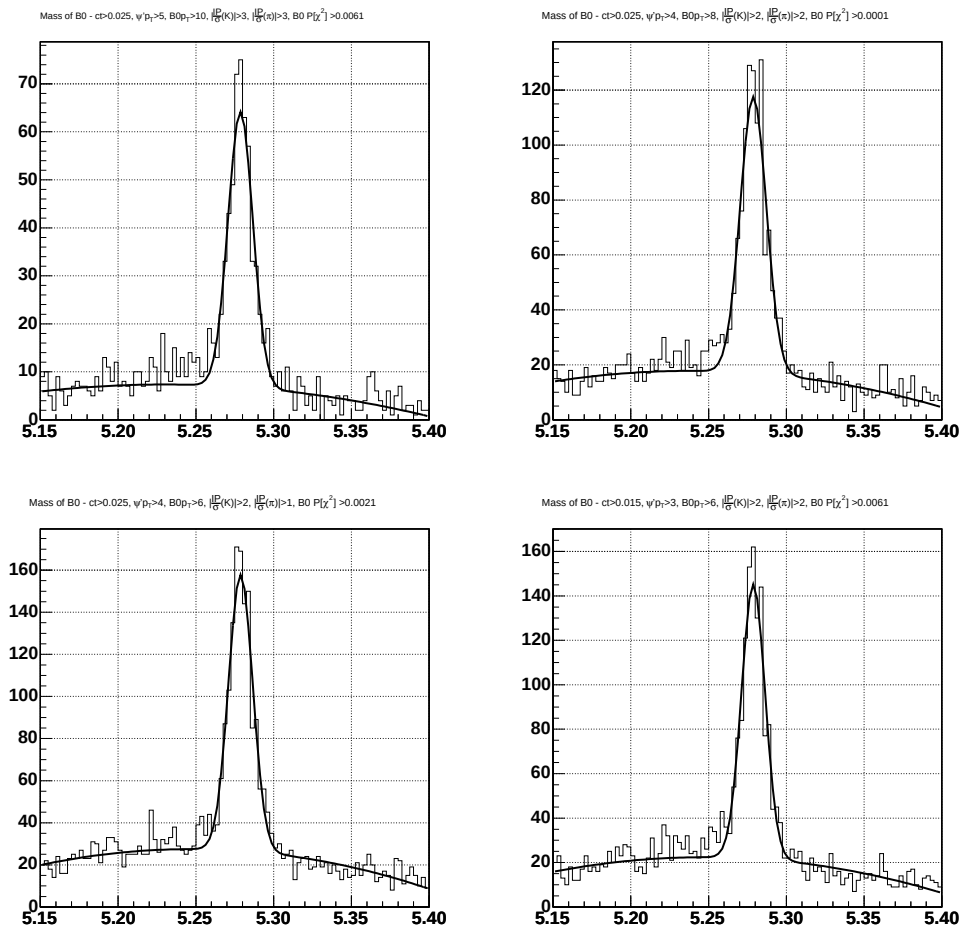

Figure 55: $\psi(2S)K^+\pi^-$–mass distributions of events selected through different configurations of cuts.

ACRONYMS

CDF	Collider Detector at Fermilab
CDFII	CDF in Run II
SVXII	Silicon VerteX
ISL	Intermediate Silicon Layers
L00	Layer 00
COT	Central Outer Tracker
TOF	Time Of Flight detector
CEM	Central ElectroMagnetic Calorimeter
CES	CEntral Strip multi-wire proportional chambers
CPR	Central Pre-Radiator
CHA	Central HAdronic
WHA	Wall HAdronic
PEM	Plug ElectroMagnetic calorimeter
PHA	Plug HAdronic calorimeter
CMU	Central MUon detector
CMP	Central Muon uPgrade
CMX	Central Muon eXtension
IMU	Intermediate MUon detectors
CLC	Cherenkov Luminosity Counters
XFT	eXtremely Fast Tracker
XTRP	eXTRaPolation unit
DAQ	Data AcQuisition
MC	Monte Carlo
QCD	Quantum ChromoDynamics
CQM	Constituent Quark Model
PDG	Particle Data Group
LR	Likelihood Ratio
ISR	Initial State Radiation
LHC	Large Hadron Collider

BIBLIOGRAPHY

[1] M. Gell-Mann. A Schematic Model of Baryons and Mesons. *Physics Letters*, 8:214, 1964.

[2] The Belle Collaboration. Observation of a Resonancelike Structure in the $\pi^{+-}\psi'$ Mass Distribution in Exclusive $B \to K\pi^{+-}\psi'$ Decays. *Physical Review Letters*, 100:142001, 2008.

[3] Diego Tonelli. A simulation-free, unbiased optimization of the selection. *CDF Internal Note*, 9509, 2008. unpublished.

[4] Particle Data Group. Review of Particle Physics, 2008.

[5] Stephen Godfrey and Stephen L. Olsen. The Exotic XYZ Charmonium-like Mesons, 2008.

[6] N. Drenska, R. Faccini, F. Piccinini, A. Polosa, F. Renga, and C. Sabelli. New hadronic spectroscopy, 2010.

[7] The Belle Collaboration. Observation of a narrow charmonium-like state in exclusive $B^+ \to K^+\pi^+\pi^- J/\psi$ decays. *Physical Review Letters*, 91:262001, 2003.

[8] The CDF II Collaboration. Observation of the Narrow State $X(3872) \to J/\psi\pi^+\pi^-$ in $\bar{p}p$ Collisions at $\sqrt{s} = 1.96\ TeV$. *Physical Review Letters*, 93:072001, 2004.

[9] The Belle Collaboration. Observation of a new charmonium state in double charmonium production in e^+e^- annihilation at $\sqrt{s} = 10.6\ GeV$. *Physical Review Letters*, 98:082001, 2007.

[10] The Belle Collaboration. Observation of a near-threshold $\omega - J/\psi$ mass enhancement in exclusive $B \to K\omega J/\psi$ decays. *Physical Review Letters*, 94:182002, 2005.

[11] The Belle Collaboration. Observation of a chi'_{c2} candidate in $\gamma\gamma \to D\bar{D}$ production at Belle. *Physical Review Letters*, 96:082003, 2006.

[12] The BABAR Collaboration. Observation of a Broad Structure in the $\pi^+\pi^- J/\psi$ Mass Spectrum around 4.26 GeV/c^2. *Physical Review Letters*, 95:142001, 2005.

[13] CLEO Collaboration. Confirmation of the Y(4260) Resonance Production in ISR. *Physical Review D*, 74:091104, 2006.

[14] Belle Collaboration. Measurement of $e^+e^- \to \pi^+\pi^- J/\psi$ Cross Section via Initial State Radiation at Belle. *Physical Review Letters*, 99:182004, 2007.

[15] The BABAR Collaboration. Search for the $Z(4430)^-$ at BaBaR. *Physical Review D*, 79:112001, 2009.

[16] C. Hanhart, Yu S. Kalashnikova, A. E. Kudryavtsev, and A. V. Nefediev. Reconciling the X(3872) with the near-threshold enhancement in the $D^0\bar{D}^{*0}$ final state. *Physical Review D*, 76:034007, 2007.

[17] L. Maiani, A. D. Polosa, and V. Riquer. The Charged $Z(4433)$: Towards a New Spectroscopy, 2007.

[18] D. P. McGinnis. Fermilab Tevatron operational status. In C. Horak, editor, *proceedings of the Particle Accelerator Conference (PAC 05)*, 2005. in addition, detailed and updated information on the Tevatron is available in the following webpages: `http://www-bd.fnal.gov/runII/index.html` `http://www-bdnew.fnal.gov/operations/rookiebooks/rbooks.html`.

[19] D. Mohl et al. Physics and Technique of Stochastic Cooling. *Phys. Rept.*, 58, 1980.

[20] S. Nagaitsev et al. Experimental Demonstration of Relativistic Electron Cooling. *Phys. Rev. Lett.*, 96, 2006.

[21] R. Blair and others (CDF II Collaboration). The CDF II Detector, Technical Design Report. *FERMILAB-Pub-96/390-E CDF*, 1996.

[22] C. S. Hill. Initial experience with the CDF layer 00 silicon detector. *Nucl. Instrum. Methods*, A511, 2003.

[23] A. Sill. CDF Run II silicon tracking projects. *Nucl. Instrum. Methods*, A447, 2000.

[24] A. Affolder et al. Status report of the intermediate silicon layers detector at CDF II. *Nucl. Instrum. Methods*, A485, 2002.

[25] A. Affolder et al. CDF Central Outer Tracker. *Nucl. Instrum. Methods*, A526, 2004.

[26] J. Marriner. Secondary vertex fit with mass and pointing constraints (CTVMFT). *CDF Internal Note*, 1996, 1993. unpublished.

[27] P. Gatto. Performance of the new tracking system at CDF II. Master's thesis, University of Padova, 2001. Ph.D. thesis, FERMILAB-THESIS-2001-23.

[28] S. Menzemer. TrackingCal - A tracking and alignment software package for the CDF II silicon detector. Master's thesis, University of Karlsruhe, 2002. CDF Internal Note 5968, unpublished.

[29] G. Ascoli et al. CDF central muon detector. *Nucl. Instrum. Methods*, A268, 1988.

[30] C. M. Ginsburg et al. CDF Run 2 Muon System. *Eur. Phys. J.*, 33(S1002), 2004.

[31] D. Acosta et al. A Time-of-Flight detector in CDF-II. *Nucl. Instrum. Methods*, A518, 2004.

[32] L. Balka et al. The CDF central electromagnetic calorimeter. *Nucl. Instrum. Methods*, A267, 1988.

[33] S. R. Hahn et al. Calibration systems for the CDF central electromagnetic calorimeter. *Nucl. Instrum. Methods*, A267, 1988.

[34] M. Gallinaro. A New Scintillator Tile/Fiber Preshower Detector for the CDF Central Calorimeter. *IEEE Trans. Nucl. Sci.*, 52, 2005.

[35] S. Bertolucci et al. The CDF central and endwall hadron calorimeter. *Nucl. Instrum. Methods*, A267, 1988.

[36] M. Albrow et al. The CDF plug upgrade electromagnetic calorimeter: test beam results. *Nucl. Instrum. Methods*, A480, 2002.

[37] M. Albrow et al. A preshower detector for the CDF Plug Upgrade: test beam results. *Nucl. Instrum. Methods*, A431, 1999.

[38] G. Apollinari et al. Shower maximum detector for the CDF plug upgrade calorimeter. *Nucl. Instrum. Methods*, A412, 1998.

[39] C. Avila et al. A measurement of the proton-antiproton total cross-section at $\sqrt{s} = 1.8\,\mathrm{TeV}$. *Phys. Lett.*, B445(419), 1999.

[40] D. Acosta et al. The performance of the CDF luminosity monitor. *Nucl. Instrum. Methods*, A494, 2002.

[41] E. J. Thomson et al. Online Track Processor for the CDF Upgrade. *IEEE Trans. Nucl. Sci.*, 49, 2002.

[42] G. Gomez-Ceballos et al. Event Builder and Level 3 at the CDF experiment. *Nucl. Instrum. Methods*, A518, 2004.

[43] J. Antos et al. Data processing model for the CDF experiment. *Nucl. Instrum. Methods*, cerca, 2006.

[44] E. Gerchtein and M. Paulini. CDF detector simulation framework and performance. In *eConf. C0303241 TUMT005*, 2003. [physics/0306031].

[45] R. Braun et al. *GEANT: Simulation Program For Particle Physics Experiments. User Guide And Reference Manual*, 1978. CERN-DD-78-2-REV.

[46] P. A. Movilla-Fernandez. Performance of the CDF Calorimeter Simulation in Tevatron Run II. In R. Yoshida S. Magill, editor, *Proceedings of the XII International Conference on Calorimetry in High Energy Physics (CALOR 06)*, 2006. [physics/0608081].

[47] R. Veenhof. GARFIELD, recent developments. *Nucl. Instrum. Methods*, A419, 1998.

[48] M. Gold. Description of the Parameterized Charge Deposition Model. *CDF Internal Note*, 5871, 2002. unpublished.

[49] CDF Collaboration. Observation of the Ω_b^- Baryon and Measurement of the Properties of the Ξ_b^- and Ω_b^- Baryons. *Physical Review D*, 80:072003, 2009.

[50] Giovanni Punzi. Sensitivity of searches for new signals and its optimization, 2003.